



**POLITECNICO**  
MILANO 1863

## School of Industrial Engineering

### Course of Launch Systems



## Launch Systems Project VIPER-1

---

Academic Year 2024-2025

---

Person code	Surname	Name	Email
11011619	De Amicis	Vincenzo	vincenzo.deamicis@mail.polimi.it
10767871	Di Carlo	Pierpaolo	pierpaolo.dicarlo@mail.polimi.it
10725102	Di Rago	Domenico	domenico.dirago@mail.polimi.it
11010337	Manucci	Paolo	paolo.manucci@mail.polimi.it
10713012	Rizzi	Mirko	mirko.rizzi@mail.polimi.it
10691238	Santalucia	Andrea	andrea.santalucia@mail.polimi.it
10739778	Taeggi	Federico	federico.taeggi@mail.polimi.it
10652780	Carretta	Vincenzo	vincenzo.carretta@mail.polimi.it
10668572	Castoldi	Paolo	paolo.castoldi@mail.polimi.it

The rocket is the most powerful tool for expanding humanity's boundaries into space

---

*Wernher von Braun*

# Abstract

This study presents the conceptual design and performance analysis of an airborne-launched rocket system, deployed from a civil Boeing 747, and able to carry 250 kg of payload to LEO. After release from the carrier aircraft, the launcher enters an unpowered aerodynamic maneuvering phase, exploiting a static unstable system. To converge to optimal attitude, the tail fins are deployed to ensure stability, while thrust vector control (TVC) is employed to dissipate the momentum. Then the vehicle is propelled by two stages to its target altitude, performing the payload orbital insertion through a dedicated kick-stage. The first stage is designed to be recovered using parachutes, highlighting simplicity and cost-effectiveness. This preliminary design offers a promising solution to improve satellite launch accessibility and flexibility, reducing dependence on traditional ground-based systems.

# Nomenclature

$\delta$	Thrust Deflection Angle	$C_t$	Tip Chord
$\delta_{fin}$	Fins Deflection Angle	$d_{main,ext}$	External Diameter of main parachute
$\eta_{att}$	Impact attenuator efficiency	$d_{main}$	Internal Diameter of main parachute
$\phi$	Roll Angle	$F_{inf}$	Inflation force
$\rho$	Density of the atmosphere	$f_{nose}$	Nose Finesse Ratio
$\rho_0$	Density at sea level	$g$	Gravity acceleration
$\rho_{kev}$	Density of Kevlar-29	$g_0$	Gravity acceleration at sea level
$\rho_{tropo}$	Density in the troposphere	$h_{drogueopen}$	Drogue parachute opening altitude
$\sigma$	Tensile strength	$h_{mainopen}$	Main parachute opening altitude
$\tau_{f_{main}}$	Main parachute inflation time	$h_{main,ext}$	External height of main parachute
$\tau_f$	Parachute inflation time	$h_{main}$	Internal height of main parachute
$\varphi$	Joint Angle	$l_{lines,main}$	Length of main parachute reefing lines
$A$	Ballistic parameter	$l_{lines}$	Length of reefing lines
$AR$	Aspect Ratio	$m_{drogue}$	Drogue parachute mass
$C_D$	Drag coefficient	$m_{dry\_stage}$	First stage dry mass
$C_g$	Centre of Gravity	$m_{main}$	Main parachute mass
$C_L$	Lift coefficient	$m_{tot,stage}$	Total mass of the stage
$C_p$	Centre of Pressure	$n$	Parachute canopy inflation fill constant
$C_{D_{main}}$	Drag coefficient of main parachute	$n_{acc}$	Permitted deceleration
$C_{inf,main}$	Main parachute inflation coefficient	$n_{main}$	Main parachute canopy inflation fill constant
$C_{inf}$	Inflation coefficient	$r_n$	Tip Radius
$c_{mac}$	Mean Aerodynamic chord	$S$	Area
$C_{x_{main}}$	Main parachute opening force coefficient	$s$	Deceleration distance
$C_x$	Opening force coefficient	$S_{main}$	Area of main parachute
$Ca$	Axial Force coefficient	$t_{mac}$	Thickness At Mean Aerodynamic chord
$Cn$	Normal Force coefficient	$V$	Volume
$Cr$	Root Chord	$v_{land,f}$	Final landing velocity
		$v_{land,i}$	Initial landing velocity



$V_{main,th}$	Volume of main parachute	D	Drag
$v_{stab,main}$	Main parachute stabilized velocity	d	Diameter
$v_{stab}$	Parachute stabilized velocity	L	Lift
$v_{td}$	Velocity at Touchdown	l	Length
$W_{drogue}$	Drogue parachute weight	M	Mach Number
$W_{dry\_stage}$	First stage dry weight	q	Dynamic Pressure
$W_{main}$	Main parachute weight	T	Thrust
X	Force reduction factor		
b	Wing Span	W	Weight

# Acronyms

**AD<sup>2</sup>** Advancement Degree of Difficulty 5

**ALB** Advanced Lightband 28

**AoA** Angle of Attack viii, x, xviii

**ARCA** Romanian Cosmonautics and Aeronautics Association 4, 9, VII

**CH<sub>4</sub>** Methane 9

**DOC** Direct Operational Cost 30

**EOM** Equation of motion xviii, 15

**FDM** Finite Difference Method 19

**FTCS** Forward Time Centered Space xxi

**H<sub>2</sub>O<sub>2</sub>** Hydrogen Peroxide 9

**HLR** High Level Requirement 1, 2, 4–7, 9, 20, 23, 31

**HoQ** House of Quality 5, 25

**IOC** Indirect Operational Cost 30

**LEO** Low Earth Orbit 1, II

**LH<sub>2</sub>** Liquid Hydrogen 9

**LOX** Liquid Oxygen xxxv, 9, 10, 25, 26, 29

**LV** Launch Vehicle 25–27, 29

**MECO** Main Engine Cut Off xxxiv, 29, VIII

**MER** Mass Estimating Relations vi, xxxii, 25, VIII

**MSIS** Master of Science in Information Systems 3

**NRLMSISE** Naval Research Laboratory Mass Spectrometer and Incoherent Scatter Radar Exosphere 3

**R-** Requirement dependent to one of the HLRs 1, 2, 6

**ROI** Return On Investment 2, 4, 6, 9, 30

**RP-1** Rocket Propellant-1 xxxv, 9, 10, 25, 26, 29

**RPA** Rocket Propulsion Analysis 9



**SM** Static Margin 13, 15

**SSO** Sun-synchronous orbit 1, 3

**ToF** Time of Flight 14

**TPS** Thermal Protection System xx, 19

**TRL** Technology Readiness Level 5, 9, 30

**TSTO** Two Stages To Orbit 3, 6

**TVC** Thrust Vector Control xix, 12, 13, 16, 17, II

# Contents

<b>1</b>	<b>Introduction</b>	<b>1</b>
1.1	Mission Requirements . . . . .	1
1.2	Launch and landing site . . . . .	2
1.3	Atmospheric Model . . . . .	3
1.4	Baselines . . . . .	3
1.4.1	LauncherOne . . . . .	3
1.4.2	Electron . . . . .	4
1.4.3	Haas (ARCA) . . . . .	4
1.4.4	Pegasus XL . . . . .	4
1.4.5	Falcon 9 . . . . .	4
1.5	House of Quality . . . . .	5
1.6	Risk Assessment . . . . .	5
1.7	Requirements flow down to subsystems . . . . .	5
1.7.1	Stages Design . . . . .	6
1.7.2	Aerodynamic and shape . . . . .	6
1.7.3	Propulsion . . . . .	6
1.7.4	Recovery System . . . . .	6
<b>2</b>	<b>Design Process</b>	<b>7</b>
2.1	Mission Analysis and Mass Budget . . . . .	7
2.1.1	$\Delta V$ budget estimation . . . . .	7
2.1.2	$\Delta V$ losses . . . . .	7
2.1.3	Mass Budget . . . . .	8
2.2	Propulsion . . . . .	8
2.2.1	Engine and propellant selection . . . . .	9
2.2.2	Choice . . . . .	9
2.2.3	I stage: Executor . . . . .	9
2.2.4	II stage: Rutherford . . . . .	10
2.2.5	Tank sizing . . . . .	10
2.3	Aerodynamics . . . . .	10
2.3.1	Shape . . . . .	10
2.3.2	Centre of Gravity and Inertia estimation . . . . .	12
2.3.3	Drop Phase . . . . .	12
2.3.4	Stability and Equilibrium . . . . .	13
2.4	Trajectory . . . . .	15
2.4.1	Simulation results . . . . .	16
2.4.2	Monte Carlo analysis . . . . .	17
2.5	Thrust Vector Control . . . . .	17
2.6	Thermal Analysis . . . . .	18
2.7	Recovery System . . . . .	20
2.7.1	First stage re-entry phase . . . . .	21
2.7.2	Parachute System . . . . .	21
2.7.3	Parachutes Sizing . . . . .	21
2.7.4	Pflanz Model . . . . .	22



2.7.5	Splashdown . . . . .	23
2.7.6	Recoverability Results . . . . .	24
2.8	MER and Structural Analysis . . . . .	25
2.8.1	Mass Estimating Relationships . . . . .	25
2.8.2	Structural analysis . . . . .	25
2.8.3	On Ground Condition . . . . .	26
2.8.4	In-Flight Condition . . . . .	27
2.8.5	Thickness analysis . . . . .	29
2.8.6	Further design steps . . . . .	29
<b>3</b>	<b>Conclusions</b>	<b>30</b>
3.1	Cost analysis . . . . .	30
3.2	Maneuver & Risk Assessment . . . . .	30
3.3	Requirement Assessment . . . . .	31
<b>Bibliography</b>		<b>i</b>
<b>A Appendix A</b>		<b>iv</b>
A.1	House Of Quality . . . . .	v
A.2	Technical loop . . . . .	vi
A.3	$\Delta V$ Budget . . . . .	vi
A.4	Mass Budget . . . . .	vi
A.5	Tank sizing . . . . .	vi
A.6	Nose Cone Design . . . . .	vii
A.7	Aerodynamics models . . . . .	vii
A.7.1	$C_n$ model . . . . .	vii
A.7.2	$C_a$ model . . . . .	x
A.8	Deflection angle fin $\delta_{fin}$ . . . . .	xv
A.9	$\alpha_{wind}$ disturbance model . . . . .	xvii
A.10	Trajectory . . . . .	xviii
A.11	Thrust Vector Control . . . . .	xviii
A.11.1	Control . . . . .	xix
A.11.2	Reference systems . . . . .	xix
A.12	Convective heat transfer model . . . . .	xix
A.13	Thermal analysis FDM Method . . . . .	xx
A.14	Re-entry . . . . .	xxii
A.14.1	Deorbiting . . . . .	xxx
A.15	Structure . . . . .	xxxi
A.15.1	Pictures . . . . .	xxxii
A.15.2	Equations . . . . .	xxxii
A.16	MECO . . . . .	xxxiv
A.17	Thicknesses tuning process . . . . .	xxxiv
A.18	TRANSCOST Model . . . . .	xxxiv
A.19	Structural Mass Index . . . . .	xxxv
A.19.1	Required thicknesses variation . . . . .	xxxv
A.20	Simulink Model . . . . .	xxxvi
<b>B Autorship Declaration</b>		<b>xxxvii</b>

# Introduction

VIPER-1 is a concept design airborne-launched, two-stage rocket system designed to deliver payloads nominally up to 250 kg into low Earth orbit (LEO). Released from a modified civil Boeing 747, the VIPER-1 begins its journey with an unpowered aerodynamic maneuver that transitions into a powered flight phase using two stages. This design features a recovery system for the first stage, employing parachutes to ensure reusability, cost-effectiveness and simplicity. The project integrates advanced aerodynamic modelling, propulsion technology, and trajectory analysis to optimize performance and meet high-level mission requirements. The Mojave Air and Space Port, California, serves as the launch site, with recovery zones strategically positioned for safe operations. The VIPER-1 offers an accessible and flexible solution to satellite deployment, reducing reliance on traditional ground-based launch systems.

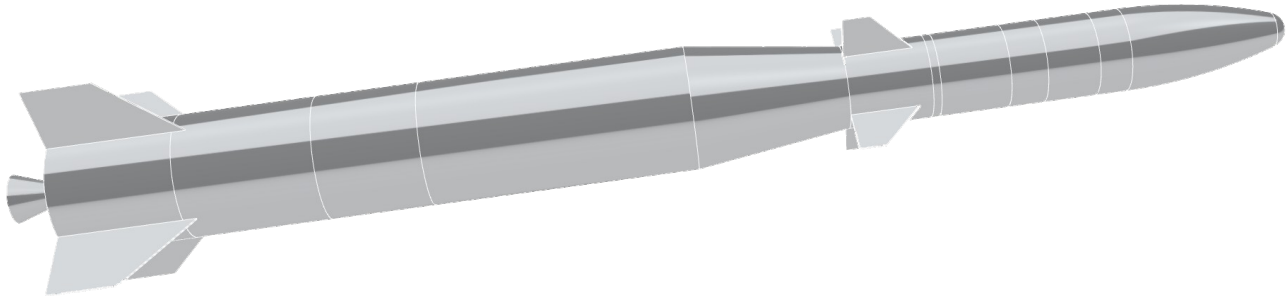


Figure 1.1: VIPER-1 isometric view

## 1.1 Mission Requirements

Requirements have been derived from client requests to guide the design process, ensuring that the final product aligns with customer needs and expectations. The following are the mission requirements identified, that the VIPER-1 design needs to satisfy:

- **HLR-01:** The launcher shall be developed and ready for market within 4 years
- **HLR-02:** The launcher shall be airborne
  - R-02.1: The launcher shall be able to detach safely from the carrier
  - R-02.2: The launcher shall endure all the loads inside the flight envelope of the carrier
- **HLR-03:** The launcher shall be compatible with a civil aircraft
  - R-03.1: The aircraft shall be already available and modifiable within the time-to-market
  - R-03.2: The launcher's length and diameter shall be compatible with the aircraft dimensions
  - R-03.3: The aircraft should take off from a civil infrastructure
- **HLR-04:** The launcher shall be able to carry 250 kg payload to a retrograde 98° SSO at 400 km
  - R-04.1: The uncertainty on the orbit insertion shall be lower than  $\pm 10 \text{ km}$
  - R-04.2: The launcher shall be capable of automating control the trajectory
  - R-04.3: The fairings shall be designed to accommodate 400 kg payload



- R-04.4: The maximum acceleration sustained by the payload shall not exceed the range [-3g,+7g] axial and [-5g,+5g] lateral
- **HLR-05**: The launcher shall be designed in a tandem (axial) configuration
  - R-05.1: The propellant tanks shall be placed only inside the stages
- **HLR-06**: The first stage shall be 100% recoverable
- **HLR-07**: The launcher's upper stages shall be considered for recoverability options
- **HLR-08**: The recovered stages shall be reusable for the number of launches necessary for the ROI
  - R-08.1: The launcher stages shall be designed to be 80% reusable
  - R-08.2: The launcher stages shall use liquid engines for faster refurbishment
- **HLR-09**: The launcher shall use non-toxic propellants
- **HLR-10**: The safety for people on ground shall be ensured during operations
  - R-10.1: The safety on ground shall be granted during stages reentry

## 1.2 Launch and landing site

To accomplish the mission, the launch complex must support the launcher assembly with the carrier, the propellant loading and all the on-ground operations, as well as the whole system take-off.

The selection of possible sites has been performed considering different factors:

- Safety was a pivotal factor in the decision-making process, prioritizing locations remote from densely populated areas and situated near oceans. This approach ensured a contingency option in case of operational issues and provided a suitable splashdown zone for the first stage (**HLR-10**).
- Only operational sites, suitable for civil applications and large civil aircrafts (**HLR-03**), were taken into account given the short time-to-market (**HLR-01**).
- High latitude sites were preferred due to the smaller Earth's velocity contribution (retrograde target orbit).

The principal candidates are reported and analyzed in Table 1.1. The Newquay Airport is located at the highest Latitude; however, due to the intention to conduct first-stage recovery on water relatively close to the mainland, the geography within a 1000 km radius has been assessed as non-compliant, and the site was discarded. Vandenberg Base meets the criteria, however it is primarily intended for military use.

So, the chosen launch site is the Mojave Air and Space Port in California, situated in a relatively remote region, with the nearest city, Lompoc, approximately 14 km away. This location was also selected for its advantageous geographical position, facing the Pacific Ocean, since the detachment of the launcher will occur over the ocean, in proximity to the carrier take-off location. In addition, it can be observed (Fig. 1.2) that the predicted first stage reentry area satisfies the on-ground safety requirement (**R-10.1**). From the Mojave Air and Space Port, the contribution of Earth's rotation is 0.3838 km/s (negative contribution to the  $\Delta V$  budget).

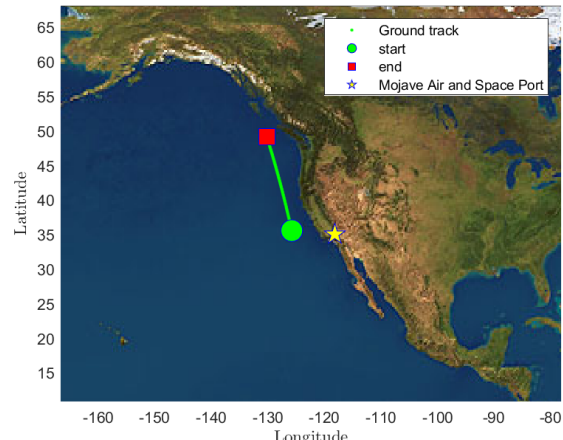


Figure 1.2: VIPER-1 predicted first stage reentry trajectory



Launch site	State	Latitude	Civil
Vandenberg Space Force Base	California (USA)	34°43'58"N	NO
Mojave Air and Space Port	California (USA)	35°03'34"N	YES
Cornwall Airport Newquay	England (UK)	50°26'27"N	YES

Table 1.1: Launch site identification

## 1.3 Atmospheric Model

In order to properly address the whole design, an appropriate model of the Earth's atmosphere up to the target orbit is needed as standard models give only temperature and density conditions up to approximately 86 km. So, the NRLMSISE-00 model [1] of the MSIS class has been implemented. NRLMSISE-00 calculates the neutral atmosphere empirical model from the surface to the lower exosphere (0 m to 1000 km). Additionally, it includes contributions from anomalous oxygen, solar flux and geomagnetic data [2]. Those data were extrapolated based on the previewed solar activity for the start of the VIPER-1 flight operations in approximately 4 years.

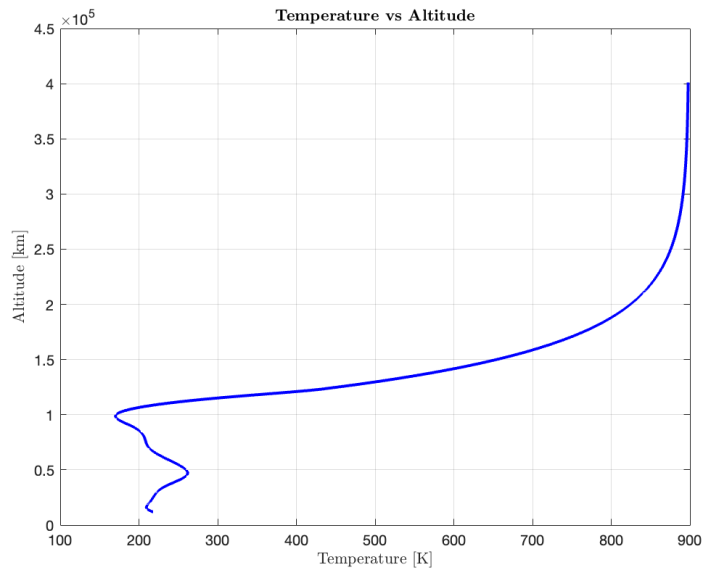


Figure 1.3: Temperature distribution VS Altitude

## 1.4 Baselines

### 1.4.1 LauncherOne

Virgin Orbit's airborne launch system, *LauncherOne* [3], serves as the primary baseline for the VIPER-1 design due to its strong alignment with most mission requirements, apart from recoverability and reusability considerations. It features a TSTO tandem configuration, released from a modified Boeing 747-400, at an altitude of 12 km, Mach 0.8, with an aircraft pitch angle of 26-27°. It serves as a yardstick for the maximum accelerations sustained [3]. This system is capable of delivering a payload of up to 500 kg to LEO or 300 kg to SSO. The vehicle has a liftoff mass of 26,150 kg, including 22,750 kg of propellant, and measures 21.34 m in length. The vehicle is a single-body structure with a constant diameter of 1.8 m, consisting of two stages, both powered by a single Newton motor capable of generating a thrust of  $T = 326.9 \text{ kN}$ . As an initial choice, its whole first stage was taken as a reference including the diameter and the engine. Additionally, it is capable of performing a pitch maneuver via thrust vector control, which has been evaluated for implementation in VIPER-1.



### 1.4.2 Electron

The Rocket Lab Electron launch vehicle has been chosen as a second baseline for several technical features:

- Recoverability and (supposed) reusability of the first stage.
- Rutherford engine has been considered for its second stage thrust capability and its innovative production process, which leverages advanced additive manufacturing techniques.
- Second-stage diameter has been determined to remain consistent with the previously selected engine, ensuring alignment with the design parameters and compatibility between components.
- The Curie Kick Stage, engineered to perform the "kick burn" essential for orbit circularization. Unlike a conventional third stage, the Curie Kick Stage is a compact and modular component integrated within the payload fairings, designed to activate near orbital altitude for precise orbital insertion (Figure 1.4). This innovative and versatile system, inspired by Rocket Lab's implementation, could minimize additional mass while maximizing mission adaptability.

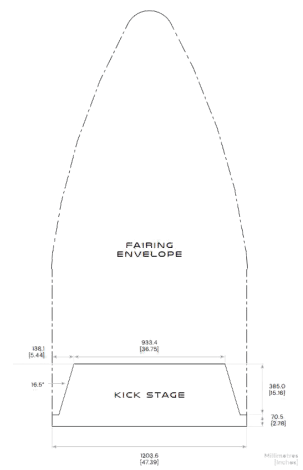


Figure 1.4: Curie Kick-stage [4]

Note: As a consequence of the diameter choice adopted it is clear that an interstage had to be implemented in order to make the transition smooth.

### 1.4.3 Haas (ARCA)

As later described in section 2.2.3 a second engine choice was needed for the first stage. The Haas rocket family, developed by ARCA, has been considered as a potential engine provider for the VIPER-1. In particular, the Executor engine, with a thrust of 260.0 kN, has been evaluated for its notable features, like its ability to operate with a high thrust vectoring angle, making it a strong candidate for integration into the design [5].

### 1.4.4 Pegasus XL

Pegasus XL [6] serves as a relevant case study for airborne launch systems, with multiple successful launches to its credit. Its extensive flight history provides valuable data for estimating price per kg launched in orbit. It can be used as a reference for comparative analysis and budgeting.

### 1.4.5 Falcon 9

Due to the limited data available on stages and engines refurbishment, the Falcon 9 rocket, and the SpaceX company in general, have been used as a baseline for estimating operational costs, in order to determine the minimum number of reuses required for a given system to achieve a return on investment (ROI) as specified by **HLR-08**.



## 1.5 House of Quality

The process of translating customer requests into "engineer-friendly" specifications starts with the use of the HoQ methodology, reported in Appendix [A.1]. Market analysis highlights the company's strengths and weaknesses, enabling qualitative and quantitative benchmarking against competitors. Recoverability is confirmed as a strong point of the system, while it loses a bit in terms of time to market and payload mass capabilities. The HoQ performed for the VIPER-1 identify the main drivers of the design process (Table 1.2) and their relative significance (Figure 1.5).

By evaluating the obtained results in Table 1.2, the foremost parameter is the structural mass index which indeed ended up resulting as a key parameter for the convergence loop between different subsystems (deeply analyzed in 2.16).

Drivers	Relative Weight
Structural Mass Index	14.9 %
Payload Mass	14.2 %
T/W ratio	12.4 %
Target Orbit	9.6 %
Safety factor	9.6 %
Toxicity of exhaust & propellant (LD50)	8.6 %
<b>Total</b>	<b>78.1 %</b>

Table 1.2: Design drivers from HoQ

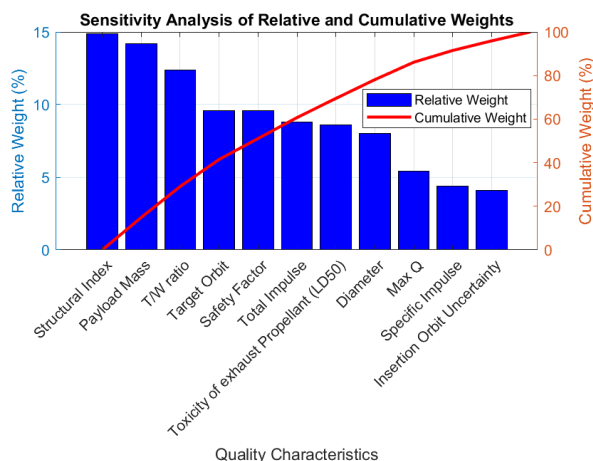


Figure 1.5: Sensitivity Analysis

## 1.6 Risk Assessment

To meet the rapid time-to-market requirement (**HLR-01**), it is crucial to select components with a high TRL; therefore, a minimum TRL of 6 has been established. Preference should be given to commercially available products, while for any new developments required by the project the focus should be on adapting or resizing existing technologies or components. To assess the risks associated with this initiative, an  $AD^2$  index of 4 is introduced to quantify the challenges in achieving the necessary technology maturity.

## 1.7 Requirements flow down to subsystems

Analyzing the baselines and considering all the high-level requirements, some directions for improvement are being considered for implementation. A key driver behind the VIPER-1 design is to perform a self-adjusting maneuver immediately after the deployment from the aircraft. Upon release, the launcher will be in a statically unstable condition as shown in Fig.1.6, which would naturally induce a pitch-up motion until it reaches the required attitude for main engine ignition. This inertial motion could be supplemented, if necessary, by thrust vectoring. However, during the powered flight phase, the full stack will be designed to achieve a statically stable configuration, Fig.1.7. By leveraging this initial adjustment, the need for a dedicated pitch-up maneuver can be eliminated. This strategic choice would allow the vehicle to achieve the desired orbital insertion more efficiently, reducing propellant mass and time to orbit compared to LauncherOne.



### 1.7.1 Stages Design

The first concept considered is a TSTO in tandem configuration, on the philosophy of the LauncherOne baseline. However, in order to ensure successful orbital insertion (**HLR-04**) and to evaluate the re-entry of the second stage (**HLR-07**), the latter must separate at the end of its ignition phase. For this reason, it cannot be used for orbital insertion. Consequently, the Curie kick stage from the Electron baseline has been retained for this purpose. In addition, the **R-04.3** led to the size of the launcher fairing volume to accommodate a maximum payload of 400 kg.

### 1.7.2 Aerodynamic and shape

In order to keep the system unstable at the beginning of the drop phase and subsequently achieve static stability, aerodynamics plays a crucial role. Thus, the presence of different aerodynamic surfaces is required:

- **Forward Fins** positioned ahead of the  $C_g$ , to guide the vehicle until it reaches the desired flight path angle.
- **Deployable Tail Fins** to be opened just before the powered flight phase, ensuring vehicle stability.



Figure 1.6: Folded fins

Figure 1.7: Deployed fins

### 1.7.3 Propulsion

The design choice to reduce the maximum acceleration (**R-04.4**), and consequently the  $T/W$  ratio, leads to the evaluation of existing engine with lower  $T$  compared to the NewtonThree used in the LauncherOne baseline configuration. This approach could offer structural benefits by reducing the mechanical stresses on the vehicle, allowing for a lighter and more efficient design. All the considered engines use non-toxic propellants to meet the **HLR-09** requirement.

### 1.7.4 Recovery System

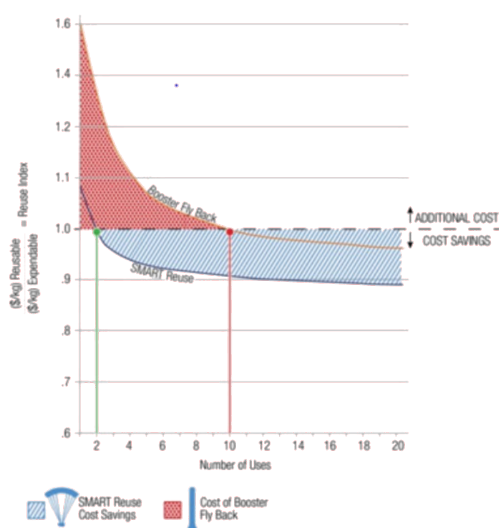


Figure 1.8: Number of reuses and costs

The main choice for the recovery system was based on the short time to market requirement **HLR-01**. Additionally, in order to satisfy the **HLR-06** and **HLR-08**, the choice falls on parachutes as the recovery system. This can be justified by analyzing the costs and efficiency associated with reusable systems. The Figure 1.8 indicates that cost reduction from reusability is not guaranteed solely by reusing stages. The toss-back strategy (booster fly-back) involves high propellant costs, requiring a higher number of reuses to achieve cost savings. In contrast, a parachute system eliminates the significant propellant budget associated with powered return strategies. It offers a simpler and more cost-effective solution for stage recovery, especially with a limited number of reuses. By using parachutes, infrastructure demands are minimized, contributing to the ROI. Furthermore, considering environmental concerns, parachutes reduce the emission of particles and pollutants released during powered flight return.

# Design Process

The design process adopted can be summarized by the following flowchart. Starting from the defined mission HLRs and performance targets (such as payload mass and target orbit), the baseline characteristics are taken as input parameters, focusing on the stages dimensions, propulsion type, and launch options. After each iteration of the technical loop, the design is checked against performance and programmatic requirements. If the performance criteria are not satisfied, minor modifications are applied to the design (Appendix [A.2]).

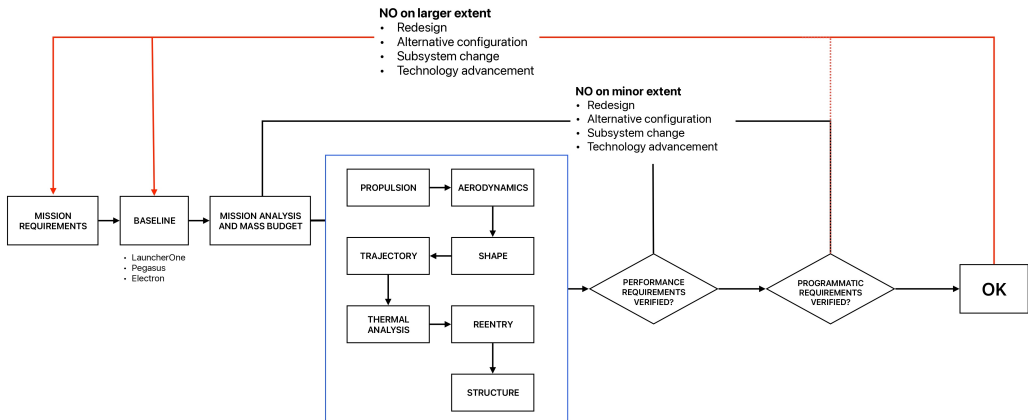


Figure 2.1: Design Workflow

## 2.1 Mission Analysis and Mass Budget

In order to initiate the design process, an initial estimation of the  $\Delta V$  required to complete the mission is needed. Once the specific rocket engines for each stage have been selected, the  $\Delta V$  estimation will be essential for mass budget calculation and for stages design.

### 2.1.1 $\Delta V$ budget estimation

The required  $\Delta V$  to achieve a circular orbit at an altitude of 400 km above Earth's surface has been estimated starting from the necessary orbital velocity,  $v = 7.67 \text{ km/s}$ . Next, assuming the release from the aircraft at 12 km, the speed of sound was calculated,  $a = 295 \text{ m/s}$  (the full equations are reported in Appendix [A.1]). The Mach number for the release has been fixed at 0.8 from the baseline/carrier choice. So, the release velocity is computed:  $v_{release} = 0.236 \text{ km/s}$  (Equations can be found in Appendix [A.3]).

Subtracting the aircraft velocity at releasing time and adding the negative contribution of the Earth's rotation, the total  $\Delta V$  is obtained:

$$\Delta V = 7.82 \text{ km/s} \quad (2.1)$$

### 2.1.2 $\Delta V$ losses

In the preliminary phase of the mission analysis and mass budget estimation, a 15% increase in the required  $\Delta V$  has been included to account for potential losses. These losses are attributed solely to gravity and aerodynamic drag during the ascent phase. This conservative assumption serves as a starting point for the design loop and will be progressively refined using the trajectory simulations. The trajectory analysis provides stage-specific



loss estimates, allowing for iterative adjustments. Once the difference between the initial 15% estimate and the calculated losses from the trajectory falls below 30%, the refinement loop can be concluded.

The final relative error of 20.64% was achieved with the losses reported in Table 2.1, with the latest obtained losses corresponding to 1182.19 m/s.

Stage	Gravity Loss [m/s]	Drag Loss [m/s]	Total Loss [m/s]	[m/s]
I	683.73	122.95	806.69	
II	173.23	0.0184	173.25	
<b>Total Losses</b>				<b>979.94</b>

Table 2.1: Gravity and drag losses for the two stages

The total  $\Delta V$  required to accomplish the mission considering the losses is equal to 8.8 km/s.

### 2.1.3 Mass Budget

In the mission analysis, the staging was performed by allocating a certain percentage of the final ideal  $\Delta V$  (without losses) to each stage. The percentage that minimized the lift-off mass was  $\alpha_1 = 0.5$  for the first stage and  $\alpha_2 = 0.5$  for the second stage. The equations are reported in Appendix [A.4]. Subsequently, the required  $\Delta V$  for each stage was refined by incorporating the gravity and drag losses obtained from the trajectory simulation. This method was used to increase the accuracy of the  $\Delta V$  allocation to each stage, taking into account the specific losses for each one. Additionally, an extra mass was included in the payload to account for the presence of the Kick Stage (without overcome the maximum volume for 400 kg).

Stage	Propellant [kg]	Structure [kg]	Stage [kg]	[kg]
I	18168.23	1869.45	20037.68	
II	1780.62	427.01	2207.64	
Kick Stage	22.22	40	62.22	
<b>Lift-Off Mass</b>				<b>22575.31</b>

Table 2.2: Mass breakdown for each stage and total lift-off mass.

From Table 2.2, it can be noted that the total actual Lift-Off Mass, obtained by summing the masses of the individual stages, is slightly lower than the Lift-Off Mass reported in the table. This discrepancy is due to the initial assumption of a total Kick Stage mass of 80 kg. Following the trajectory simulation, the actual propellant mass required by the Kick Stage was computed, resulting in a total Kick Stage mass reduction of 22.22%. The total mass at lift-off of 22.5 tons is consistent with that of the chosen baseline, the LauncherOne, which had a lift-off mass of 26 tons.

## 2.2 Propulsion

The whole engine design process is summarized in Figure 2.2.

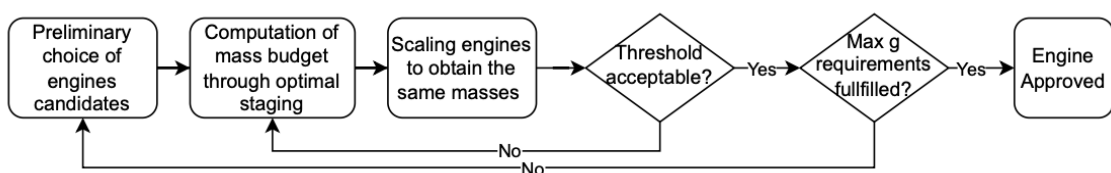


Figure 2.2: Engine design process



Selection has been made with particular attention to:

- **Propellant type:** Non-toxic propellant in order to fulfill **HLR-09**.
- **Throttleability:** to easily handle **HLR-08**, at least one throttleable engine is needed.
- **Reusability:** in order to achieve **HLR-06, HLR-07, HLR-08** solid grain propellant was not the optimal choice due to its long refurbishment time.
- **TRL:** high level of TRL in order to fulfill **HLR-01**.

Through a staging algorithm and a scaling law (reported previously in Section 2.1), the propellant mass budget has been performed.

### 2.2.1 Engine and propellant selection

Given the 4-year market requirement, the choice of building an in-house motor was considered challenging. It was discarded immediately as it was chosen to focus on more important aspects of the mission that would have brought a higher ROI. In order to address this, the best solution was to find and buy an already existing engine with the needed characteristics. As said previously, a two-stage liquid vehicle propellant combination was needed to satisfy **HLR-08**. Based also on the requirement for non-toxic propellant, a comparison between existing engines had to be done.

Properties	LOX/RP-1 [7]	LOX/LH <sub>2</sub> [8]	LOX/CH <sub>4</sub> [9]	H <sub>2</sub> O <sub>2</sub> /RP-1 [10]
Typical O/F ratio	2.56	4.8	3.45	7.07
Combustion Temperature (K)	3670	2985	3560	2975
Oxidizer Density (kg/m <sup>3</sup> )	1340	1340	1340	1450
Fuel Density	860	75	450	860
Specific impulse (s) [11]	353	451	369	319
Characteristic velocity (m/s)	1805	2435	1340	1665
Toxicity [12]	Low	Low	Low	Low
Type	Semi-cryogenic	Cryogenic	Semi-cryogenic	Storable

Table 2.3: Comparison of Propellant Combinations

### 2.2.2 Choice

According to Table 2.3, H<sub>2</sub>O<sub>2</sub>/RP-1 might be the most suitable choice, but it has low performance. Therefore LOX/RP-1 couple was chosen as a good trade-off between energy density and design simplicity. This propellant combination is widely used in rocket propulsion, so with a higher TRL, due to its high performance, cost-effectiveness, and relative ease of handling.

It offers a high specific impulse allowing for smaller tanks, and is more stable and safer to store compared to cryogenic fuels like liquid hydrogen. Finally, to evaluate the needed missing data of the engines, RPA software has been exploited.

### 2.2.3 I stage: Executor

Regarding the first stage, the Newton3 engine was initially chosen from the baseline but later discarded, as it was too powerful with respect to what was needed; so the choice was constrained by the amount of thrust needed keeping into account a safe margin. The first iteration led to the choice of the Executor engine. It is a rocket engine developed by ARCA for use on its Haas rocket series. The Executor uses kerosene and liquid oxygen as propellants in a gas-generator power cycle. Moreover, it uses an ablatively cooled silica-phenolic and carbon fiber composite nozzle, which produces 260 kN of thrust. This resulted in a  $T/W = 1.17$ , more coherence with an airborne launcher, with respect to the previous engine ( $T/W = 1.62$ ). The structure thickness varies from



10 mm to 30 mm. Beside the ablative cooling, the engine is also using a kerosene film cooling method. Its parameters are summarized in Table 2.4.

	$m_p$ [kg]	$P_c$ [bar]	$I_{sp}$ [s]	$T$ [kN]	$t_b$ [s]	$D$ [m]	$\varepsilon$ [-]
<b>Executor</b> [13] [5]	18168.23	43	270	260	208	0.72	12

Table 2.4: I stage parameters

### 2.2.4 II stage: Rutherford

As done for the first stage engine, based on the baseline, the Rutherford engine was chosen. It is a liquid-propellant rocket engine designed by aerospace company Rocket Lab. The engine is used on the company's own rocket, Electron. It uses LOX and RP-1 as propellants and it uses an electric-pump-fed cycle. Moreover, the engine is regeneratively cooled. Its parameters are summarized in Table 2.5.

	$m_p$ [kg]	$P_c$ [bar]	$I_{sp}$ [s]	$T$ [kN]	$t_b$ [s]	$D$ [m]	$\varepsilon$ [-]
<b>Rutherford</b> [14] [15]	1780.62	145	343	25.8	241	0.25	105

Table 2.5: II stage parameters

### 2.2.5 Tank sizing

According to [15], the pressure inside the second stage tanks was set to 5 bar. This value was assumed to be the same for all the tanks. To prevent pumps cavitation, a helium supply and pressurization system had to be considered. High-pressure graphite composite helium bottles were mounted on the aft bulkhead. These were considered (but not sized) in both the propulsion and the mass calculation. To estimate the actual volume of the tanks for both stages, ullage gas was initially considered inside the tanks at 3% and 5%, respectively.

Cylindrical tanks in tandem configuration, with external piping and with elliptical bulkhead have been considered, with semi-major axis  $a = d_{tank}/2$  and semi-minor axis  $b = 0.6 \cdot a$  (Appendix [A.5]). The choice of a tandem configuration was driven by simplicity, and optimization of spaces, and the common bulkhead was immediately discarded because of the different temperatures of propellants.

Fluid	T [K]	M [kg]	V [ $m^3$ ]	H [m]
LOX	78	12761.02	10.86	4.93
RP-1	300	5407.21	6.40	3.05

Table 2.6: Stage 1 fuel and oxidizer data

Fluid	T [K]	M [kg]	V [ $m^3$ ]	H [m]
LOX	78	1250.76	1.04	1.24
RP-1	300	529.95	0.61	0.83

Table 2.7: Stage 2 fuel and oxidizer data

## 2.3 Aerodynamics

### 2.3.1 Shape

As shown in the CAD model of the Viper-1 2.4, its characteristic shape has been accurately designed to meet the mission objectives. The design reflects careful consideration of both functional and aerodynamic requirements. The following are features and the rationale behind the design.

#### Blunted Tangent Ogival Nose

A vehicle traveling at hypersonic speeds experiences significant deceleration primarily due to drag, which plays a critical role in the aerodynamic design of rockets. At these velocities, the nose cone is essential for minimizing drag and preventing flow separation, which can reduce the rocket's efficiency. To achieve this, a spherical-blunted tangent ogival nose was selected. This profile provides a higher critical Mach number but a higher drag coefficient ( $C_D$ ). In the choice between a conical and a blunted tangent ogive nose for hypersonic rockets,



different parameters such as aerodynamic efficiency, structural simplicity, thermal management and payload capacity have been taken into account. A low-fineness nose design is ideal for electromagnetic considerations and allows for more propellant length and volume [16]. For supersonic missiles, a moderate nose finesse is typically used, with a length-to-diameter ratio of about 2. Conical noses are structurally simple and offer lower drag, making them effective in reducing aerodynamic resistance at high speeds. However, their sharp transitions can lead to increased thermal and structural stress. In contrast, tangent ogive ones provide smoother curvature, improving load distribution and aerodynamic stability. Both shapes are still prone to high aerodynamic heating, especially at the tip. This can be mitigated by introducing a blunt tip, which reduces thermal loads while maintaining aerodynamic efficiency. This design offers a balance between thermal protection and performance, making it a practical choice for hypersonic applications. A possible bluntness is designed in Appendix [A.6] The design was constrained by the minimum amount of volume and length we needed in order to store our payload which was approximated to occupy one meter cube of volume.

$l/d$ [-]	$d$ [m]	$r_n$ [m]
2	1.2	0.26

Table 2.8: Nose characteristics



Figure 2.3: CAD Model

### Aerodynamic appendages: shape and configuration

To ensure maneuverability and stability, aerodynamic appendages were designed for the system. The final configuration of the Viper-1 fins and tails adopts a modified cruciform design. In this configuration, the appendages are rotated by  $45^\circ$  relative to the vertical body axis, enabling the system to maintain a null side force without significant losses in vertical force. Balancing aerodynamic efficiency with stability performances, an analysis was conducted on two potential geometries: delta and trapezoidal. The trapezoidal, double-wedged shape was selected for its superior control effectiveness compared to the delta configuration. The latter design exhibited significant variations in the aerodynamic centre during flight, which could adversely affect stability. Additionally, the trapezoidal shape minimizes wingtip vortex formation by redistributing lift more evenly, whereas the delta fins, with their broad base and narrow tip, tend to generate stronger vortexes, increasing drag [16]. Furthermore, both the fins and tails were designed to ensure that, when the tails are fully deployed, the static margin ( $SM$ ) remains greater than zero. This guarantees static stability throughout the nominal trajectory. The final geometrical parameters of both fins and tails are displayed in Table 2.9.

Appendage	$C_t$ [m]	$C_r$ [m]	$b$ [m]	Surface [ $m^2$ ]
Tails	1.00	2.00	2.20	3.30
Fins	0.40	1.00	1.40	0.98

Table 2.9: Aerodynamic appendages geometrical parameters

**Note:** the wingspan  $b$  refers to the span of two appendages merged.

### Aerodynamic models

Regarding the computation of aerodynamic coefficients, particularly  $C_n$  and  $C_a$ , a component build-up methodology was employed to determine the overall aerodynamic behavior of the Viper-1. Detailed descriptions of the models used in this analysis can be found in Appendix [A.7].



### 2.3.2 Centre of Gravity and Inertia estimation

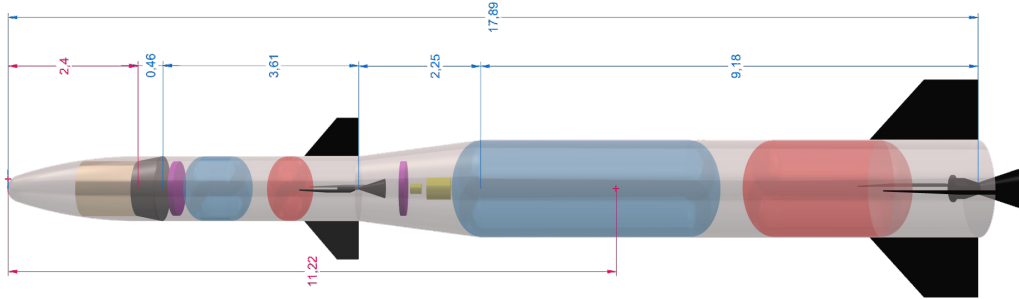


Figure 2.4: CAD Model of rocket

One of the initial steps in accurately evaluating the maneuver, is calculating  $C_g$  and inertia related to it. To achieve this, the lumped mass model was discarded in favor of a more precise representation. An accurate modeling of all individual masses and dimensions was essential to ensure the reliability of the initial maneuver analysis.

The aerodynamics of the Viper-1 is crucial in the design process. In particular, the aerodynamic behavior is crucial in the first part of the ascent, where the rocket crosses the atmosphere up to the Karman line, and during the VIPER maneuver 2.3.3, where aerodynamic forces are exploited through fins and tails to achieve the desired ignition point and subsequently gain the necessary angular initial condition for the nominal trajectory. Even if the boundary line between the atmosphere and space is around 100 km, the adopted atmospheric model gives a negligible value for the density over 84 km, so for this study the boundary has been settled at that height.

According with the latter assumptions both  $C_n$  and  $C_a$  are derived and subsequently  $C_L$  and  $C_D$ . The model followed for the analysis can be found in the Appendix [A.7].

### 2.3.3 Drop Phase

During the drop phase, when the vehicle is released from the aircraft, which maintains its flight horizontal without doing any pitch manouver, the achievement of the correct flight path angle to begin the proper trajectory for orbital insertion is treated as an instantaneous event, resulting in a discontinuous change in the trajectory. However, when considering the vehicle as a rigid body, the release phase is characterized by a transient behavior. This involves a gradual adjustment of the vehicle's orientation, requiring a finite amount of time to achieve the desired attitude through TVC:

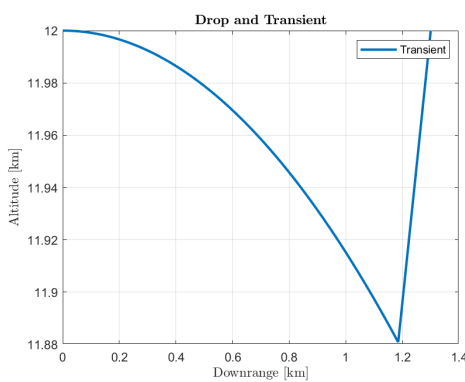


Figure 2.5: Drop Phase for the point mass

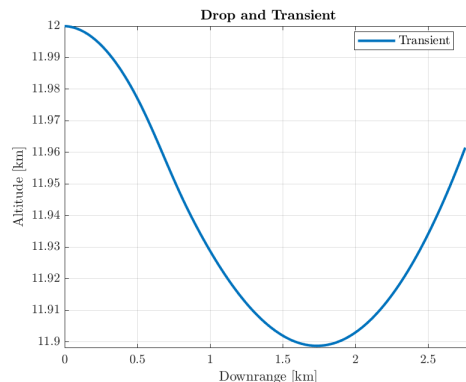


Figure 2.6: Drop Phase for the rigid body

In order to achieve the aim of the mission, it has been decided to follow this main driver:



The launcher shall be able to autonomously reach the initial angle of the nominal trajectory by exploiting a rotation around  $C_g$

In this phase the launcher changes between two configurations (Section 2.3): the first configuration involves the movable forward fins to create a statical instability ( $SM < 0$ ) in order to naturally start a rotation around the  $C_g$ , controlled by changing  $\delta_{fin}$  angle of the fins (Appendix [A.8]); in order to dissipate the stored momentum, consequently to the ignition at 2.5 s, the TVC is added to further slow down the unstable rotation. Slightly before, at 1.5 s, tail fins start deploying, progressively stabilizing the rocket (in order to make a feasible simulation, the deployments lasts 2 s). After the deployment, the second configuration is reached and also the static stability ( $SM > 0$ ) due to the displacement of the  $C_p$  behind the  $C_g$  as can be seen from the plots (2.3.4). The main problem of this procedure was to guarantee the maneuverability and the guidance during the most critical phase in which the rocket has to cancel out the vertical velocity to gain altitude, exploiting the thrust: a preliminary control has been implemented in order to only show the feasibility of the maneuver itself (Figure 2.7). This procedure has been valued as the best trade-off coming from the high sensitivity of the rocket to the changing conditions; this precise operations timing is obtained taking into consideration also a margin which refers to the presence of a transient before the final attitude.

For this reason, it wouldn't be possible to start the active control once reached the chosen trajectory angle, but, as can be seen from the plots (2.7), it begins a bit earlier ( $t = 15\text{s}$ ). This preliminary design takes also into consideration  $C_g$  variation due to the consumption of the propellant (Figure [A.19]) and, as consequence, the inertia of the rocket: this was done by interpolating the initial and final value taken from the CAD. After 15 s, convergence to trajectory angle is reached and the transient can be considered terminated.

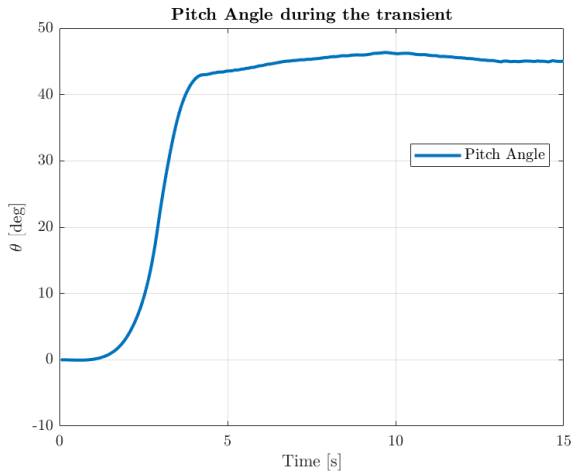


Figure 2.7: Pitch Angle

Taking into account the graphs present in the Figure [A.17], in that phase high angles of attack are reached due to the rotation of the body; as consequence, aerodynamic models described in the section 2.3 undergo variations:

$$\alpha < 10^\circ \Rightarrow \begin{cases} C_n = C_L \\ C_a = C_D \end{cases} \quad \alpha > 10^\circ \Rightarrow \begin{cases} C_L = C_n \cos \alpha - C_a \sin \alpha \\ C_D = C_n \sin \alpha + C_a \cos \alpha \end{cases}$$

Regarding the time before ignition, it is  $t = 2.5\text{s}$ : usually it is around 5s but it has to be underlined that during the falling, the rocket is rotating, moving the nozzle direction away from the aircraft. This allows to have a gain in terms of free fall losses without constituting a risk for the carrier (Figure [A.16]). In this phase, the study is focused on the body dynamics without taking into account the presence of any external disturbance that is reduced to be negligible.

### 2.3.4 Stability and Equilibrium

After defining the launcher principal dimensions , the longitudinal positions of the  $C_p$  and  $C_g$ , are determined.

#### RAS Aero 2

In particular,  $C_p$  is obtained using the software *RAS Aero 2*. Among various simulation software options, *RAS Aero 2* was selected for its both simple and detailed geometry design. Its aerodynamic computational approach



aligns well with the design requirements. Additionally, it excels in rapidly generating accurate data by utilizing a database of real rocket parameters, making it an ideal choice for this application. The  $C_p$  is predicted as a function of the Mach number. For the subsonic  $C_p$ , the standard Barrowman method is used, as our initial Mach number is approaching the transonic phase. Ensuring overall stability is essential, which requires satisfying the condition expressed in Eq.2.2. This condition must be maintained across all configurations, altitudes, and during the reduction of mass over the *ToF*. Adherence to this relation is indispensable for guaranteeing the rocket's stability throughout the mission.

$$X_{C_g} \geq X_{C_p} \quad (2.2)$$

Note: This equation refers to Figure.2.8 for the representation of  $C_p$  and  $C_g$

Various strategies can be employed to meet this stability requirement, one of which involves aerodynamic design choices. In the selected design, stability is achieved by incorporating fins.



## Equilibrium

As mentioned before, the trajectory was modelled as a point mass. In order to check the stability and the possibility of maintaining equilibrium over the path, three different instantaneous "pictures" were taken in consideration:

- End of the transient ( $\tau_1 = 15s$ )
- Max-q ( $\tau_2 = 22.20s$ )
- Max- $q_\alpha$  ( $\tau_3 = 17.75s$ )

	$\tau_1$	$\tau_2$	$\tau_3$
$\delta$ [deg]	1.68	-0.39	0.47
SM [-]	0.12	0.33	0.21

Table 2.10: Static Margin and Gimbal Correction Angle

In Table 2.10 the stability can be identified by checking SM and the equilibrium is guaranteed by the application of an instantaneous correction  $\delta_{fin}$  of the gimbal direction. It is immediately evident from the results that in the transient phase the corrections require more effort with respect to the same body studied on nominal trajectory.

In addition, in this study the perturbation of the wind has been taken into account which generates an  $\alpha_{wind}$  who acts on the body and changes the nominal velocity direction, the model adopted for  $\alpha_{wind}$  is shown in Appendix [A.9]. As explained in Section 2.3.1 trapezoidal double wedge fins were chosen. Once the final stabilizer specifications were established, the atmospheric flight conditions and the geometric configuration (first-stage, second-stage, and  $C_g$  positions) were discretized over time. This enabled a computational validation of the initial stability predictions, reported in Figure 2.8.

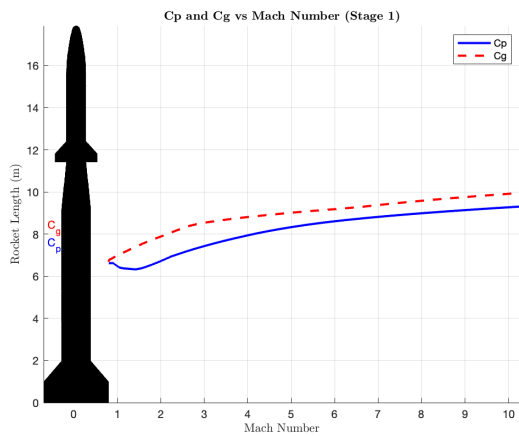


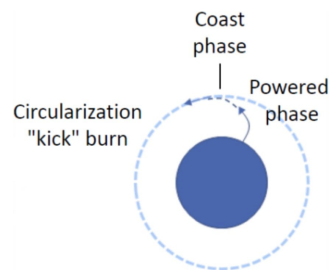
Figure 2.8:  $C_p$  and  $C_g$  variation

	Stage 1	Stage 2
SM [-]	0.04	-1.27

Table 2.11: Minimum static margin

## 2.4 Trajectory

The nominal trajectory of the airborne VIPER-1 is analyzed using a 2DOF round Earth model (the EOM considered are reported in Appendix [A.10]). This framework assumes the vehicle as a point mass, capturing the essential dynamics. In order to better understand the nominal trajectory, the mission can be divided into distinct phases:



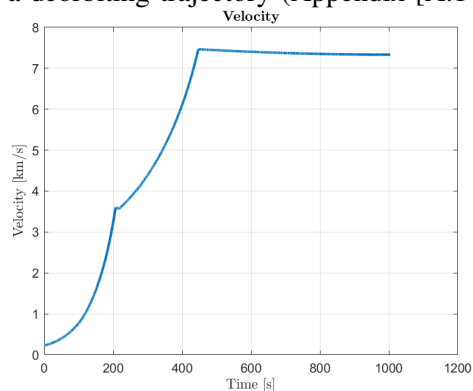
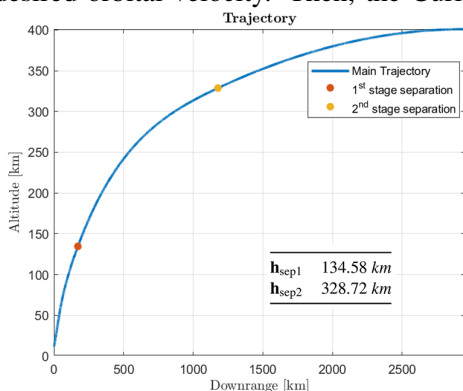
- **Drop Phase:** the launcher is released by the aircraft, initiating a free-fall phase that lasts for a certain amount of seconds to ensure a safe evasion maneuver of the carrier
- **First stage ignition:** the first stage ignites and performs a powered flight, propelling the vehicle along the initial segment of the trajectory
- **Staging phase:** after the burnout of the first stage, the separation happens along with the jettison of the fairings followed by a 10-second idle period where no propulsion is active. This allows to ensure a safe separation between stages
- **Second stage ignition:** the second stage ignites and provides the remaining velocity required to reach the target altitude



- **Coast phase:** after the second stage separation, the vehicle follows a ballistic trajectory determined by the velocity and altitude gained earlier. The vehicle relies on its kinetic energy and follows a trajectory determined by Earth's gravity
- **Kick burn:** at apogee, a circularization burn is performed to reach the correct velocity for orbit insertion

### 2.4.1 Simulation results

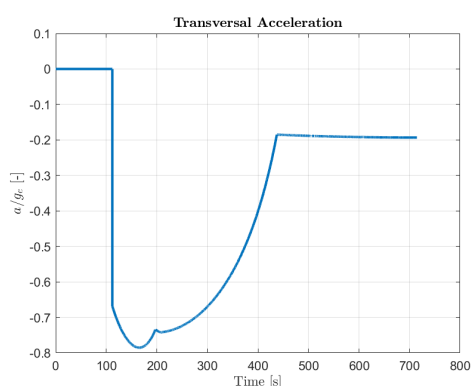
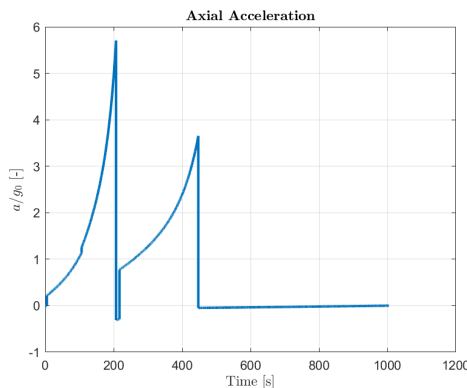
This section analyses the results of the model previously described. After a certain number of iterations, modifying both the initial flight path angle and the altitude up to which the ideal control acts on the variation of the flight path angle, the nominal trajectory in Figure 2.9 was obtained. From the velocity profile in Figure 2.10, it can be noted that the final velocity is slightly lower compared to the orbital velocity reported in Appendix [A.1]. This indicates that the kick stage is required to provide a velocity increment of 217.159 m/s to achieve the desired orbital velocity. Then, the Curie kick stage follows a deorbiting trajectory (Appendix [A.14.1]).



As can be observed, the stages separation occurs at higher altitudes compared to a conventional approach. This is primarily attributed to two factors:

- The self-adjustment maneuver during the drop phase, as explained in Section 1.7;
- The increase in dry mass, and consequently propellant mass, resulting from multiple iterations with the structural subsystem.

By omitting the pitch maneuver, all the burning time is fully dedicated to increasing altitude, enabling the vehicle to reach orbit in the shortest time possible. In fact, it only takes 11 minutes and 50 s to reach an altitude of 400 km, while in the case of LauncherOne, the time to reach orbit exceeded one hour. From Figures 2.11 and 2.12, it can be observed that the maximum acceleration during the ascent phase, reached just before first stage separation, remains below 6g. In Figure 2.12, the acceleration is zero up to 100 s due to the TVC that balances the variation in the flight path angle, which is responsible for the generation of the transversal acceleration.





### 2.4.2 Monte Carlo analysis

A Monte Carlo simulation has been performed in order to evaluate the accuracy of the orbit insertion. The analysis achieved convergence with a standard deviation of less than 10 km in the final orbital position. However, the simulation required introducing very low levels of uncertainty due to the high sensitivity of the trajectory to specific initial conditions, particularly the initial flight path angle and the altitude up to which the control system operates. These parameters critically influence the accuracy of orbital insertion, underscoring the importance of precise control during this phase.

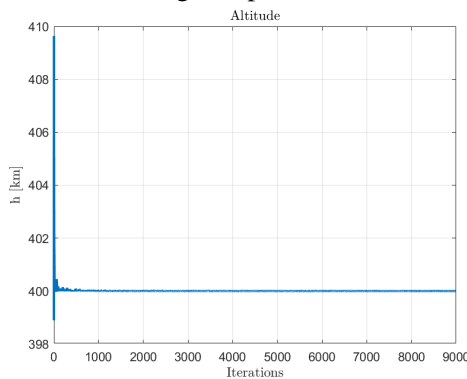


Figure 2.13: Altitude convergence

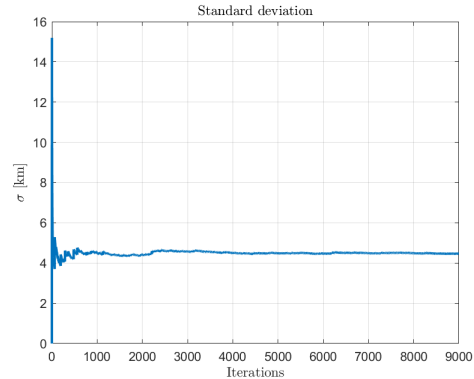


Figure 2.14: Standard deviation on altitude

## 2.5 Thrust Vector Control

A high-level trade-off was conducted to determine the most suitable thruster gimbaling system, evaluating different options based on maximum achievable deflection, system complexity, and heritage (Figure 2.15). The selected methodology entails moving the entire thruster, including the nozzle and combustion chamber. This approach integrates the principles of The Agile Eye, developed by the University of Laval, with a Double Gimbal design. The resulting mechanism offers a lightweight, compact structure capable of achieving high deflection angles while maintaining a significantly simpler design compared to its predecessors.

Feature \ Approach	Movable Thruster	Movable Nozzle	Sec. Fluid Injection	Mech. Deflection
Maximum deflection	Best	Good	Worse	Bad
Complexity	Good	Best	Bad	Bad
Heritage	Best	Bad	Bad	Bad

Figure 2.15: Thruster Gimbaling System

To identify the optimal design, a Pugh matrix approach was employed (Appendix [A.11]) and the "Concept 5" design (Figure 2.16) emerged as the most suitable one.

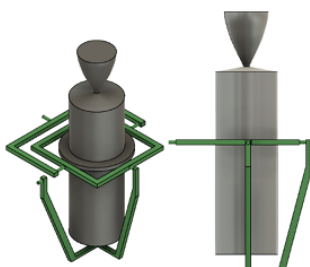


Figure 2.16: Concept 5

This concept demonstrates the capability to achieve high deflection angles up to  $\pm 80^\circ$ . However, such extreme angles would impose significant structural stresses and result in substantial efficiency losses. The literature analysis [17] indicates that a maximum deflection angle of  $\pm 30^\circ$  provides an optimal trade-off, balancing deflection capability with operational efficiency and structural reliability. So, this range has been adopted as TVC deflection limit for the main engine.



The ideal thrust vectoring deflection angle, as studied in Appendix [A.11.1], required to nullify the variation in the flight path angle, up to the altitude necessary to ensure proper orbit insertion. In Figure 2.17, it can be observed that the maximum deflection angle is  $27.35^\circ$ , meaning that our gimbaling system is suitable to our applications.

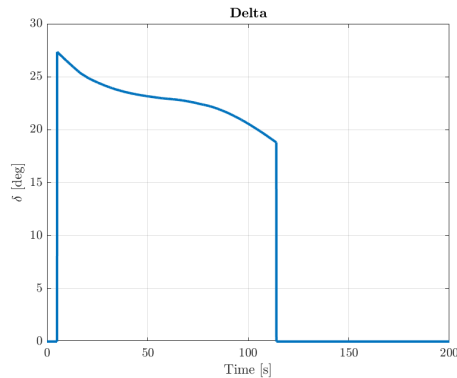


Figure 2.17: Deflection angle

## 2.6 Thermal Analysis

After having designed the nose cone tip shape as shown in Section 2.3.1, the aim is now to analyze how the heat transfer affects it (from the free-stream air) and ensure the following conditions are met:

- Temperature of the nose cone tip does not exceed the service temperature of the material used.
- Temperature of the components connected to the nose cone tip remains below their respective service temperatures.

To address this, the identification of heat transfer sources into the tip is necessary:

1. **Convective:** Heat is transferred from the free-stream air to the tip through convection
2. **Radiative:** Heat is radiated from the free-stream air to the tip
3. **Conductive:** Heat is conducted through the surface and potentially into adjoining components

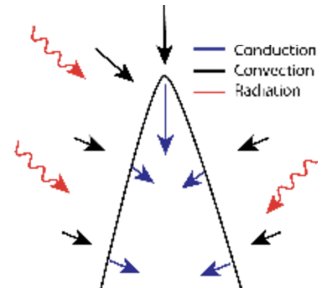


Figure 2.18: Surface tip energy balance

Due to aerodynamic drag and friction between the vehicle skin and the atmosphere, the vehicle accelerates and this leads to intense heating. With the extreme temperatures, convective and radiative heat transfer to the spacecraft are significant [18]. In this work, it is assumed that the temperature increase occurs solely due to aerodynamic heating. It is considered only the convective component of heat transfer since the radiative component is negligible.

### Convective heat transfer model

Modeling convective heat transfer is a complex task. The most accurate approach would involve performing a full unsteady simulation of the rocket flying through the atmosphere and directly measuring the convective heat transfer rate. However, a more practical approach is to approximate this heat transfer using a variety of semi-empirical models that have been developed. For the calculation of the convective heat rate, simple correlations can be derived based on simplifications of the stagnation flow analysis, as discussed in the paper [19]. This paper suggests that the convective heat transfer at the stagnation points of a vehicle (in the Earth's atmosphere) can be modeled by the following equations, further explained in Appendix [A.12]:

$$\dot{q}_{\text{conv}} = C \rho^N V^M \quad C = (1.83 \cdot 10^{-4}) \frac{1}{\sqrt{r_n}} (1 - g_w) \quad (2.3)$$

The heat flux is highest at lower altitudes due to a denser atmosphere, peaking shortly after launch, and decreases significantly as the rocket ascends into thinner atmospheric layers. Additionally, Figure 2.20 shows that



the heat flux peaks around 20 seconds into the ascent, corresponding to the period of maximum aerodynamic heating, and then drops sharply as the rocket gains altitude, reasonable according to [20].

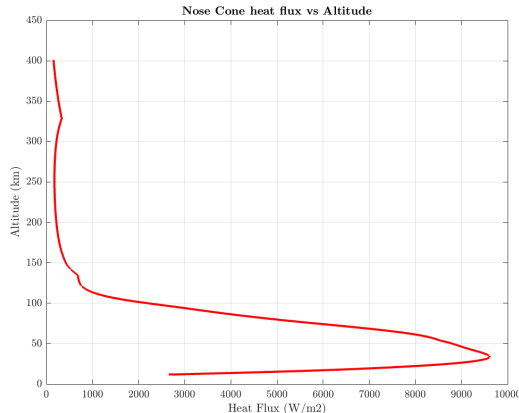


Figure 2.19: Heat transfer as a function of altitude

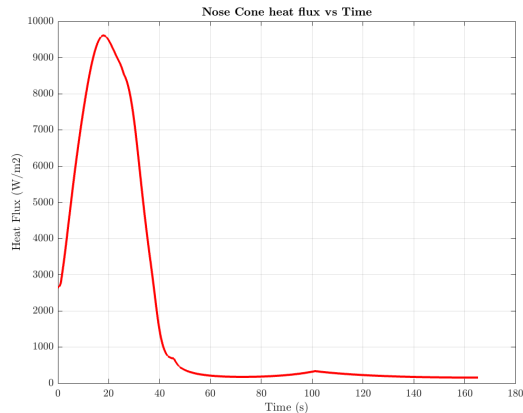


Figure 2.20: Heat transfer as a function of time

### Temperature at wall

For the calculation of the wall temperature, the Finite Difference Method (FDM) was employed [21], this is deeply explained in Appendix [A.13].

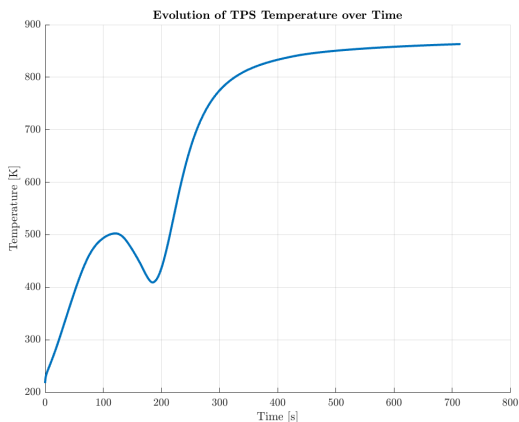


Figure 2.21: External surface temperature over time

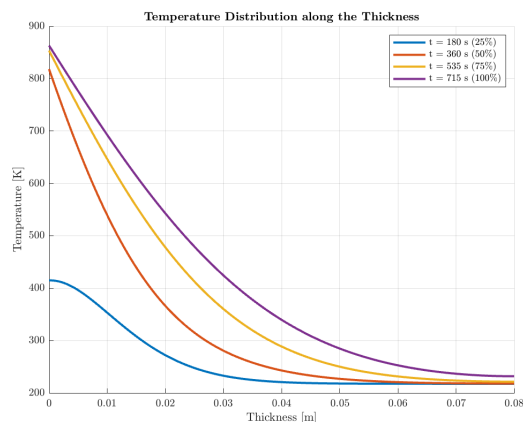


Figure 2.22: Temperature along thickness at different t

Based on the first iteration of the obtained plots, it is clear that a Thermal Protection System (TPS) thickness of 0.03 m is sufficient to ensure the survivability of the aluminum structure, and by extension, the payload, as the temperature remains well below the maximum allowable limit of 660°C [22].

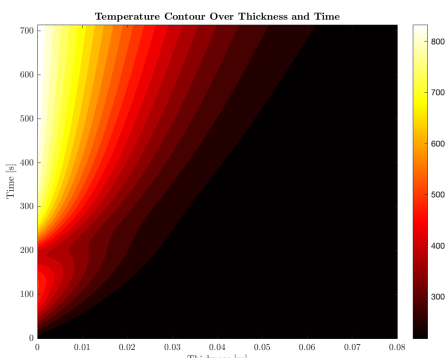


Figure 2.23: Temperature contour

Additionally, the variation in temperature along the thickness at different times is shown in Figure 2.23. However, this is a very approximate calculation, as the vehicle in reality is composed of a combination of different materials across its surface, each with distinct heat transfer properties. Despite these approximations, the results obtained at this stage of design are acceptable for estimating the heat loads experienced by the aircraft. Reiterating with the corrected TPS thickness, which has been updated based on more accurate design parameters, the following results are obtained.

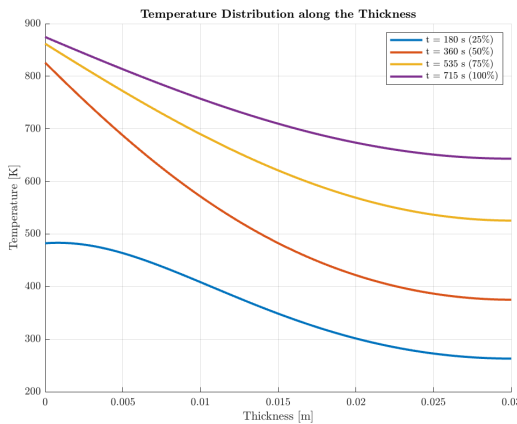


Figure 2.24: Temperature along thickness at different  $t$

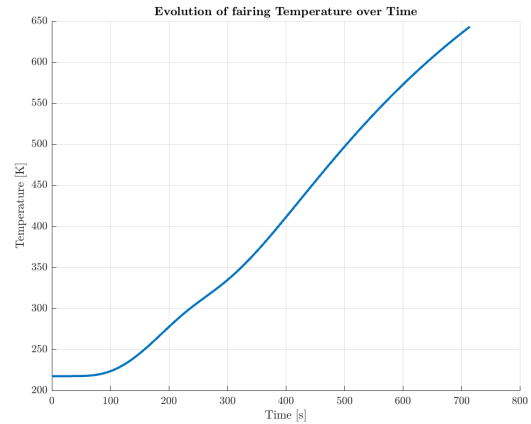


Figure 2.25: Internal surface temperature over time

This adjustment ensures that the model more closely reflects the actual physical conditions and material properties, thereby providing a more reliable estimation of the thermal behaviour under the expected flight conditions. Moreover, a validation of what was obtained in the CAD regarding the bluntness radius is necessary.

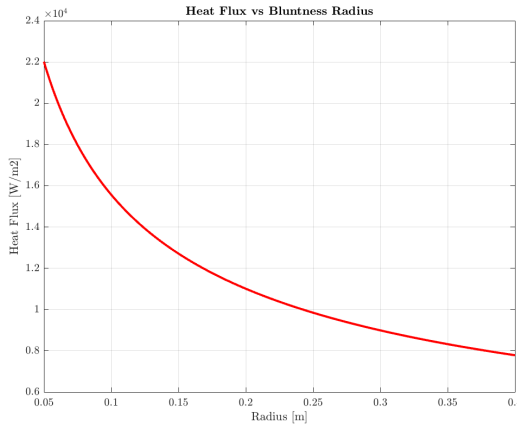


Figure 2.26: Heat flux at different  $r_n$

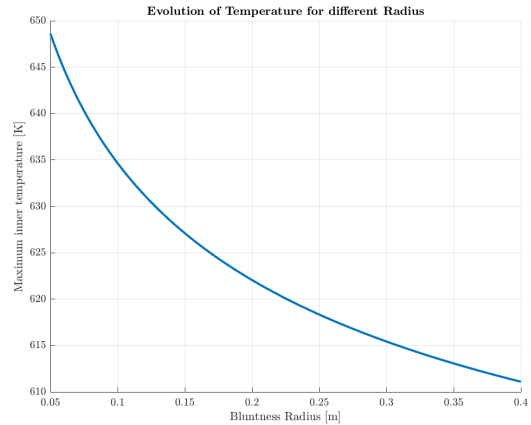


Figure 2.27: Temperature ad different  $r_n$

The two graphs provide a comprehensive analysis of the impact of the bluntness radius ( $r_n$ ) on the thermal behaviour of the surface. From Figure 2.26, it is clear that increasing the bluntness radius leads to a substantial reduction in the heat flux. This trend can be explained by the aerodynamic effect where a larger bluntness radius helps diffuse the shockwave over a larger surface area, thus reducing the intensity of heat transfer to the surface. This phenomenon effectively lowers stagnation point heating, which is a key factor in thermal management. Similarly, Figure 2.27 demonstrates that the reduction of the maximum inner wall temperature aligns with the lower heat flux. From this analysis, it can be stated that,  $r_n = 0.26$  m obtained radius from the constrained geometry is an optimal trade-off point. At this radius, both the heat flux and the inner wall temperature are sufficiently reduced, without incurring excessive aerodynamic penalties.

## 2.7 Recovery System

As required by **HLR-06** and **HLR-07**, the mission must ensure the safe landing of the first stage and evaluate the feasibility of a safe recovery for the second stage. The first stage recovery is analyzed under two scenarios:

- I) The main engine shuts down before full propellant consumption, leaving 898.75 kg for descent deceleration
- II) The propellant is fully consumed during ascent



The analysis primarily focuses on the first stage (released with the interstage attached), while the second stage results are discussed later.

### 2.7.1 First stage re-entry phase

During the initial phase of descent, the stage experiences simple projectile motion, with the main vertical forces being weight and drag, while drag is the only significant horizontal force.

- I Scenario) This approach aims to reduce the vertical velocity of the stage in the upper atmosphere. However, the use of parachutes at this altitude is ineffective due to low air density; hence, the main engine is employed. This requires conserving propellant by releasing the stage earlier than initially planned and ensuring correct stage orientation. To achieve proper orientation, the inherent instability of the first stage with closed fins is utilized. Upon release, the interstage initially leads the trajectory, causing incorrect orientation for subsequent firing. However, due to its instability (with the  $C_g$  at 7.07 m and  $C_p$  at 1.20 m from the top), the stage naturally rotates to a more stable configuration, where the engine leads the rest of the body along its trajectory. This reorientation better aligns the stage in the desired direction, though not completely vertical for optimal thrusting. Mild thrust level retro rockets can be employed for precise alignment, taking advantage of low air density. The altitude for thrusting is chosen to minimize the maximum acceleration experienced during descent
- II Scenario) During the free fall phase, still with closed fins, significant accelerations occur due to the rapid interaction of the stage with a denser atmosphere. The stage follows a parabolic trajectory with initial rotation due to its instability (with the  $C_g$  at 6.92 m and  $C_p$  at 1.20 m from the top) without any control during the initial phase of descent, as neither retro rockets nor the main engine are employed.

### 2.7.2 Parachute System

To assess the feasibility of the specified requirement, drogue and main parachutes have been designed. During parachute re-entry, the parachutes' surface area is a critical parameter, as it plays a key role in decelerating the system. Typically, a re-entry velocity of approximately 8 m/s is targeted for landing, but to ensure additional conservativeness in the analysis, the parachutes have been designed to achieve a touchdown velocity of 6 m/s. A lower landing velocity was not selected, as it would require larger parachutes, increasing the overall mass. The initial selected configuration includes both drogue and main parachutes for each stage. The drogue parachute aims to decelerate the system at higher altitudes, and to grant a stable descent velocity higher than the touchdown one, its size is smaller than the one of the main parachute. In contrast, the main parachute is designed to achieve the desired touchdown velocity, requiring a larger surface area. In addition, each parachute is doubled for redundancy purposes.

### 2.7.3 Parachutes Sizing

The initial step in the sizing process involves defining the main parachute by imposing the touchdown velocity and considering the equilibrium between the system's weight and drag [23]:

$$W = D \rightarrow (m_{\text{dry\_stage}} - m_{\text{drogue}})g_0 = \frac{1}{2} \rho_0 S_{\text{main}} C_{D_{\text{main}}} v_{td}^2 \quad (2.4)$$

The lift action has been discarded from Eq. 2.4 since its effect is minimal compared to other forces, considering the fins are closed and trajectory control via winged configuration is not performed [24]. The stage's dry mass, derived from mass budget computation, is subtracted by the drogue parachute's mass, as it was already released. An initial guess value for the drogue parachute has been used and refined iteratively.

The main parachute is conical with a 75° aperture angle, and the drogue parachute is a ribbed guide surface with 12 ribs, approximated as a conical shape with the same aperture angle [25]. This geometry minimizes mass through a trade-off analysis, optimizing a good strength at the most critical points such as the connections



to the suspension lines. This approach ensures that the stresses can be more safely withstood. Key design parameters are derived from this geometry (Figure [A.23]) and detailed in Table 2.13. The computed surface area corresponds to the parachute's base circle, with a correction coefficient applied for parachute inflation to derive the diameter:

$$d_{\text{main}} = \sqrt{\frac{4S_{\text{main}}}{\pi}} C_{\text{inf},\text{main}} \quad (2.5)$$

Once the surface area is computed, the parachute must also be characterized in terms of mass. So, a minimum thickness of 0.11 mm is selected for both manufacturing reasons and to ensure conservativeness with respect to common values derived from the literature. With Kevlar-29 (Table 2.12) as the chosen material, the mass can be derived as:

$$V_{\text{main,th}} = \frac{1}{3}\pi \left( \left( \frac{d_{\text{main,ext}}}{2} \right)^2 h_{\text{main,ext}} - \left( \frac{d_{\text{main}}}{2} \right)^2 h_{\text{main}} \right) \rightarrow m_{\text{main}} = V_{\text{main,th}} \cdot \rho_{\text{kev}} \quad (2.6)$$

Material	Density [ $\frac{\text{kg}}{\text{m}^3}$ ]	Tensile Strength $\sigma$ [MPa]
Kevlar-29	1440	3600

Table 2.12: Kevlar-29 Characteristics [26]

Consequently, the length of the suspension lines is defined as:

$$l_{\text{lines,main}} = d_{\text{main}} \sqrt{\frac{1 - C_{D_{\text{main}}}}{4.5} + 1.17} \quad (2.7)$$

A similar procedure can be applied to the design of the drogue parachute. However, due to the unknown velocity at drogue cut off, an alternative analysis path was chosen. The analysis considered various drogue-to-main area ratios, focusing on descent accelerations and encountered Mach values to ensure structural safety and parachute stability. A ratio of 0.0475 was selected and validated by literature. The drogue parachute sizing follows the same principles once the initial area is defined. The constants listed in Table 2.13 apply to both scenarios defined for the first stage.

	Type	$C_D$ [-]	$C_x$ [-]	$C_{\text{inf}}$ [-]	S [ $\text{m}^2$ ]	d [m]	V [ $\text{m}^3$ ]	Mass [kg]	$l_{\text{lines}}$ [m]
<b>Main</b>	Conical	0.85	1.80	0.94	1016.24	33.81	0.05	72.82	37.09
<b>Drogue</b>	Ribbed	0.35	1.20	0.63	48.27	4.94	0.0053	7.65	5.66

Table 2.13: Parachutes characteristic parameters

## 2.7.4 Pflanz Model

The forces applied to the parachutes were analyzed using the Pflanz model [23], which defines key parameters such as stabilized velocity ( $v_{\text{stab}}$ ), parachute inflation time ( $\tau_f$ ), ballistic parameter (A), and canopy inflation fill constant (n) (Figure [A.26]). After determining A, the force reduction factor (X) is derived (Chart in Figure [A.24]). Based on literature, drogue parachutes are typically deployed at 8 km and main parachutes at 3 km. These conditions were applied in the analysis:

$$v_{\text{stab,main}} = \sqrt{\frac{2(m_{\text{dry\_stage}} - m_{\text{drogue}})g(h_{\text{main open}})}{\rho_{\text{tropo}}(h_{\text{main open}})S_{\text{main}}C_{D_{\text{main}}}}} \quad (2.8)$$

$$\tau_{f_{\text{main}}} = \frac{n_{\text{main}}d_{\text{main}}}{v_{\text{stab,main}}} \rightarrow A = \frac{2(W_{\text{dry\_stage}} + 2W_{\text{main}} + 2W_{\text{drogue}})}{\rho_{\text{tropo}}(h_{\text{main open}})gS_{\text{main}}\tau_{f_{\text{main}}}v_{\text{stab,main}}} \quad (2.9)$$



Now, the force generated on the parachute during its inflation can be defined as:

$$F_{inf} = \frac{1}{2} \rho v_{stab,main}^2 S_{main} C_{x,main} X_{main}$$

	$v_{stab} [\frac{m}{s}]$	$n [-]$	$\tau_f [s]$	$A [-]$	$\mathbf{X} [-]$
<b>Main</b>	6.96	8	38.88	0.02	0.05
<b>Drogue</b>	65.43	14	1.06	2.22	0.67

Table 2.14: Pflanz model parachutes parameters

The constants defined in the current section, are presented in Table 2.14, and the computed force applied on the suspension lines is computed and reported in Figures 2.28-2.29 for the two scenarios. As can be observed, the force evolution over time for the main and drogue parachutes follows opposite trends. For the drogue parachute, the force increases due to the substantial velocity reduction, which outweighs the effects of increasing air density. Conversely, for the main parachute, the force decreases since the velocity reduction achieved is less pronounced, since the combined effects of increased air density and gravity dominate. In both cases, after a certain time, the forces stabilize. This occurs when the parachutes are fully deployed and functioning as intended. Interestingly, the force profiles show strong similarities between scenarios with and without the main engine's action. The atmospheric interaction alone provides sufficient drag, resulting in almost identical velocities in the two cases.

Since the connection points between the suspension lines and the parachutes represent critical stress areas, a conservative design was adopted, incorporating 12 lines for the main parachute and 18 lines for the drogue parachute at full deployment. This configuration ensures that the connection points and suspension lines can withstand forces up to  $6.98 \cdot 10^4 \text{ N}$  for the main parachute and  $1.05 \cdot 10^5 \text{ N}$  for the drogue system.

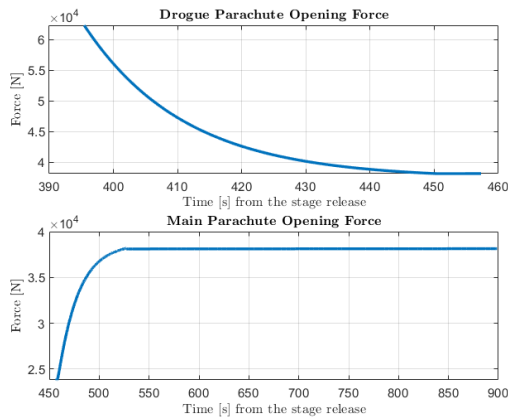


Figure 2.28: I Scenario - first stage parachutes opening forces

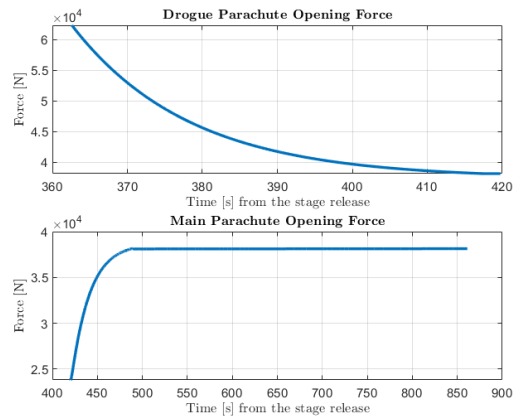


Figure 2.29: II Scenario - first stage parachutes opening forces

## 2.7.5 Splashdown

Given the **HLR-08**, an additional safety system could be designed to fully absorb the stage's residual velocity and ensure an additional level of conservativeness. To achieve this, it is necessary to calculate the deceleration distance:

$$s = \frac{v_{land,i}^2 - v_{land,f}^2}{2g_0(n_{acc}\eta_{att} - 1)} = 0.437 \text{ m} = 17.20 \text{ in} \quad (2.10)$$

Where  $v_{land,i}$  represents the velocity before the activation of the deceleration system, which, in this case, is the touchdown velocity.  $v_{land,f}$  is the desired velocity after the system is activated, ideally set to zero. The permitted deceleration ( $n_{acc}$ ) is a multiple of the gravity acceleration, here set to 8g, considering the presence of sensitive electronics on board, retrieved from Figure [A.27]. Instead  $\eta_{att}$  is the impact attenuator efficiency, here set, as typical, to 0.65. The computed value of the deceleration distance would require the use of a retrorocket system (as observable in Figure [A.25]).



## 2.7.6 Recoverability Results

This section presents the results for the main parachute of the first stage. Looking at the results obtained, the recovery of the first stage would be possible only with the main engine firing. In fact, the structure is able to sustain the maximum acceleration reached in the first scenario, with a magnitude of  $7.78g$ , touched during the interaction with the denser part of the atmosphere. Instead, in the second scenario,  $16.02g$  is reached, and as was analysed, the value cannot be withstood by the structure. The accelerations reached are shown in Figures 2.30 and 2.31. These high accelerations experienced by the first stage are primarily due to the altitude at which stage separation occurs. Here, the stage re-enters the atmosphere at high velocity, resulting in an aggressive interaction with the atmospheric layers. Another critical instant to be analysed is the aperture of the drogue parachute, in fact it causes an abrupt change in the stage orientation; this will be discussed only for the first scenario, since the recoverability in the second one has been attested as non feasible due to the atmospheric interaction. During the deployment, the stage needs to change configuration from a flight path angle of  $58.21^\circ$  to an inclination of  $90^\circ$ . Even in this case, the acceleration due to the shock has been tested and assessed as compatible with the stage resistance.

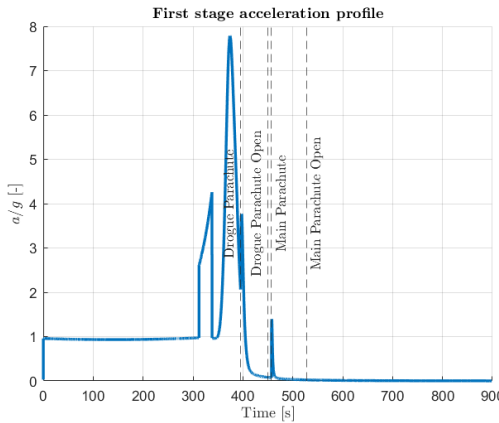


Figure 2.30: First stage acceleration profile with main engine

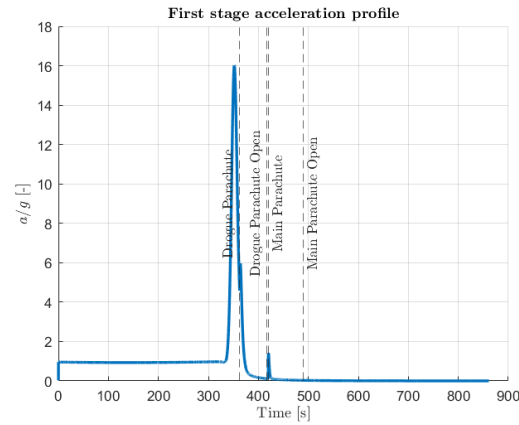


Figure 2.31: First stage acceleration profile without main engine

The second stage parachutes results are not reported due to severe accelerations (Figure 2.32) encountered in the denser atmosphere, which the structure cannot withstand. Saving propellant is more complex for the second stage as it must reach orbit and cannot be released earlier. Increasing propellant requires a higher lift-off mass, which is not feasible. Since recoverability of the second stage is not mandatory, it is considered non-recoverable. In Figure [A.28] the trajectories, path followed, velocities, and accelerations for the two analyzed cases of the first stage and one for the second stage are presented. For the latter, the two deorbiting paths that can be followed are reported in A.14.1.

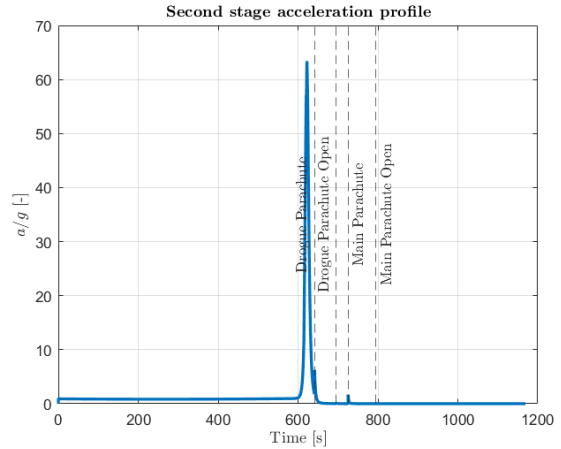


Figure 2.32: Second stage acceleration profile



## 2.8 MER and Structural Analysis

### 2.8.1 Mass Estimating Relationships

The component masses were estimated using geometric analysis, competitor comparisons and statistical relationships to ensure accuracy and avoid over- or underestimation. Statistical relationships also verified geometrically derived masses.<sup>1</sup>. The masses obtained are listed in the Table 2.15.

The external structures use Al-Li 2198, while Al 2618-T6 and Al 5456 are chosen for the LOX and RP-1 tanks due to their excellent structural properties and performance under low temperatures. The cylindrical tank sections will be welded to an external structural layer 0.002 m thick, allowing space for feeding lines; detailed design of these layers will be addressed in later design phases. The "Extra mass" listed in the Table 2.15 comprehend some mass margin of variation in the considered configuration, the pressurizer tanks which have not been sized but taken into account in the following structural considerations and the mechanical belts which aim to separates the stages and the payload. The mass estimation process was completed through an iterative approach, taking into account the results of the trajectory analysis and mass budget in terms of propellant mass and dry mass for the first and second stages, as well as lift-off mass.

Masses [Kg]	Stage I	Interstage	Stage II	Nose
Engine	300	-	52.76	-
Gimbal	17.13	-	-	-
Thrust structure	66.30	-	6.57	-
4 Tails & Fins	108.00	-	32.80	-
After Skirt	122.14	-	38.39	-
Feeding Lines	327.02	-	32.05	-
RP-1	5407.20	-	529.95	-
Tank RP-1	228.15	-	26.21	-
Intertank	102.36	-	34.22	-
LOX	12761.00	-	1250.70	-
Tank LOX	290.29	-	33.49	-
Drogue parachute	8.71	-	-	-
Main parachute	82.96	-	-	-
Structural External layer	178.97	-	13.16	-
Avionics	15	-	60	-
Wiring	14.41	-	6.01	-
Interstage	-	99.96	-	-
Forward Skirt	-	-	25.60	-
Kick stage	-	-	-	80.20
Payload	-	-	-	250.00
Fairing	-	-	-	16.26
Extra mass	40.02	-	36.00	-

Table 2.15: Mass Estimation

The purpose of this iterative process was to provide the structural analysis with more refined mass values, thereby achieving better initial estimates for structural parts thicknesses. The process was considered complete when the relative error between the estimated dry masses from the trajectory evaluation and mass budget, and the results of the mass evaluation was below 10%, satisfying one of the most relevant parameter of this pre-design phase as stated in the HoQ.

The results obtained from the mass estimation and relative error with respect to the dry masses obtained during the mass budget are reported in Table 2.16

	Propellant mass [kg]	Dry mass [kg]	$\epsilon_{SMER}$ [-]	$\epsilon_{MBUDG}$ [-]	$err_{relative}$ [%]
First Stage	18168.23	2000.81	0.099	0.089	7.02
Second Stage	1780.62	397.04	0.182	0.18	7.02

Table 2.16: Mass estimation results and relative error with respect to mass budget data

### 2.8.2 Structural analysis

The scope of the structural analysis is to verify the feasibility of the maneuvers and trajectory followed by the LV from a structural point of view. The LV was divided into 11 nodes to better comprehend the behavior of these structural parts in different phases. The nodes considered were the following:

1. **Nose:** Terminal part of the launcher where the Payload and the Kick Stage are placed, as well as the PAF considered in the mass of the Kick Stage.

<sup>1</sup>All the mass estimating relationships considered have been reported in Appendix [A.15.2]



2. **Forward skirt:** Cylindrical component which connect the nose to the cylindrical part of the LOX tank, to this component are attached the Avionics and part of the extra mass estimated for the pressurizer tanks.
3. **Tank LOX Second Stage:** This tank contains the LOX for the second stage; throughout the mission,  $C_g$  of the propellant will variate once the second stage engine is fired.
4. **Intertank Second Stage:** This cylindrical component connects the oxidizer and fuel tanks for the upper stage.
5. **Tank RP-1 Second Stage:** As well as the LOX tank, it contains the fuel for the upper phase of the trajectory.
6. **After Skirt Second Stage:** Connects the cylindrical part of the RP-1 tank to the Interstage; to this part are connected all the components related to the Second stage engine, as well as the aerodynamic fins.
7. **Interstage:** Connects the first and second stage, it contains the parachutes, avionics and the estimated mass for the pressurizer tanks.
8. **Tank LOX First Stage:** As well as the other propellant tanks, it contains the LOX which  $C_g$  variation has been evaluated to better assess the moments and forces acting on the launcher.
9. **Intertank First Stage:** Connect the two propellant tanks of the first stage.
10. **Tank RP-1 First Stage:** Contains the fuel used in the early phases of the mission.
11. **After Skirt First Stage:** To this component are attached all the parts relative to the first stage main engine and the aerodynamic tails.

The nodes placement is depicted in Figure [A.40]. In the node evaluation the feeding lines and the wiring masses have been considered as distributed loads. For all the cases considered, the load evaluation was performed by balancing forces and moments acting on each component, accounting for the interaction between adjacent sections. Consequently, the results are primarily presented as variations between two values corresponding to the boundary values of each component, ensuring internal equilibrium.<sup>2</sup>

The structural analysis was made by considering several cases which are the most demanding from a stress point of view in terms of axial compression, bending moment and elastic stability or buckling.

### 2.8.3 On Ground Condition

The analysis was conducted by considering the most demanding ground conditions as those in which the launcher is attached to the carrier prior to takeoff, laying horizontally.

Pre-attachment conditions were deemed less structurally demanding due to the compact structure's adaptability. Various transport methods and configurations with multiple supports can distribute loads more effectively, reducing stress compared to when the fully assembled launcher is attached to the carrier with a two-junction-point system, which was the one chosen for the analysis, similarly to the baseline case (Figure [A.39]).

Each junction provides two constraint reactions and one constraint moment, applied at the interstage and the intertank sections of the first stage.

The on ground condition considered are two: with not-pressurized tanks and with pressurized tanks. The first happens when the propellant are loaded into the tanks but not yet pressurized and the pressurized case is considered as the nominal during the early phases of the mission up until the ignition of the first engine.

In this two cases the loads and bending moments are only due to the weight of the structure. The axial loads are negligible because no aerodynamic contribution of the wind has been considered being the launcher horizontal and not far from ground. In the following loads analysis the convention used will be: the axial loads positive towards the main engine, shear loads positive upwards and bending moments positive in the same direction of the pitch maneuver. The overall representation of the loads and bending moments is the following:

<sup>2</sup>These variations do not necessarily reflect the actual load or bending distribution on the structure but are included for completeness and continuity in the representations used during the analysis, or the actual representation of the loads and bending distribution, a deeper knowledge of the internal design of the LV, should be required.

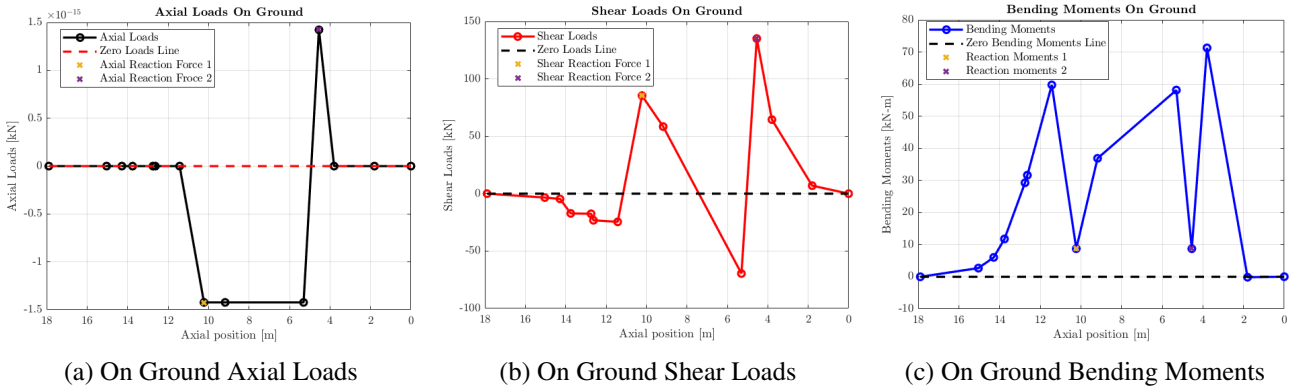


Figure 2.33: Loads and Bending Moments analysis of On Ground conditions

The reaction forces and moment computation was obtained by solving a 6 variables system to guarantee the equilibrium of forces and moment in each component and satisfy the constraint of having 0 loads and bending moment at the boundaries of the launcher.

#### 2.8.4 In-Flight Condition

For the In-flight condition, the contribution of the aerodynamic surfaces has a relevant role. For this reason starting from data expressing the state and the attitude of the launcher, a model of the atmospheric environment around the LV is obtained. Dynamic pressure effects on the LV are analyzed for components with varying diameters (e.g., nose and interstage), fins and tails. Using aerodynamic loads and global force equilibrium, the axial loading factor ( $n_x$ ) and lateral loading factor ( $n_z$ ) are determined. From  $n_z$  the Thrust required to counteract resulting moment is calculated, followed by the axial contribution based on the total available Thrust.

The first case considered involves the maneuver during which the structure is subjected to a range of accelerations. In the transient phase between detachment from the carrier and the nominal trajectory, the condition where the maximum angular acceleration occurs was analyzed, to determine the loads and stresses applied to the structure as a result of rapid maneuvering. The contribution of the aerodynamic surfaces has been evaluated based on the data of the position and time in which the maximum angular acceleration is reached.

	Time [s]	$v$ [m/s]	$h$ [Km]	$M$ [-]	$q$ [Pa]	$a_{angular}$ [rad/s <sup>2</sup> ]
<b>Maneuver</b>	9	210.80	11.76	0.71	5672.31	1.79

Table 2.17: Maneuver data

The second case examined was the max-q condition (Table 2.18) in which the dynamic pressure reaches its maximum during the ascent of the LV. From the Figure 2.34 it is worth noticing that in correspondence of axial position 0, the loads and bending moments are equal to the corresponding effect of the thrust applied to the structure in the corresponding position of the gimbal. The axial contribution of the thrust  $T_n = -256.46$  kN, the shear and bending moment  $T_z = 42.77$  kN and  $M_z = -19.89$  kNm.

	Time [s]	$v$ [m/s]	$h$ [Km]	$M$ [-]	$q_{max}$ [Pa]
<b>Max q</b>	22.2	315.66	15.29	1.07	7947.4

Table 2.18: Max q data

The third condition is the one where the product between the dynamic pressure and the angle of attack of the vehicle is maximum, this condition happens slightly before the q-max condition but in some components the difference between this two cases is the cause for a re-size of the tank thicknesses.

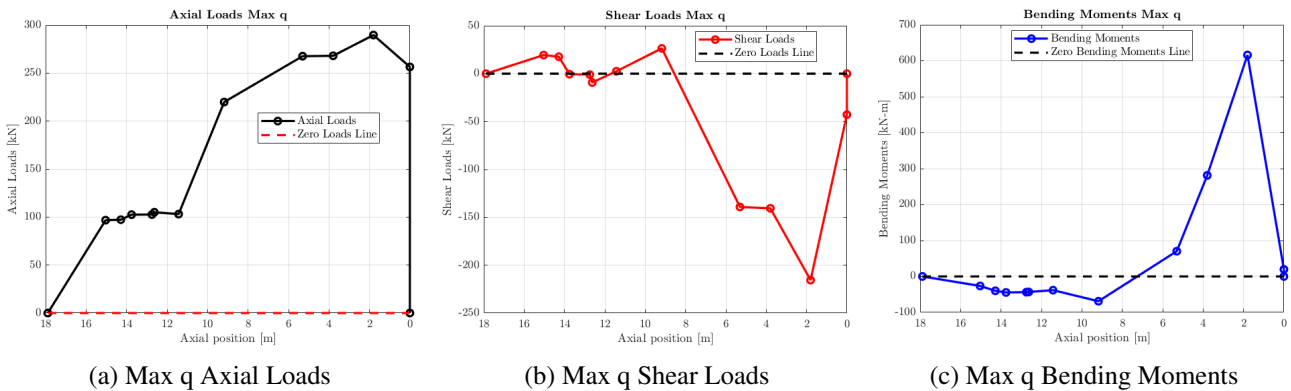


Figure 2.34: Loads and Bending Moments analysis of Max q condition.

	Time [s]	$v$ [m/s]	$h$ [Km]	$M$ [-]	$q\alpha_{max}$ [Pa · rad]
<b>Max <math>q\alpha</math></b>	17.5	294.95	14.26	0.995	1235.50

Table 2.19: Max  $q\alpha$  data

The fourth and last condition of the ascending trajectory considered, where the first stage main engine cut off happens, followed by stages separation. The shutdown of the main engine will result in a deceleration of magnitude  $\Delta a = 5.98g$  which would cause some effect on the structure due to the inertia of the components. For stages and payload separation, it was considered a mechanical separation provided by Advanced Lightband from Rocket Lab [27]<sup>3</sup>. This choice was driven by the low-shock performances, high reliability and very low weight. The weight and performance of the ALB have been estimated by its current performances with lower diameter configurations. It is considered the requirement of obtaining a minimum relative velocity  $\Delta V = 3m/s$  [28] in order to guarantee a safe separation, avoiding further interactions between the stages. A  $\Delta V = 3.85m/s$  was obtained (in Appendix [A.16]), along with an axial deceleration transmitted to the first stage of  $a = -2.59m/s^2$ , which has been considered in the load analysis. The case of the second-stage main engine cut-off has not been analyzed because the occurring accelerations are relatively less important.

The final conditions analyzed were considered for the re-entry of the first stage after the re-ignition of the main engine to slow the descent. Both of them were analyzed starting considering the state and attitude of the falling stage and evaluating them for the aerodynamic model as considered for the previous cases. The verification of the conditions feasibility in terms of structure's thickness was done by following the same process as for the previous case. Firstly it was analyzed the structural safety of the first stage at the insertion in the Earth's atmosphere, which was considered and verified to happen with the data reported in Table 2.20.

The second considered instant was the opening of the drogue parachute deployed from the first stage. This condition was selected due to the extremely high angular acceleration and axial deceleration it involves, which impose substantial stresses on the structure, possessing considerable inertia and aerodynamic loads during re-entry. Given the data reported in Table 2.21 from the re-entry analysis, in correspondence of the deployment of the drogue parachute, the aerodynamics loads were evaluated as for the previous cases. The maximum force that could be applied by the parachute on the structure would required a loading factor of  $4.4g$ <sup>4</sup> which is much higher with respect to the  $3.42g$  loading factor required by the chosen configuration in the given conditions.

<sup>3</sup>This system does not currently accommodate the 1.2 m diameter of the separation section between stages, but it is expected that within four years, the range of applicable diameter will support larger configurations.

<sup>4</sup>This maximum value was obtained by considering the effect on the structure of different magnitude of deceleration, developing the loads and stress analysis as in the previous cases, but only considering the empty mass of the first stage.

$v$ [m/s]	$h$ [km]	$M$ [-]
1746.31	21.39	5.80

Table 2.20: Atmospheric entry



Once verified the feasibility of the maneuver the analysis was carried out with the load analysis (reported in Appendix [A.41]) and the required thickness evaluation.

	$v$ [m/s]	$h$ [km]	$M$ [-]	$a_{angular}$ [rad/s <sup>2</sup> ]
<b>Parachute Deployment</b>	404.58	7.99	1.31	4.18

Table 2.21: Parachute Deployment data

### 2.8.5 Thickness analysis

For all structural components, following the mass estimation phase and load evaluation, the stress behaviour was analyzed. The stresses were evaluated by considering the highest absolute value of axial, shear and bending moment of each component, through its length, to keep a more conservative approach with respect to the evaluations at the bottom of each structural segment. For each component, the stresses considered included those generated by coupling of axial loads with bending loads, and shear loads, although the latter were always significantly lower compared to the others. Buckling, or elastic stability, was also analyzed for each component and was found to be the critical sizing condition for several of them. For pressurized components, additional factors were considered due to the presence of static and dynamic pressures within the tanks. After computing a set of thicknesses that satisfied all stress conditions across the cases considered, a tuning process (Appendix [A.17]) was performed to refine the thickness selection for each structural component.

The Results obtained by this tuning process are reported in the Table A.3. All the components have a Margin of Safety higher than 0 which is the required constraint for design feasibility. The RP-1 first stage tank could allow a further reduction of 0.5 mm in thickness but this would not leave enough margin of safety.

In conclusion of this analysis the structural safety of all the cases previously listed, for all the structural components was satisfied with different margins.

Component	Minimum MS	Case	Selected Thickness [mm]	Thickness Margin [mm]	Stress Condition
Nose	11.08	Manoeuvre	2	0.42	Buckling
Fwd Skirt	8.54	Manoeuvre	2	0.31	Buckling
Tank LOX 2 <sup>ND</sup>	1.87	MECO	2	0.36	Hoop
Intertank 2 <sup>ND</sup>	5.54	Manoeuvre	2	0.026	Buckling
Tank RP-1 2 <sup>ND</sup>	2.01	MECO	2	0.35	Hoop
Aft Skirt 2 <sup>ND</sup>	2.96	Manoeuvre	3	0.19	Buckling
Interstage	4.84	Manoeuvre	3.5	0.19	Buckling
Tank LOX 1 <sup>ST</sup>	2.50	Manoeuvre	3.5	0.008	Buckling
Intertank 1 <sup>ST</sup>	4.23	Parachute Deploying	4	0.39	Buckling
Tank RP-1 1 <sup>ST</sup>	2.28	Max q $\alpha$	4	0.51	Buckling
Aft Skirt 1 <sup>ST</sup>	3.11	Parachute Deploying	4	0.11	Buckling

Table 2.22: Minimum MS and Thickness Data for Structural Components

### 2.8.6 Further design steps

Other important cases which may results significative for the sizing of some structural components may be the following, which in this pre-design phase were not considered:

- **In Flight with carrier:** The current aerodynamic model is too simplified, neglecting important effects from the carrier's presence. To address this, a more complex numerical model is required. This advanced model would simulate the environment more accurately, capture the specific conditions under analysis, and verify the stress behavior on the LV. It ensures better alignment with real-world aerodynamic influences.
- **First Stage Splashdown:** For a similar reason, due to complexity of the condition in analysis, a more precise model is required to better understand the impact and interaction of the first stage with water.

# Conclusions

## 3.1 Cost analysis

In conclusion, a brief cost analysis and stages reusability assessment can be performed. For this study, an operational life of 5 years for the VIPER-1 launchers series has been assumed, with a minimum of 3 launches per Year (always considering the nominal mission).

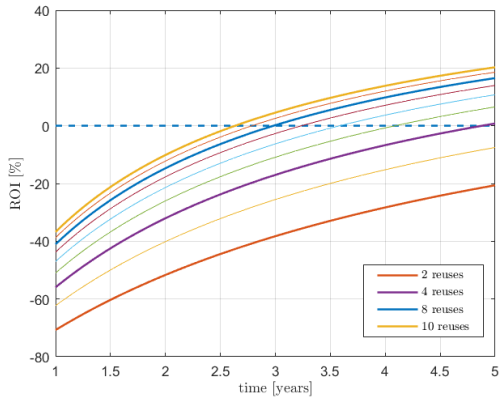


Figure 3.1: ROI over the planned operative time

Using the TRANSCOST model developed by Dietrich E. Koelle [29], a total cost per launch has been estimated, which includes Indirect and Direct Operational Costs (IOC and DOC), reusable components refurbishment costs and Vehicle development and production costs amortized in the total operational life (process fully described in Appendix [A.18]). The final cost is obtained in Man-Years (MY), a universal value independent from currency and inflation; multiplying by the actual US annual cost of work [30], the cost per launch in dollars (\$) is obtained. Then, a price for launch per kg of payload is estimated adding a percentage to the Pegasus one [31]. The ROI index is computed as:

$$ROI = \frac{price/kg \cdot m_{pay} - total\ cost}{total\ cost} \quad (3.1)$$

The Vehicle production costs decrease with reuses of the first stage and its relative engine, lowering the total cost per launch. To reenter in the initial investment, the minimum number of four reuses of the same components has been found (Figure 3.1), corresponding to a total cost per launch of 26 M\$ (in line with Pegasus-XL). A greater number of reuses will certainly lower the cost, but the higher cost of refurbishment of over-reused components has not been considered in the study.

## 3.2 Maneuver & Risk Assessment

As initially explained, the key driver for this preliminary design was to make the unpowered maneuver efficient and advantageous. After analyzing all phases, the following considerations were drawn:

- This maneuver could be employed to achieve any launch inclination that the carrier aircraft cannot reach, thereby reducing transverse loads
- The time to reach orbit was found (Section 2.4.1) to be shorter compared to LauncherOne
- In the absence of robust control, the system fails due to the presence of significant angular accelerations
- Thrust vectoring is necessary because the fins only are not sufficient to efficiently maneuver the rocket
- An incorrect deployment timing of the tail fins could compromise the mission
- The low TRL of the maneuver represents a higher risk for the client relying on us



### 3.3 Requirement Assessment

Regarding the conceptual design phase for the VIPER-1 launcher, a final requirements assessment has been performed. Table 3.1 addresses the HLRs as fulfilled/non-fulfilled and defines a consequent direction of improvement.

Further developments, currently constrained by the short time-to-market, could include the implementation of movable rear fins, requiring the design of a dedicated mechanism to make them both deployable and movable. Additionally, the study of a backboost system for reentry could potentially enable the recovery of both stages, thus guaranteeing the 100% recoverability of the first stage.

Requirement	Fulfillment	Direction of improvement
HLR-01	Yes	–
HLR-02	Yes	–
HLR-03	Yes	–
HLR-04	Yes	Developing a robust control system to ensure a smooth transient during the drop phase and to minimize uncertainties in orbit insertion
HLR-05	Yes	–
HLR-06	Partially	Further iterations will be necessary to preserve stage reusability
HLR-07	Yes	Evaluating the implementation of a thermal protection system for the second stage re-entry and a lofted maneuver exploiting more propellant
HLR-08	Yes	Building an in-house engine would allow to experiment different propellant combinations
HLR-09	Yes	–
HLR-10	Yes	–

Table 3.1: Requirements fulfilment and directions of improvement

The integration of innovative aerodynamic maneuver and a dedicated kick stage for orbital insertion shows a well-rounded approach in optimizing performance while maintaining cost-effectiveness. Ultimately, VIPER-1 embodies a forward-thinking solution to reducing reliance on traditional ground-based systems, paving the way for more flexible and efficient satellite deployment missions.

At the conclusion of the conceptual design, it has to be underlined that the structural analysis for the feasibility of the re-entry maneuver imposes two different developments, one for each scenario (2.7.1). In the case of a powered re-entry, a successive iteration must take into account a larger amount of propellant, requiring an overall re-definition of the masses and subsequently a re-design of the other subsystems. In the condition of no re-ignition of the main engine, the structural safety has to be verified. Very significant changes will be required in the first stage structures, as reported in the tables in Appendix A.19.1. The unpowered re-entry would cause an increment of the structural components thickness and so a general increase in the masses; as a consequence the structural error would overcome 10%. Again a further iteration will be necessary, leading to re-considerations in the masses, in order to reduce the error.

# Bibliography

- [1] *Atmospheric Model: NRLMSISE-00 - MATLAB and Simulink*. Accessed: 2024-12-08. URL: <https://it.mathworks.com/help/aerotbx/ug/atmosnrlmsise00.html>.
- [2] *Flux, Solar, and Geomagnetic Indices - MATLAB and Simulink*. Accessed: 2024-12-08. URL: <https://it.mathworks.com/help/aerotbx/ug/fluxsolarandgeomagnetic.html>.
- [3] Virgin Orbit. *LAUNCHERONE SERVICE GUIDE*. Tech. rep. URL: <https://newspaceeconomy.ca/wp-content/uploads/2022/06/launcherone-service-guide-august-2020.pdf>.
- [4] Rocket Lab. *Electron Overview*. Tech. rep. URL: <https://www.rocketlabusa.com/assets/Uploads/Electron-Payload-User-Guide-7.0.pdf>.
- [5] *Executor Rocket Engine - ARCA Space (Archived)*. Accessed: 2024-12-08. URL: <https://web.archive.org/web/20141009042218/http://www.arcaspace.com/en/executor.htm>.
- [6] URL: <http://www.braeunig.us/space/specs/pegasus.htm>.
- [7] *LOX/Kerosene*. Accessed: 2024-12-08. URL: <http://www.astronautix.com/l/loxkerosene.html>.
- [8] *LOX/LH2*. Accessed: 2024-12-08. URL: <http://www.astronautix.com/l/loxlh2.html>.
- [9] *LOX/LCH4*. Accessed: 2024-12-08. URL: <http://www.astronautix.com/l/loxlch4.html>.
- [10] *H2O2/Kerosene Propellant - Encyclopedia Astronautica*. Accessed: 2024-12-08. URL: <http://www.astronautix.com/h/h2o2kerosene>.
- [11] *Overview on Hybrid Propulsion*. Accessed: 2024-12-08. URL: [https://www.researchgate.net/publication/258491207\\_Overview\\_on\\_hybrid\\_propulsion/figures?lo=1](https://www.researchgate.net/publication/258491207_Overview_on_hybrid_propulsion/figures?lo=1).
- [12] *EUCASS Conference Document*. Accessed: 2024-12-08. URL: <https://www.eucass.eu/component/docindexer/?task=download&id=6118>.
- [13] *Executor (rocket engine)*. Accessed: 2024-12-08. URL: [https://en.wikipedia.org/wiki/Executor\\_\(rocket\\_engine\)](https://en.wikipedia.org/wiki/Executor_(rocket_engine)).
- [14] *Rutherford (rocket engine)*. Accessed: 2024-12-08. URL: [https://en.wikipedia.org/wiki/Rutherford\\_\(rocket\\_engine\)](https://en.wikipedia.org/wiki/Rutherford_(rocket_engine)).
- [15] *Discussion on NASA SpaceFlight Forum - Topic: Rocket Engine Development*. Accessed: 2024-12-08. URL: <https://forum.nasaspacesflight.com/index.php?topic=51764.0>.
- [16] Eugene L. Fleeman. *Tactical Missile Design*. Ed. by Joseph A. Schetz. Second. AIAA Education Series. Reston, VA, USA: American Institute of Aeronautics and Astronautics, Inc., 2006.
- [17] Pavlos Kakouris. “Design of a high-angle pointing mechanism for thrust vector control”. MA thesis. Politecnico di Milano, 2022-23. URL: <https://hdl.handle.net/10589/209754>.
- [18] *Aerodynamic and Aerothermodynamic Analysis of Space Mission Vehicles*. Accessed: 2024-12-08. URL: [https://www.researchgate.net/publication/276271792\\_Aerodynamic\\_and\\_Aerothermodynamic\\_Analysis\\_of\\_Space\\_Mission\\_Vehicles](https://www.researchgate.net/publication/276271792_Aerodynamic_and_Aerothermodynamic_Analysis_of_Space_Mission_Vehicles).
- [19] *AIAA Paper: 10.2514/3.45483*. Accessed: 2024-12-08. URL: <https://arc.aiaa.org/doi/10.2514/3.45483>.
- [20] *Aerothermodynamics Course - TFAWS 2012 Proceedings*. Accessed: 2024-12-08. URL: <https://tfaws.nasa.gov/TFAWS12/Proceedings/Aerothermodynamics%20Course.pdf>.



- [21] *Politecnico di Torino Thesis: Detailed Analysis and Research*. Accessed: 2024-12-08. URL: <https://webthesis.biblio.polito.it/32280/>.
- [22] *Material Property Data Sheet - MatWeb*. Accessed: 2024-12-08. URL: <https://www.matweb.com/search/DataSheet.aspx?MatGUID=0cd1edf33ac145ee93a0aa6fc666c0e0>.
- [23] Theo W. Knacke. *Parachutes Recovery Systems Design Manual*. 1991, Chapter 5. DOI: <https://doi.org/10.1017/S0001924000026725>. URL: <https://apps.dtic.mil/sti/tr/pdf/ADA247666.pdf>.
- [24] *Forces During Recovery - nasa.gov*. URL: <https://www.grc.nasa.gov/www/k-12/VirtualAero/BottleRocket/airplane/rktrecv.html>.
- [25] *Design and Testing of High-Performance Parachutes*. URL: <https://www.sto.nato.int/publications/AGARD/AGARD-AG-319/AGARD-AG-319.pdf>.
- [26] *KEVLAR ARAMID FIBER TECHNICAL GUIDE*. URL: [https://www.dupont.com/content/dam/dupont/amer/us/en/safety/public/documents/en/Kevlar\\_Technical\\_Guide\\_0319.pdf](https://www.dupont.com/content/dam/dupont/amer/us/en/safety/public/documents/en/Kevlar_Technical_Guide_0319.pdf).
- [27] *2003336 Advanced Lightband User's Manual*. URL: <https://www.rocketlabusa.com/assets/Uploads/2003336F-Advanced-Lightband-Users-Manual.pdf>.
- [28] *FLIGHT SEPARATION MECHANISMS*. Accessed: 2024-12-07. URL: <https://ntrs.nasa.gov/api/citations/19710019510/downloads/19710019510.pdf>.
- [29] Dietrich E. Koelle. "The transcost-model for launch vehicle cost estimation and its application to future systems analysis". In: *Acta Astronautica* 11.12 (1984), pp. 803–817. ISSN: 0094-5765. DOI: [https://doi.org/10.1016/0094-5765\(84\)90100-0](https://doi.org/10.1016/0094-5765(84)90100-0). URL: <https://www.sciencedirect.com/science/article/pii/0094576584901000>.
- [30] W. Costa D. Edberg. *Design of Rockets and Space Launch Vehicles*. American Institute of Aeronautics & Astronautics, 2022. Chap. 17.
- [31] D.E. Koelle. *Handbook of Cost Engineering for Space Transportation Systems with Transcost 7.0: Statistical-analytical Model for Cost Estimation and Economical Optimization of Launch Vehicles*. TCS-TR-168/00. TransCostSystems, 2000. URL: <https://books.google.it/books?id=CKXYngEACAAJ>.
- [32] *Ballistics: Ogives and Bullet Shapes (Part 1)*. Accessed: 2024-12-08. URL: <https://www.mathscinotes.com/2011/01/ballistics-ogives-and-bullet-shapes-part-1/>.
- [33] *Research Paper from IJISRT: IJISRT21JUL954*. Accessed: 2024-12-08. URL: <https://ijisrt.com/assets/upload/files/IJISRT21JUL954.pdf>.
- [34] James S. Barrowman. "The Practical Calculation of the Aerodynamic Characteristics of Slender Finned Vehicles". Submitted in partial fulfillment of the requirements for the degree of Master of Science in Aerospace Engineering. MA thesis. Washington, D.C.: The Catholic University of America, Mar. 1967. URL: <https://ntrs.nasa.gov/search.jsp?R=20010047838>.
- [35] Sampo Niskanen. *OpenRocket Technical Documentation*. Tech. rep. Version 13.05. Based on the Master's thesis: "Development of an Open Source model rocket simulation software". OpenRocket Project, May 2013. URL: <http://openrocket.sourceforge.net/>.
- [36] Donald L. Edberg and Guillermo Costa. *Design of Rockets and Space Launch Vehicles*. Second Edition. AIAA Education Series. Includes bibliographical references and index. Reston, Virginia: American Institute of Aeronautics and Astronautics, Inc., 2022. ISBN: 978-1-62410-641-5. URL: <https://arc.aiaa.org>.
- [37] *NASA Technical Report: 19890017745*. Accessed: 2024-12-08. URL: <https://ntrs.nasa.gov/api/citations/19890017745/downloads/19890017745.pdf>.
- [38] *OSPIC Report: A Study on Spacecraft Propulsion*. Accessed: 2024-12-08. URL: <https://ostad.nit.ac.ir/payaidea/ospic/file8973.pdf>.



- [39] *Nose Cone Tip Thermal Analysis - MIT Rocket Team Wiki*. Accessed: 2024-12-08. URL: <https://wikis.mit.edu/confluence/display/RocketTeam/Nose+Cone+Tip+Thermal+Analysis>.
- [40] W. Costa D. Edberg. *Design of Rockets and Space Launch Vehicles*. American Institute of Aeronautics & Astronautics, 2022. Chap. 8.
- [41] *Development of a Mass Estimating Relationship Database for Launch Vehicle Conceptual Design*. URL: <https://www.yumpu.com/en/document/read/26559325/development-of-a-mass-estimating-relationship-database-for->.
- [42] W. Costa D. Edberg. *Design of Rockets and Space Launch Vehicles*. American Institute of Aeronautics & Astronautics, 2022. Chap. 10.





# Appendix A

## A.1 House Of Quality

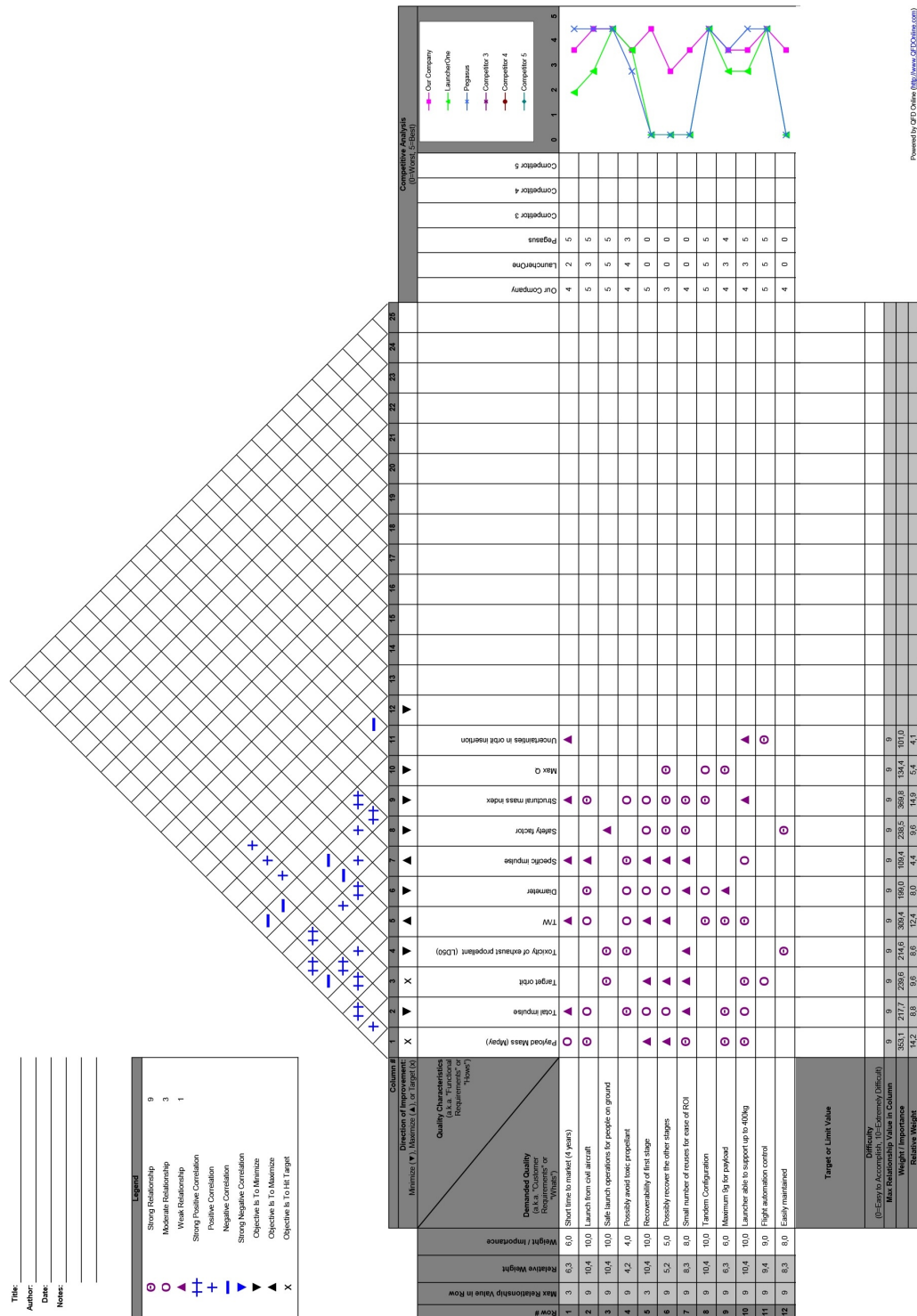


Figure A.1: HoQ



## A.2 Technical loop

The technical loop starts with the analysis of the mission, calculating the required propellant mass to achieve the objectives. This energy budget is a key input for the sizing of the propulsion subsystem, including the tanks sizing. Once the tanks dimensions have been determined, the overall shape and length of the rocket can be determined. This process is guided and refined using the baseline design as a reference, ensuring consistency with the initial assumptions and constraints. The dimensions, in turn, are required for the aerodynamic analysis that will provide critical insights into how to design the structure, particularly in the most stress-loaded areas. This step also allows the decomposition of the entire launcher into various subsystems, with their respective masses being calculated (MER). If the total mass of these subsystems aligns with the initial estimates derived during the staging analysis within a reasonable error range, the process can proceed to trajectory refinement. Finally, the recovery system is designed, to ensure safe and efficient retrieval of reusable components, safeguarding both the vehicle's structure and civilians on the ground.

## A.3 $\Delta V$ Budget

$$v = \sqrt{\frac{\mu_{\text{Earth}}}{R_{\text{orbit}}}} = 7.67 \text{ km/s} \quad (\text{A.1})$$

where  $\mu_{\text{Earth}}$  is Earth's gravitational constant, and  $R_{\text{orbit}}$  is the orbital radius, which is the sum of Earth's radius and the target altitude.

$$a = \sqrt{\gamma R T} = 295 \text{ m/s} \quad (\text{A.2})$$

where  $T$  is the temperature at 12 km altitude, estimated as -56°C.

## A.4 Mass Budget

$$\left\{ \begin{array}{l} M_2 = \frac{M_{\text{pay}} \left( e^{\frac{\Delta V_{\text{design},2}}{T_{\text{sp},2}^{80}}} - 1 \right)}{1 - \epsilon_{s,2} e^{\frac{\Delta V_{\text{design},2}}{T_{\text{sp},2}^{80}}}} \\ M_1 = \frac{(M_2 + M_{\text{pay}}) \left( e^{\frac{\Delta V_{\text{design},1}}{T_{\text{sp},1}^{80}}} - 1 \right)}{1 - \epsilon_{s,1} e^{\frac{\Delta V_{\text{design},1}}{T_{\text{sp},1}^{80}}}} \\ M_{s,2} = \epsilon_{s,2} M_2, \quad M_{s,1} = \epsilon_{s,1} M_1 \\ M_{p,1} = M_1 - M_{s,1}, \quad M_{p,2} = M_2 - M_{s,2} \\ M_0 = M_1 + M_2 + M_{\text{pay}} \end{array} \right.$$

## A.5 Tank sizing

$$L_{\text{tank}} = \frac{V_{\text{tot}} - \frac{4\pi}{3} a^2 b}{\pi a^2} \quad (\text{A.3})$$



## A.6 Nose Cone Design

The profile of the nose cone is generated using a circular segment with dimensions  $6 \times D$  [32], which is tangent to the base of the nose cone. The popularity of this shape arises from its simplicity in construction, as illustrated in Figure A.2. This design combines a spherical section at the tip with the tangent ogive shape of the main body. The spherical section smoothens the leading edge, improving thermal resistance and load distribution. Given that the length of the nose cone ( $L$ ) is fixed, the shape parameters must be determined by solving a linear system of four equations with four unknowns. This ensures the geometric and aerodynamic constraints are satisfied while maintaining the fixed length.

$$\begin{cases} X_t = X_c - \sqrt{r_n^2 - Y_t^2} \\ Y_t = \frac{r_n(\rho - R)}{\rho - r_n} \\ X_c = L - \sqrt{(\rho - r_n)^2 - (\rho - R)^2} \\ X_a = X_c - r_n \end{cases} \quad (A.4)$$

where:

- $X_c$  is the centre of the spherical nose
- $L$  represents the length of the nose cone
- $X_t$  represents the X-coordinate of the tangency point
- $Y_t$  is the Y-coordinate of the tangency point
- $r_n$  is the ogive bluntness radius

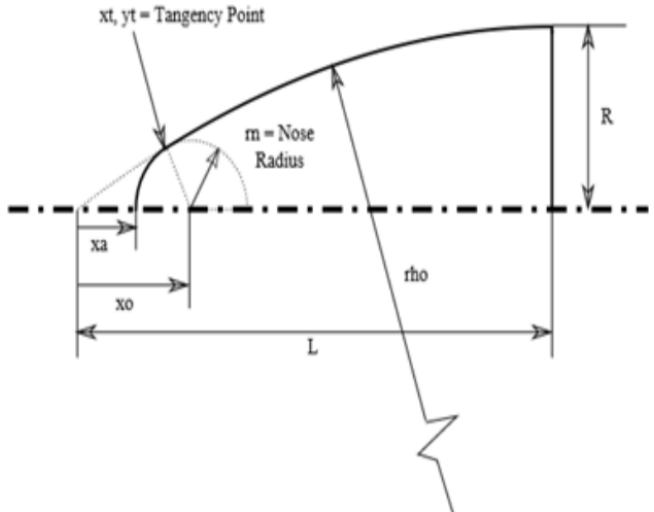


Figure A.2: Blunt tangent ogive nose cone profile [33]

## A.7 Aerodynamics models

### A.7.1 $C_n$ model

The total  $C_n$  is obtained through the components build-up method, evaluating contributes given by body, fins and tails and putting them together after being opportunely weighted. In the following sections, models adopted for each of them will be discussed.

#### Body $C_n$

Viper-1 in Stack 1 configuration is characterized, excluding aerodynamics appendixes, by a cylindrical modular shape having an initial diameter of 1.8 m for the first stage, a 1.2 m for the second stage connected by a slender shoulder long 2.25 m. Then, the launcher terminate with a Blunted Tangent Ogive nose. These features classify the body as a non-lifting body, which contribute to the  $C_n$  are mainly due to the previously mentioned nose and shoulder. Anyway in this discussion due to the slenderness of the shoulder its contribution in terms of normal force is assumed to be almost negligible, according to that only the nose contribution has been modeled. This has been done according to Allen model which is based on Slender body Theory and cross flow theory [16]:

$$|Cn| = \left| \left( \frac{a}{b} \right) \cos^2(\phi) + \left( \frac{b}{a} \right) \sin^2(\phi) \right| \left[ \left| \sin(2\alpha) \cos\left(\frac{\alpha}{2}\right) \right| + 2 \left( \frac{L}{D} \right) \sin^2(\alpha) \right] \quad (A.5)$$

Where  $\phi$  is assumed to be 0 and  $a/b$  ratio assumed to be 1 due to the symmetry of the body. This model is valid for bodies characterized by an  $l/d$  higher than 5, so it is well suited for the VIPER-1 which, at last iteration, has an  $l/d = 9.93$ . In figure A.3 the body contribute to  $Cn$  is shown:

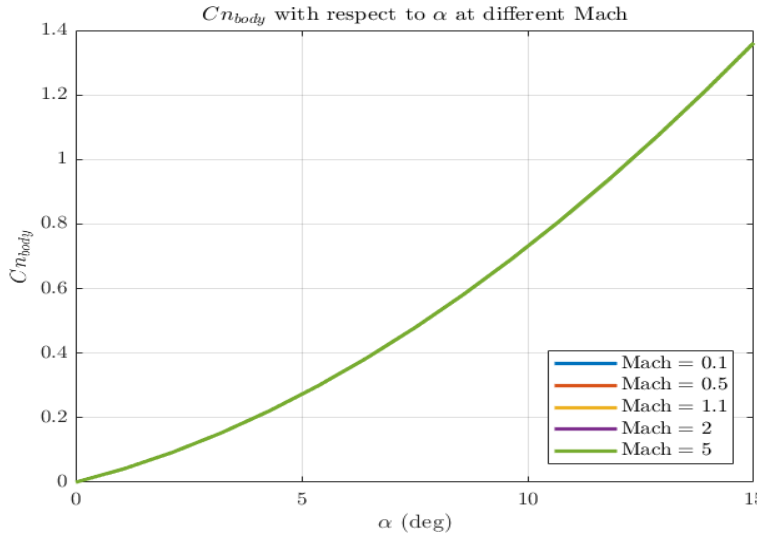


Figure A.3:  $Cn$  body contribution for significative Angle of attacks

As predicted this contribution is not affected by Mach variation.

### Fins and Tails $Cn$

For what concern fins and tails both have been designed using two different models, one for High supersonic condition and one for Subsonic and Low Subsonic condition. The following equations explicate the dependence of the  $Cn$  by the geometrical parameters of the aerodynamic appendixes through  $AR$  and local AoA through  $\alpha_{surf}$  [16]. In particular:

$$\lambda = \frac{Ct_{surf}}{Cr_{surf}} \quad (\text{A.6})$$

$$AR = \frac{2b_{surf}}{[(1+\lambda)Cr_{surf}]} \quad (\text{A.7})$$

$$\alpha_{surf} = \alpha + \delta_{surf} \quad (\text{A.8})$$

- High Supersonic condition:  $M^2 > 1 + [8/(\pi AR)]^2$

For this condition the linear wing theory plus Newtonian impact theory adopted lead to :

$$|Cn_{surf}| = \left[ \frac{4 |\sin(\alpha_{surf}) \cos(\alpha_{surf})|}{(M^2 - 1)^{\frac{1}{2}}} + 2 \sin^2(\alpha_{surf}) \right] \left( \frac{S_{surf}}{S_{ref}} \right) \quad (\text{A.9})$$

- Subsonic and Low Supersonic condition:  $M^2 < 1 + [8/(\pi \cdot AR)]^2$

For this condition the slender wing theory plus Newtonian impact theory that has been adopted lead to:

$$|Cn_{surf}| = \left[ \left( \frac{\pi \cdot AR}{2} \right) |\sin(\alpha_{surf}) \cos(\alpha_{surf})| + 2 \sin^2(\alpha_{surf}) \right] \left( \frac{S_{surf}}{S_{ref}} \right) \quad (\text{A.10})$$

It is important to highlight that this models combination allow to predict with high accuracy the overall behaviour of  $Cn_{surf}$  for  $AR \leq 3$ , overshooting this threshold the slender theory start to lack in accuracy. Anyway, having an  $AR_{fin}=2$  and  $AR_{tail}=2.93$  computations int this analysis are not afflicted by this problem. In figure



A.4 and A.5 contribution to the total  $Cn$  are shown:

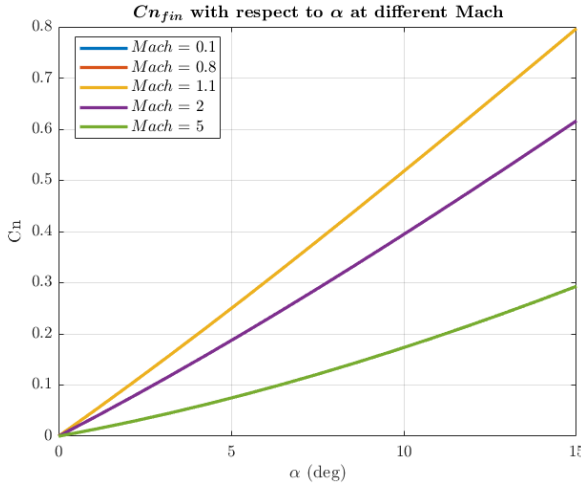


Figure A.4:  $Cn_{fin}$  at different  $\alpha$

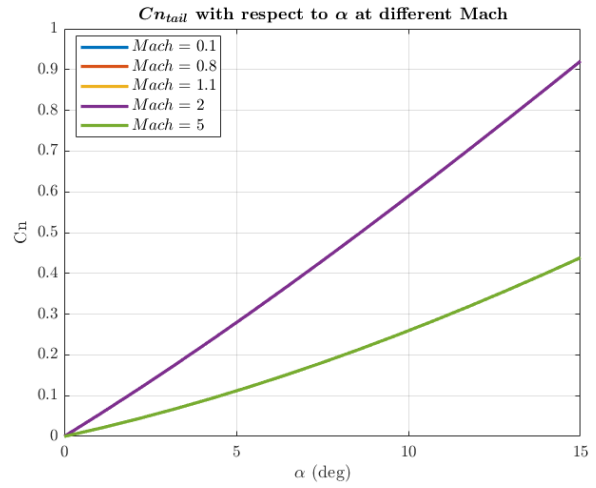


Figure A.5:  $Cn_{tail}$  at different  $\alpha$

What is represented in those figure is consistent with the model, indeed in A.4 curves of  $Cn_{fin}$  at  $M = 0.1$  and  $M = 0.8$  are overlapped to the one at  $M = 1.1$  because they are subjected to the condition of Subsonic and Low-supersonic flow where according to Equation A.9 no dependence on Mach is present. Same can be said about A.5. So, according with models and initial hypothesis, the resulting  $Cn$  of the whole system is:

$$Cn_{tot} = Cn_{tail} + Cn_{fin} + Cn_{body} \quad (\text{A.11})$$

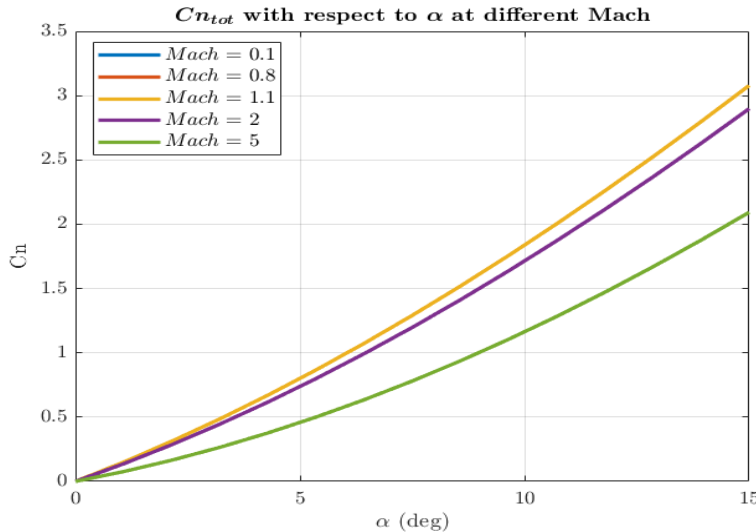


Figure A.6:  $Cn_{tot}$  behavior for significative Angle of attacks

Once obtained the global value of  $Cn$ , model have been validated comparing the results with the aeroplot from *Ras Aero 2* which is the one in A.7.

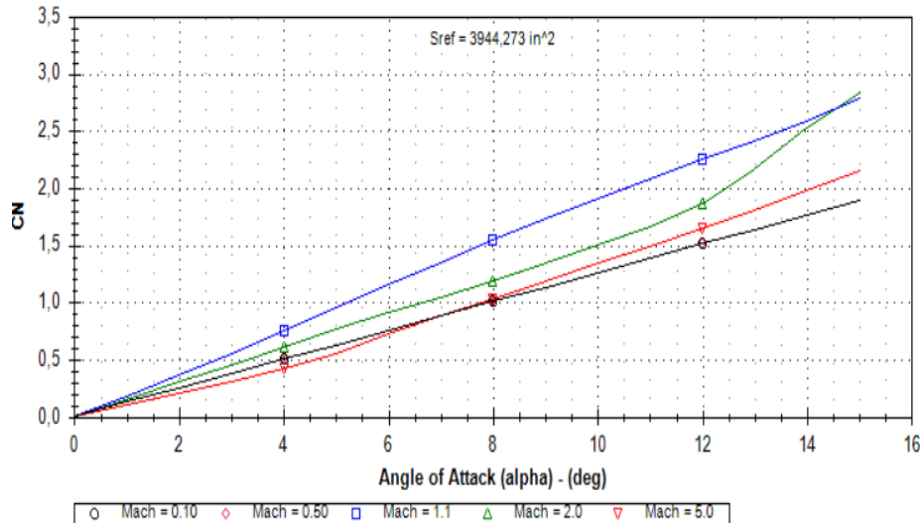


Figure A.7: Ras Aero 2 aeroplot for  $C_{n_{tot}}$

For what concern high supersonic behavior up to  $10^\circ$  there are no substantial difference between computed  $C_n$  and the curves from *Ras Aero 2*, while differences in slow Supersonic and Subsonic condition can be found and this could be addressed to different model which this software exploit to derive the already mentioned parameter.

### A.7.2 Ca model

Regarding the  $Ca$ , a similar approach to the one adopted for the  $C_n$  has been followed, the contributions of the body and aerodynamic appendixes have been modeled separately and then merged according to components Build-up theory. The main difference with previous analysis is that in this case the coefficients have been computed at zero-Lift condition ( $\alpha = 0$ ) and then the global coefficient evaluated at the AoA of interest through:

$$Ca = Ca_0 \cos^2(\alpha) \quad (\text{A.12})$$

#### $Ca_0$ body

Evaluating the contribution of the body, three different terms have been taken into account:

- **Wave Drag:** The drag due to the shock wave has been modeled both in subsonic and supersonic region, the choice of taking into account also the behavior at  $M < 1$  has been driven by the fact that the Viper-1 is released by the carrier at  $M = 0.8$  so same effects due to compressibility of air are already present at least for the nose. Initially designed as a Tangent Ogive, in order to accomplish thermal requirements the nose has been blunted. The aerodynamic model takes into account this change in shape considering the contribution of a hemispherical nose and summing it to the contribute of the sharp one weighting them through suitable Surfaces ratios. At the end, in supersonic region the contribution of the wave drags on the shoulder it has been assumed not negligible. So this contribution has been modeled as follows:

- Subsonic Region [16]:  $M \leq 1$

$$Ca_{0_{hemi}} = 0.665 \left( 1.59 + \frac{1.83}{M^2} \right) \quad (\text{A.13})$$

$$\varphi = \tan^{-1} \left( \frac{1}{2f n_{nose}} \right) \quad (\text{A.14})$$

$$Ca_{0_{sharp}} = 0.8 \sin(\varphi)^2 \quad (\text{A.15})$$

$$Ca_{0_{blunt}} = Ca_{0_{sharp}} \left( \frac{S_{nose} - S_{tip}}{S_{nose}} \right) + Ca_{0_{hemi}} \left( \frac{S_{tip}}{S_{nose}} \right) \quad (\text{A.16})$$

- Supersonic Region:  $M > 1$  Here the effect of the actual wave drag has been considered according to the empirical Miles Method [34]

$$\sigma = 2\text{atan}\left(\frac{d_{nose}}{2l_{nose}}\right)\left(\frac{180}{\pi}\right) \quad (\text{A.17})$$

$$P = \left(0.083 + \frac{0.096}{M^2}\right) \left(\frac{\sigma}{10}\right)^{1.69} \quad (\text{A.18})$$

$$Ca_{0_{sharp}} = P \left(1 - \frac{|196fn_{nose} - 16|}{14(M+18)fn_{nose}^2}\right) \quad (\text{A.19})$$

Then Equation A.16 is used to compute  $Ca_{0_{blunt}}$  in this region. For what concern the shoulder  $Ca_{0_{shoulder}}$  has been computed through Equation A.17, Equation A.18 and Equation A.19 replacing the geometrical parameter of the shoulder, ending with:

$$Ca_{0_{wave}} = Ca_{0_{blunt}} + Ca_{0_{shoulder}} \quad (\text{A.20})$$

- **Base Drag:** The base drag is a pressure-based contribution and depends on the interaction between the flow and the nozzle section of the launcher. Also, this kind of drag varies its behaviour in Sub and Super sonic condition. Moreover, this contribution is also influenced by the condition of the thruster, indeed if ignited this effect is less effective on the total D.

- Unpowered

- \* Subsonic Condition:  $M < 1$

$$Ca_{base} = 0.12 + 0.13M^2 \quad (\text{A.21})$$

- \* Supersonic Condition:  $M \geq 1$

In this case, the Gabeaud formulation has been adopted

$$Cp_{base} = \left(\frac{2}{\gamma_{air}M^2}\right) \left(\left(\frac{2}{\gamma_{air}+1}\right)^{1.4} \left(\frac{1}{M}\right)^{2.8} \left(\frac{2\gamma_{air}M^2 - \gamma_{air} + 1}{\gamma_{air} + 1}\right) - 1\right) \quad (\text{A.22})$$

$$Ca_{0_{base}} = -Cp_{base} \quad (\text{A.23})$$

- Powered

- \* Subsonic Condition:  $M < 1$

$$Ca_{0_{base}} = \left(1 - \left(\frac{d_{nozzle}^2}{d_{stage1}^2}\right)\right) (0.12 + 0.13M^2) \quad (\text{A.24})$$

- \* Supersonic Condition:  $M \geq 1$

$$Ca_{0_{base}} = \left(1 - \left(\frac{d_{nozzle}^2}{d_{stage1}^2}\right)\right) \left(\frac{0.25}{M}\right) \quad (\text{A.25})$$

- **Skin Friction:** Thought to be the least affective source of drag, it has been modeled taking into account the interaction of the flow in different states, from laminar to high turbulent based on the local Reynolds Number, with the superficial roughness heights of the wet surface of the launcher [35]. In this model an optimum paint surface with an  $Rs = 5 * 10^{-6}$  has been considered.

Type of surface	Height / $\mu\text{m}$
Average glass	0.1
Finished and polished surface	0.5
Optimum paint-sprayed surface	5
Planed wooden boards	15
Paint in aircraft mass production	20
Smooth cement surface	50
Dip-galvanized metal surface	150
Incorrectly sprayed aircraft paint	200
Raw wooden boards	500
Average concrete surface	1000

Figure A.8: superficial roughness heights [35]

Then according to this value a critical  $Re$  can be computed:

$$Re_{crit} = 51 \left( \frac{R_s}{l} \right)^{-1.039} \quad (\text{A.26})$$

Then this value is used as reference for different flow condition as follow

- Low turbulent flow:  $Re \leq 10^4$

$$Cf = 1.48 * 10^{-2} \quad (\text{A.27})$$

- Turbulent Flow  $Re > 10^4$  and  $Re < Re_{crit}$

$$Cf = \frac{1}{(1.5 \log(\text{Re}) - 5.6)^2} \quad (\text{A.28})$$

- Extremely turbulent  $Re \geq Re_{crit}$  In this situation there is no more dependence on the local Reynolds.

$$Cf = 0.032 \left( \frac{R_s}{l} \right)^{0.2} \quad (\text{A.29})$$

Then a correction due to compressibility effect is taken into account

- Subsonic flow  $M < 1$ :

$$Cf_c = Cf(1 - 0.1M^2) \quad (\text{A.30})$$

- Supersonic flow  $M \geq 1$ : In this case two correction have been taken into account and among the two the higher value selected

$$Cf_c = \frac{Cf}{(1 + 0.15M^2)^{0.58}} \quad (\text{A.31})$$

$$Cf_c = \frac{Cf}{1 + 0.18M^2} \quad (\text{A.32})$$

Then once the corrected skin friction coefficient has been computed it can be turned into the actual  $Ca_{0,skin}$  as follow:

$$Ca_{0,skin} = Cf_c \left( \frac{1 + \frac{1}{2fn_{body}}}{S_{wetbody}} \right) S_{ref} \quad (\text{A.33})$$

Where the  $S_{wetbody}$  is the lateral surface of the cylinder exposed at the flow.



The body contribution at zero-lift condition is:

$$Ca_{0_{body}} = Ca_{0_{base}} + Ca_{0_{skin}} + Ca_{0_{wave}} \quad (\text{A.34})$$

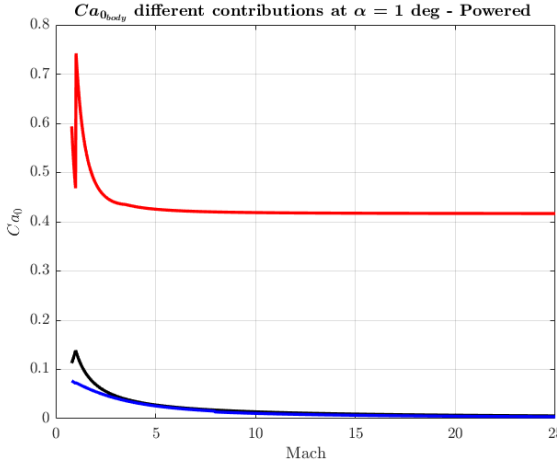


Figure A.9:  $Ca_{0_{body}}$  contributions-powered case

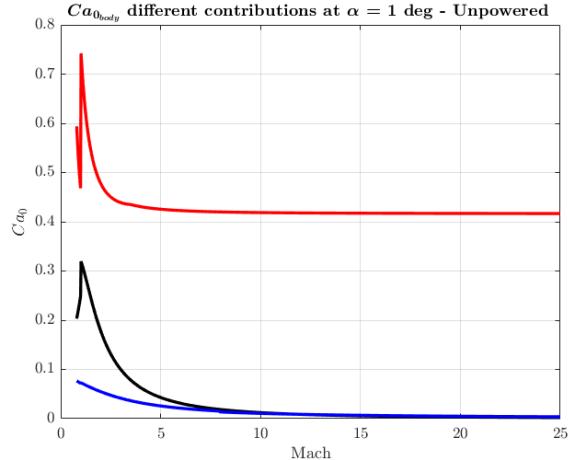


Figure A.10:  $Ca_{0_{body}}$  contributions-unpowered case

As can be seen in A.9 and A.10 the assumption on low skin friction is confirmed, it is also evident the difference in the effect of Base Drag in the two different cases. This is due to the fact that Base drag is a consequence of the recirculation effect caused by the negative pressure zone on the base surface, when ignited, the high pressure zone due to the plume sensibly reduces the Area exposed at recirculation. The most effective contribution is, as expected, the one due to the wave drag which is accentuated by the bluntness of the nose.

### $Ca_0$ Fins and Tail

According to the chosen shape, the forward and tail fins have been sized by considering as reference [16]. These models are based on the modified Newtonian Theory:

$$Ca_{0_{Surface,Friction}} = n_{Surface} \left( 0.0133 \left[ \frac{M}{qc_{mac}} \right]^{0.2} \right) \left( \frac{2S_{Surface}}{S_{ref}} \right) \quad (\text{A.35})$$

$$Ca_{0_{Surface,Wave}} = n_{Surface} \left( \frac{1.429}{M_{LE}^2} \right) \left[ (1.2M_{LE}^2)^{3.5} \left[ \frac{2.4}{2.8M_{LE}^2 - 0.4} \right]^{2.5} - 1 \right] \sin^2(\delta_{LE}) \cos(\Lambda_{LE}) t_{mac} \frac{b}{S_{ref}} \quad (\text{A.36})$$

### Plot fins and tail contribution

In these empirical equations the units of dynamic pressure  $q$  and mean aerodynamic chord  $C_{mac}$  are  $psf$  and  $ft$  respectively as displayed in [16]. The cumulative contribution of the aerodynamic appendices is:

$$Ca_{0_{surf}} = Ca_{0_{Surface,Wave}} + Ca_{0_{Surface,Friction}} \quad (\text{A.37})$$

Additionally, thanks to this model, the variation of the  $C_p$  due to the Mach has been evaluated and taken into account for the further computation of the Aerodynamic moments when needed. Finally, once all the components have been evaluated, accordingly with the components Build-Up theory the global axial coefficient at zero-lift condition is

$$Ca_0 = Ca_{0_{surf}} + Ca_{0_{body}} \quad (\text{A.38})$$

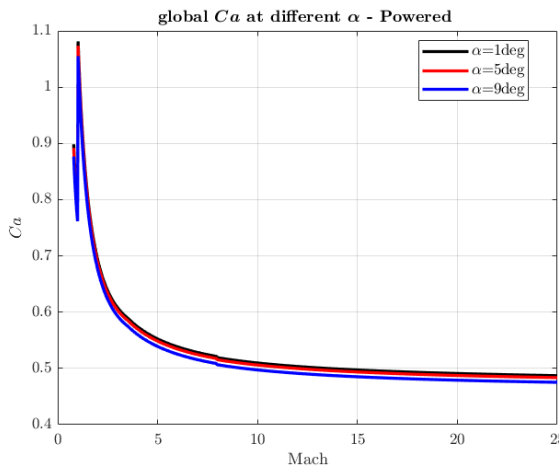


Figure A.11:  $Ca$  - powered case

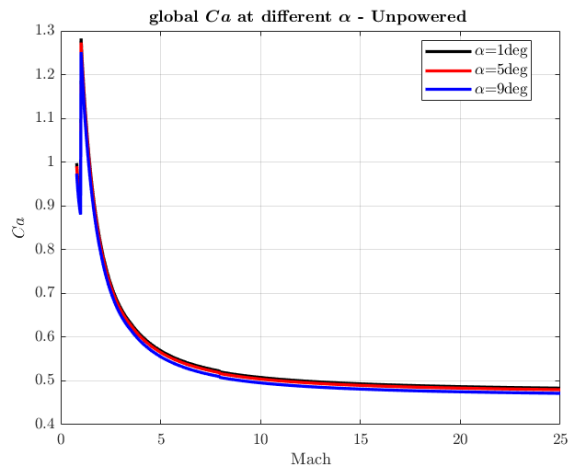


Figure A.12:  $Ca$  -unpowered case

What is shown in A.11 and A.12 is consistent with what was expected, it is valuable to highlight the peaks at  $M=1$  which are caused by a higher contribution of the wave drag due to the presence of the already cited bluntness: Equation A.16. Validation of the model adopted in this case has been more challenging with respect to the  $Cn$  one. Indeed, the software used as validation tool, *Ras Aero 2*, adopts different computational method for the estimation of  $Ca$  coefficient. Main problems are due to the different approach adopted in the computation of  $Ca_{body}$ , in figure A.13 is shown the Aeroplot from the mentioned software:

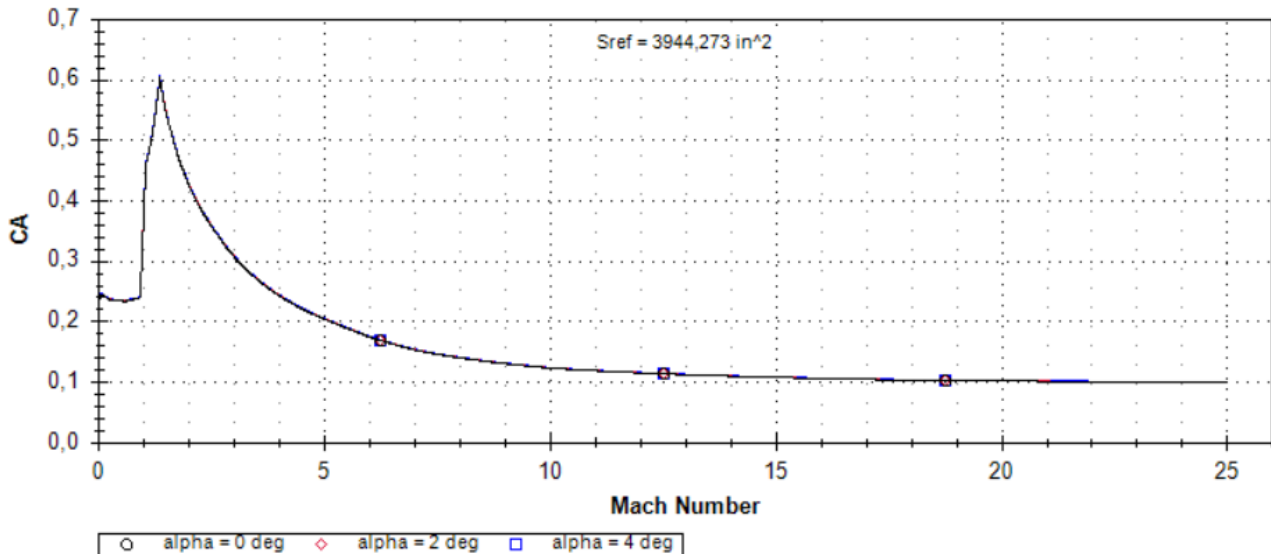


Figure A.13:  $Ca$  from *Ras Aero 2*

Comparing the plots some discrepancies can be found and they can be accounted, for instance in fig A.13 peak at  $M=1$  is sensibly lower to the one in fig A.12 this is mainly due to the presence of the blunted contribution that *Ras Aero 2* does not take into account, proof of this statement is the behavior of the model when a non-blunted nose is used A.14 . For what concern the behavior at high Mach values the discrepancies should be addressed to the way the skin friction has been modeled. Anyway, the global behavior of the curves is almost the same allowing, with a certain degree of certainty, that the model developed for the computation of the  $Ca$  is working properly.

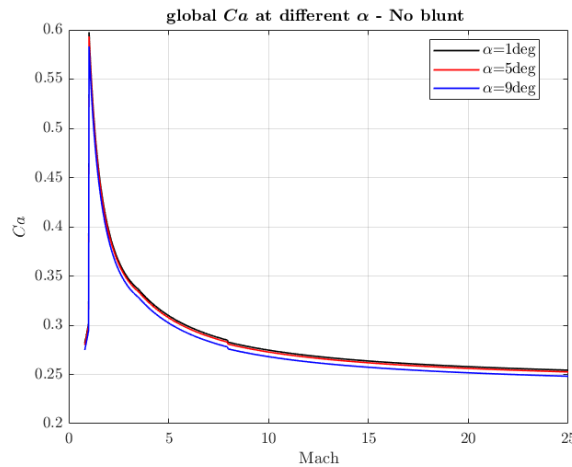


Figure A.14:  $Ca$  without blunted nose

## A.8 Deflection angle fin $\delta_{fin}$

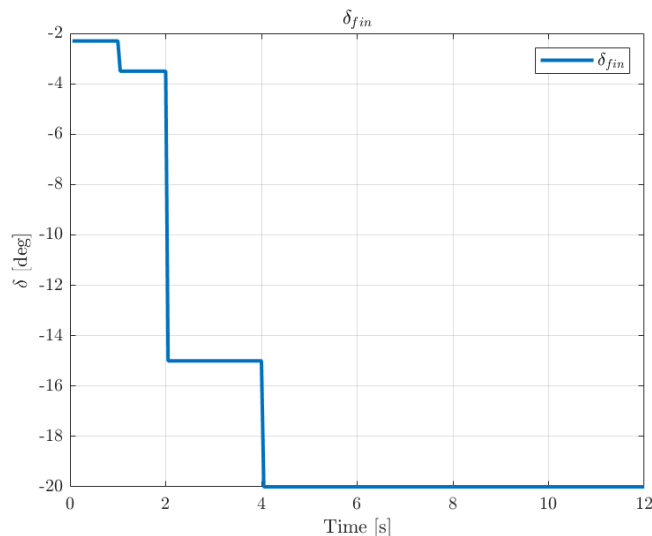


Figure A.15: Deflection angle fin

This plot shows how forward fins were used. As it can be seen, all the angles are negative due to the fact that they are mainly used in the first part of the flight, just after the dropping, with the aim to create down-force and slow down the angular acceleration.

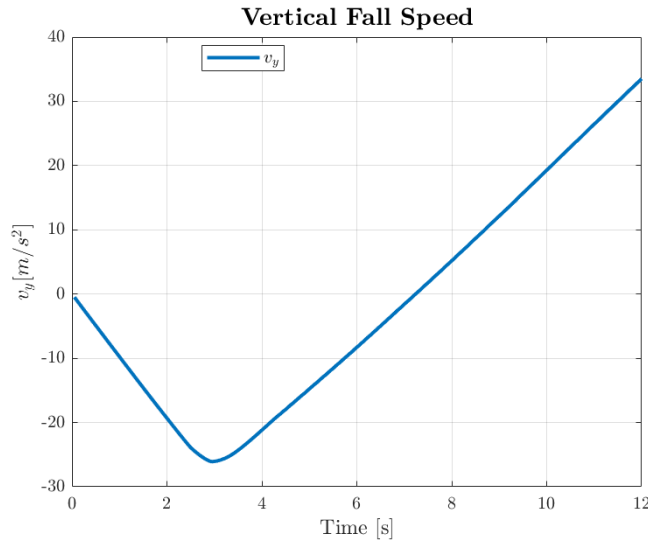


Figure A.16: Vertical Fall Speed

This plot shows what is the reason behind the "premature" switch-on of the thrust: as it is clear, even if the ignition is at  $2.5s$ , the rocket doesn't start to climb till around  $7s$ , where the vertical speed is null; for this reason, there aren't risks for the aircraft and it is not required to take evasive maneuvers.

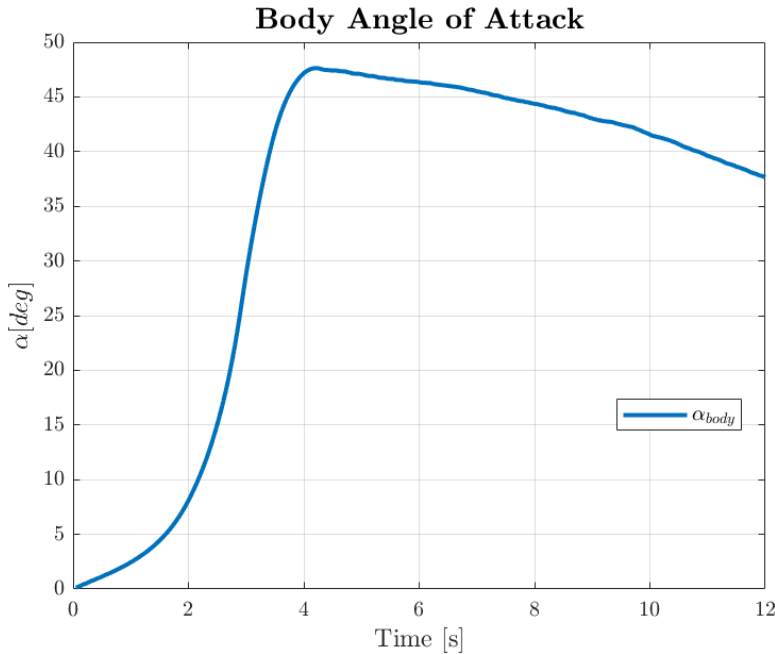


Figure A.17: Body Angle of Attack

This plot shows how the transient phase is different from the typical values of the body angle of attack. This is due to a double inclination: the first given by the starting rotation of the rocket and the second given by the falling (so the  $\gamma$  angle is increasing negatively). This value provide a drift of the rocket once the tail is completely deployed.

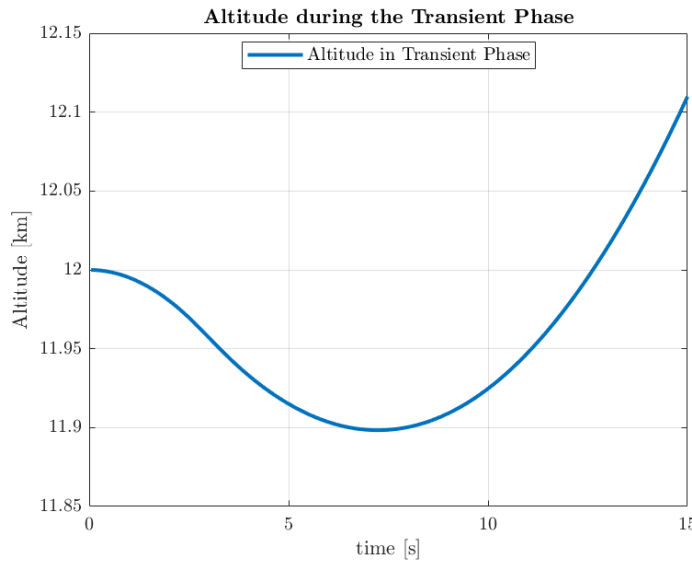


Figure A.18: Altitude during Transient

As mentioned, the rocket can recover its negative vertical velocity around 100m of altitude, showing the progressive and continuous climbing towards the initial conditions of the nominal trajectory.

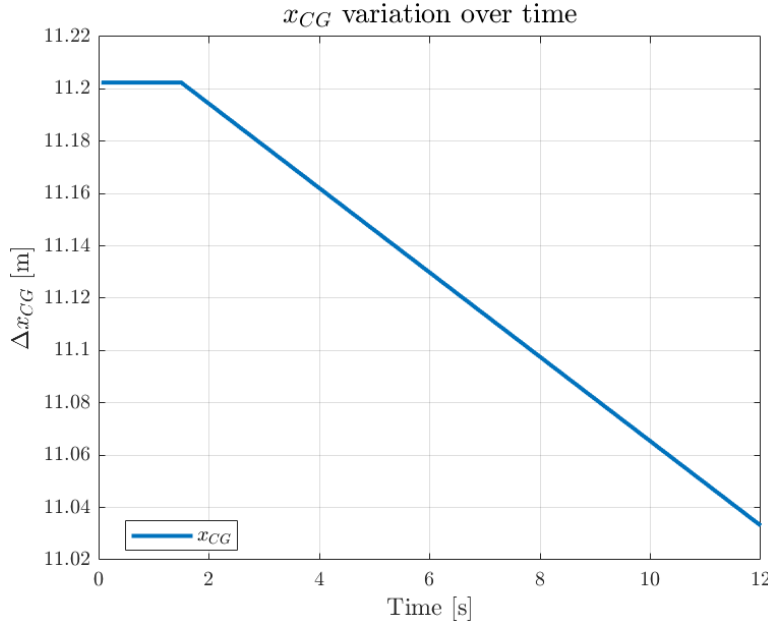


Figure A.19:  $x_g$  variation

In this plot is shown the interpolation done for the  $C_g$  variation due to the consumption of the propellant (the same was done for the inertia).

## A.9 $\alpha_{wind}$ disturbance model

In order to evaluate the stability a disturbance due to wind shears impacting on the launcher a model based on the wind shear velocity has been developed, based on the statistical value present in the [36].



$v_{wind} = (6.9288h_{km} + 9.144) \text{ m/s}$	$0 < h \leq 9.6 \text{ km}$
$v_{wind} = 76.2 \text{ m/s (250 ft/s)}$	$9.6 \text{ km} < h \leq 14 \text{ km}$
$v_{wind} = [76.2 - 8.9474(h_{km} - 14)] \text{ m/s}$	$14 \text{ km} < h \leq 20 \text{ km}$
$v_{wind} = 24.384 \text{ m/s (80 ft/s)}$	$h > 20 \text{ km}$

Table A.1: wind shear velocity  $v$  with respect different heights ranges  $h$ .

Starting from this velocity the  $\alpha_{wind}$  and the real local AoA are retrieved as follow:

$$v_{x_{body}} = v_{body} \cos(\gamma) \quad (\text{A.39})$$

$$v_{y_{body}} = v_{body} \sin(\gamma) \quad (\text{A.40})$$

$$V_{real} = \sqrt{v_{y_{body}}^2 + (v_{x_{body}} - v_{wind})^2} \quad (\text{A.41})$$

$$\alpha_{wind} = \arccos\left(\frac{v_{wind}^2 - v_{x_{body}}^2 - V_{real}^2}{-2v_{x_{body}}V_{real}}\right) \quad (\text{A.42})$$

$$\alpha_{local} = \alpha_{wind} + \alpha_{body} \quad (\text{A.43})$$

## A.10 Trajectory

The EOM used for the trajectory design are reported below:

$$\begin{cases} \dot{V} = \frac{T}{M} \cos \delta - \frac{D}{M} - g \sin \gamma \\ \dot{\gamma} = \frac{V \cos \gamma}{R} + \frac{T \sin \delta}{MV} + \frac{L}{MV} - \frac{g \cos \gamma}{V} \\ \dot{h} = V \sin \gamma \\ \dot{\omega} = \frac{\dot{x}}{R} = \frac{V \cos \gamma}{R} \\ g = \frac{g_0}{(1 + \frac{h}{R_E})^2} \end{cases}$$

## A.11 Thrust Vector Control

Feature	Concept Weight	1	2	3	4	5
Maximum deflection	5	5	3	3	2	4
Rate of deflection	4	4	3	2	5	3
Heritage	1	2	5	3	2	2
Mass	4	2	5	2	3	5
Occupied Volume	3	2	5	1	2	5
Complexity	2	3	4	2	2	4
Reliability	3	4	3	3	3	3
Total:		75	84	50	63	86

Figure A.20: Pugh matrix



### A.11.1 Control

3DOF model is used to ensure that the vehicle follows its nominal trajectory.

$$\ddot{\theta} = \frac{T \sin(\delta) (L - x_{C_g})}{I_{yy}} + \frac{N (x_{C_g} - x_{C_p})}{I_{yy}} \quad (\text{A.44})$$

The model incorporates the gimbal angle control for the TVC, which is computed using a simple feedback control system based on the pitch rate and the error between the flight path angle and the pitch angle.

$$\delta = K_1(\gamma - \theta) + K_2\dot{\theta} \quad (\text{A.45})$$

where the gains  $K_1$  and  $K_2$  are respectively 2 and 0.8. The control law aims to keep  $\theta$  as close as possible to the flight path angle of the nominal trajectory.

### A.11.2 Reference systems

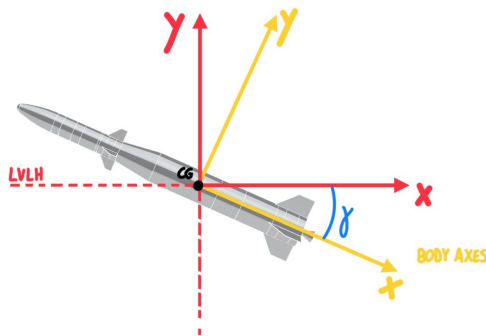


Figure A.21: Sistemi di riferimento

All the study was based on these two simple reference systems: LVLH and body axes. In the transient phase a third one can be added due to the presence of  $\delta_{fin}$  angle which link the reasoning around this angle.

## A.12 Convective heat transfer model

The following equations have been used for the convective heat transfer model:

$$\dot{q}_{\text{conv}} = C \rho^N V^M \quad C = (1.83 \cdot 10^{-4}) \frac{1}{\sqrt{r_n}} (1 - g_w) \quad (\text{A.46})$$

where  $\dot{q}_{\text{conv}}$  is the heat flux in  $\text{W/m}^2$ , the constant  $C$  [37] depends on the nose cone tip radius  $r_n$  (in meters), and  $g_w$  represents the ratio of wall enthalpy to total enthalpy. A correction factor accounts for the presence of the boundary layer, which in the worst case is zero, so for the purpose of sizing, it was assumed to be zero. The variable  $\rho$  denotes the free-stream air density (in  $\text{kg/m}^3$ ) at the flight altitude, and  $V$  represents the free-stream airspeed (in m/s). This is a first-order model which may not be highly accurate. It is difficult to assess whether this model overestimates or underestimates the actual heat load, so some form of validation would be highly beneficial. Additionally, this model lacks a reliable method to estimate the heat transfer along the surface of the nose cone, away from the stagnation point.



## A.13 Thermal analysis FDM Method

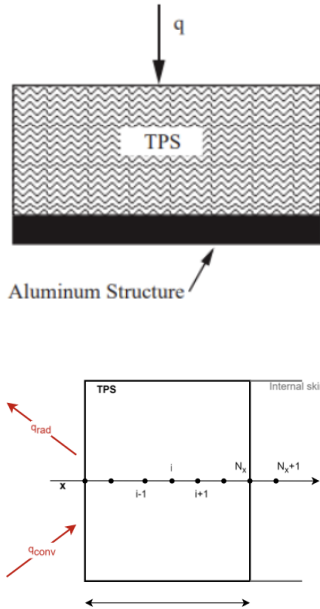
Specifically, a 1D model has been considered, as shown in Figure A.22, where the wall is insulated from the external environment with a material thickness  $t$ . The following assumptions have been made:

- No internal heat generation.
- No variations along the  $y$ -direction; temperature varies only in the  $x$ -direction.
- Adiabatic inner surface: the temperature at the rear of the Thermal Protection System (TPS) is assumed to be the same as that of the base material.
- Thermal properties are assumed to be constant, even as temperature changes.
- Only the convective component of the incident flux is considered.
- Heat from possible chemical reactions in the flow around the vehicle is neglected.

Finite difference discretization was used, dividing the thickness  $t$  of the Thermal Protection System (TPS) into  $N_x$  nodes, as shown in Figure A.22, where  $N_x$  is the number of nodes along the spatial coordinate  $x$ . Let  $i$  represent the node index along the thickness  $t$ , with  $1 \leq i \leq N_x$ . The node at the external surface is denoted by  $i = 1$ , corresponding to  $x = 0$ . For the temperature calculation, the balance between the convective heat flux from the outside and the radiative flux was considered. The governing equation is:

$$\rho c_p \frac{\partial T}{\partial t} = k \frac{\partial^2 T}{\partial x^2}, \quad (\text{A.47})$$

where  $\rho$  is the density of the Thermal Protection System (TPS) material,  $c_p$  is the specific heat capacity (in  $\text{J}/(\text{kg} \cdot \text{K})$ ), and  $k$  is the thermal conductivity (in  $\text{W}/(\text{m} \cdot \text{K})$ ). To implement the finite difference method, a centred difference formula was used for approximating the second spatial derivative [38].



$$\frac{\partial^2 T}{\partial x^2} = \frac{T_{i+1} - 2T_i + T_{i-1}}{\Delta x^2} \quad (\text{A.48})$$

Here,  $i$  is an index ranging from 2 to  $N_x - 1$ . An explicit finite difference method was used to approximate the time derivative. The partial derivative of temperature with respect to time is discretized using a forward finite difference scheme. Let  $T_i^n$  denote the temperature at spatial point  $i$  and time step  $n$ , so:

$$\frac{\partial T}{\partial t} = \frac{T_i^{n+1} - T_i^n}{\Delta t} \quad (\text{A.49})$$

By substituting the expressions of the derivatives in space and time into Eq.A.47, we obtain the following equation:

$$\frac{T_i^{n+1} - T_i^n}{\Delta t} = \alpha \frac{\partial^2 T}{\partial x^2} = \alpha \frac{T_{i+1} - 2T_i + T_{i-1}}{\Delta x^2} \quad (\text{A.50})$$

Figure A.22: FD thermal model of TPS [21]

Solving for  $T_i^{n+1}$ , we have:

$$T_i^{n+1} = T_i^n + \alpha \frac{\Delta t}{\Delta x^2} (T_{i+1}^n - 2T_i^n + T_{i-1}^n), \quad (\text{A.51})$$

where  $\alpha = \frac{k}{\rho c_p}$  is the thermal diffusion coefficient (in  $\text{m}^2/\text{s}$ ). This equation is valid for internal nodes. The main challenge with the Forward Time Centered Space (FTCS) scheme is ensuring solver stability [39]. For the heat equation, a stability analysis shows that the time step ( $\Delta t$ ) and spatial step ( $\Delta x$ ) must satisfy the following condition:

$$r = \frac{\alpha \Delta t}{\Delta x^2} < \frac{1}{2} \quad (\text{A.52})$$

In the numerical scheme implemented, the spatial resolution is predefined, and the software computes a suitably small time step to maintain stability. While reducing the time step and spatial step improves accuracy by reducing numerical error, it significantly increases computational time.

To solve the problem, appropriate boundary conditions must first be chosen.

**Boundary Condition - Outer Surface** ( $x = 0$ ) The boundary condition at the outer surface accounts for the balance of heat fluxes, including the incoming convective heat flux, the outgoing radiative heat flux, and the conductive heat exchanged between adjacent cells:

$$k \frac{T(2,n) - T(1,n)}{\Delta x} - \varepsilon \sigma (T(1,n)^4 - T_{amb}^4) + q_{conv} = \rho c_p \frac{\Delta x}{2} \frac{T(1,n+1) - T(1,n)}{\Delta t} \quad (\text{A.53})$$

Solving for the temperature  $T(1,n+1)$ , the boundary condition at the external surface is given by:

$$T(1,n+1) = T(1,n) + \frac{2\Delta t}{\rho c_p \Delta x} \left( \dot{q}_{conv} + k \frac{T(2,n) - T(1,n)}{\Delta x} - \varepsilon \sigma (T(1,n)^4 - T_{amb}^4) \right) \quad (\text{A.54})$$

**Boundary Condition - Inner Surface** ( $x = t$ ) The boundary condition at the inner surface can be obtained by substituting  $i = N_x$ :

$$T(N_x, n+1) = \frac{\alpha \Delta t}{\Delta x^2} [T(N_x - 1, n) - 2T(N_x, n) + T(N_x + 1, n)] + T(N_x, n) \quad (\text{A.55})$$

The temperature  $T_{N_x+1}$  corresponds to the temperature at the node on the internal skin of the vehicle, which is considered an adiabatic wall. Therefore:

$$T(N_x, n) = T(N_x + 1, n) \quad (\text{A.56})$$

So, the boundary condition at the inner surface is:

$$T(N_x, n+1) = \frac{\alpha \Delta t}{\Delta x^2} [T(N_x - 1, n) - T(N_x, n)] + T(N_x, n) \quad (\text{A.57})$$



## A.14 Re-entry

TYPE	CONSTRUCTED SHAPE		INFLATED SHAPE $\frac{D_p}{D_o}$	DRAG COEF $C_D$ RANGE	OPENING FORCE COEF $C_X$ (INF MASS)	AVERAGE ANGLE OF OSCILLATION, DEGREES	GENERAL APPLICATION
	PLAN	PROFILE					
FLAT CIRCULAR		— —	1.00	0.67 TO 0.70	0.75 TO 0.80	~1.7	±10 TO ±40
CONICAL		— —	0.93 TO 0.95	0.70	0.75 TO 0.90	~1.8	±10 TO ±30
BICONICAL		— —	0.90 TO 0.95	0.70	0.75 TO 0.92	~1.8	±10 TO ±30
TRICONICAL POLYCONICAL		— —	0.90 TO 0.95	0.70	0.80 TO 0.96	~1.8	±10 TO ±20
EXTENDED SKIRT 10% FLAT		— —	0.86	0.66 TO 0.70	0.78 TO 0.87	~1.4	±10 TO ±15
EXTENDED SKIRT 14.3% FULL		— —	0.81 TO 0.85	0.66 TO 0.70	0.75 TO 0.90	~1.4	±10 TO ±15
HEMISPERICAL		— —	0.71	0.66	0.62 TO 0.77	~1.6	±10 TO ±15
GUIDE SURFACE (RIBBED)		— —	0.63	0.62	0.28 TO 0.42	~1.2	0 TO ±2
GUIDE SURFACE (RIBLESS)		— —	0.66	0.63	0.30 TO 0.34	~1.4	0 TO ±3
ANNUAL		— —	1.04	0.94	0.85 TO 0.95	~1.4	< 6
CROSS		— —	1.15 TO 1.19	0.65 TO 0.72	0.60 TO 0.85	1.1 TO 1.2	0 TO ±3

Figure A.23: Parachutes geometry parameters

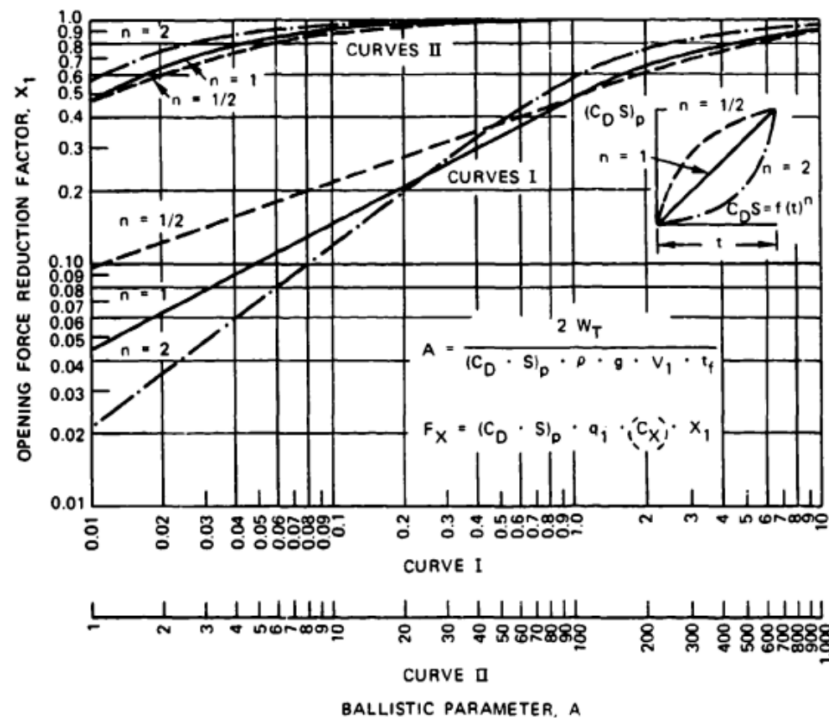


Figure A.24: Ballistic parameter vs Force reduction factor

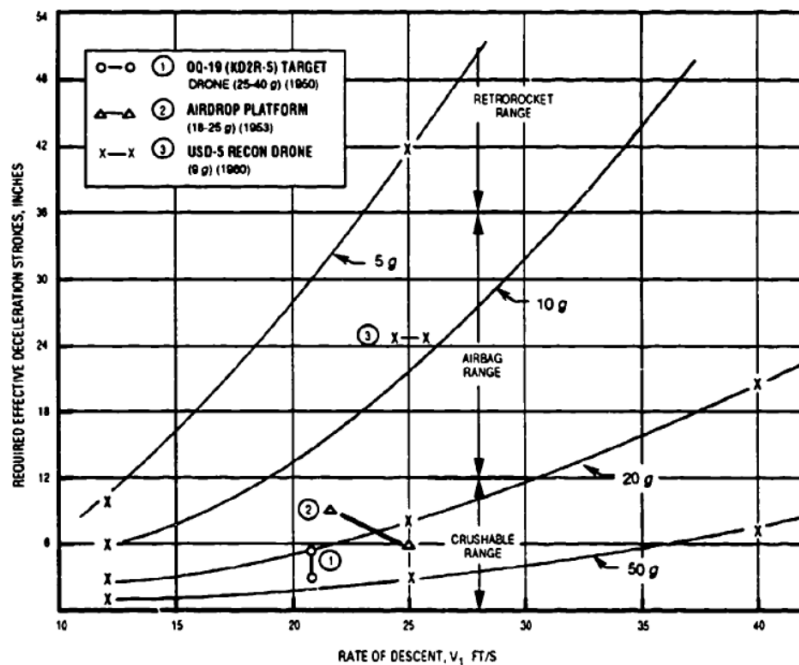


Figure A.25: Landing devices



Parachute type	Canopy fill constant, n		
	Reefed opening	Disreef opening	Unreefed opening
Solid flat circular	ID*	ID	8
Extended-skirt, 10%	16-18	4.5	10
Extended-skirt, full	16-18	7	12
Cross	ID	ID	11.7
Ribbon	10	6	14
Ringslot	ID	ID	14
Ringsail	7-8	2	7
Ribless guide surface	...	...	4-6

\* ID = Insufficient data available for meaningful evaluation.

Figure A.26: Canopy fill constant for various parachute types

Operation	Impact deceleration, g
Military airdrop cargo	20 to 35
Target drones, unmanned vehicle structures	20 to 30
Telemetry equipment	20 to 25
Sensitive electronics equipment	5 to 10
Aircrew members	6 to 10
Astronauts after long duration space flights	3 to 5

Figure A.27: Allowable impact decelerations

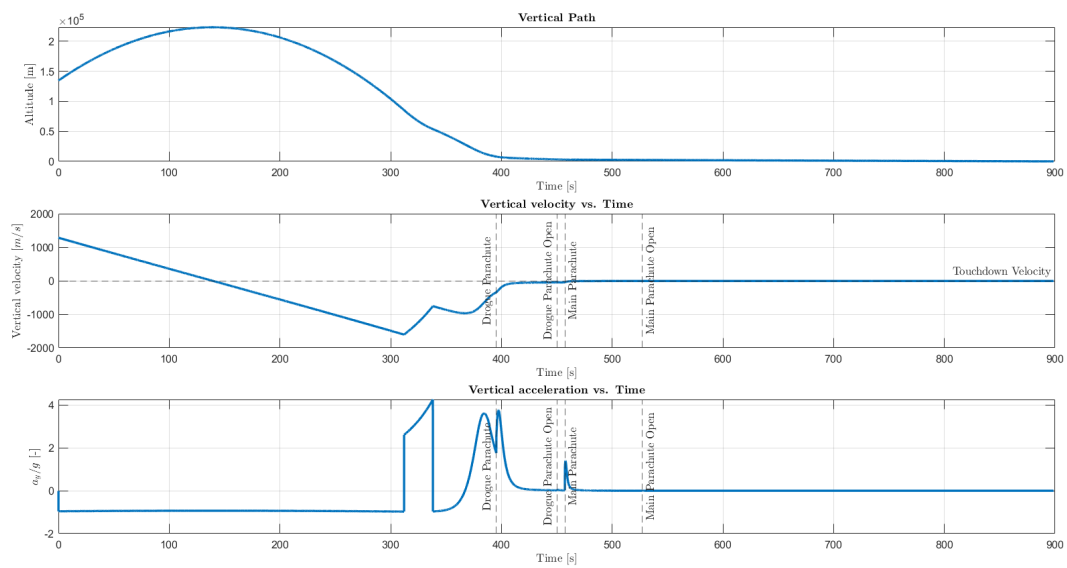


Figure A.28: First re-entry condition with main engine

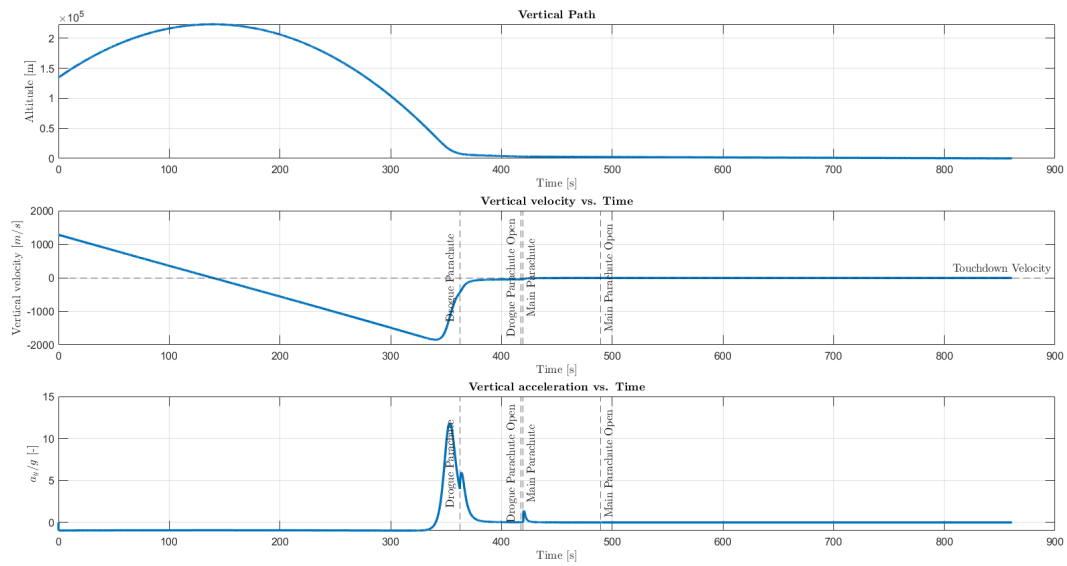


Figure A.29: First stage vertical re-entry condition without main engine

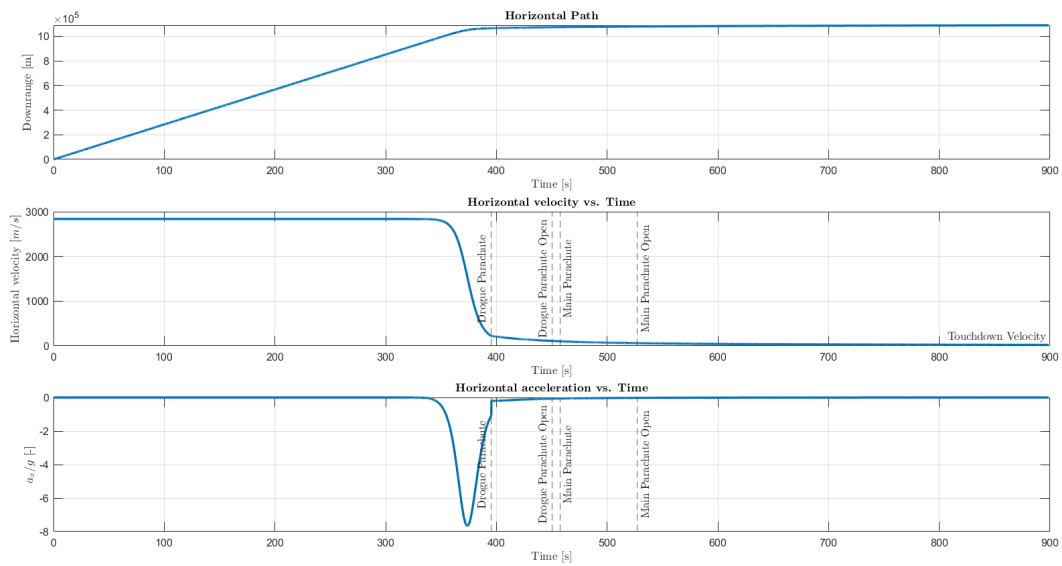


Figure A.30: First stage horizontal re-entry condition with main engine

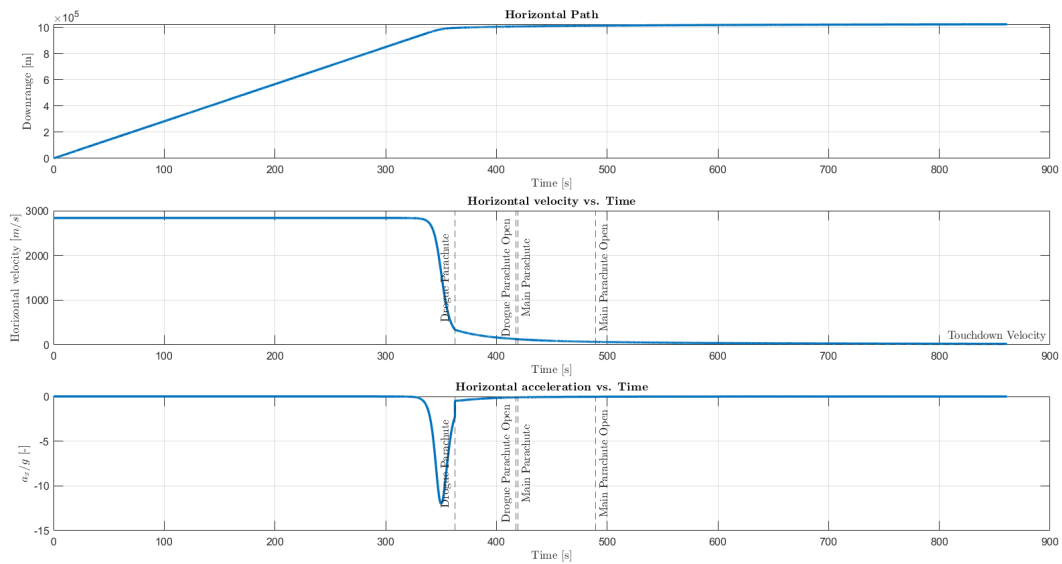


Figure A.31: First stage horizontal re-entry condition without main engine

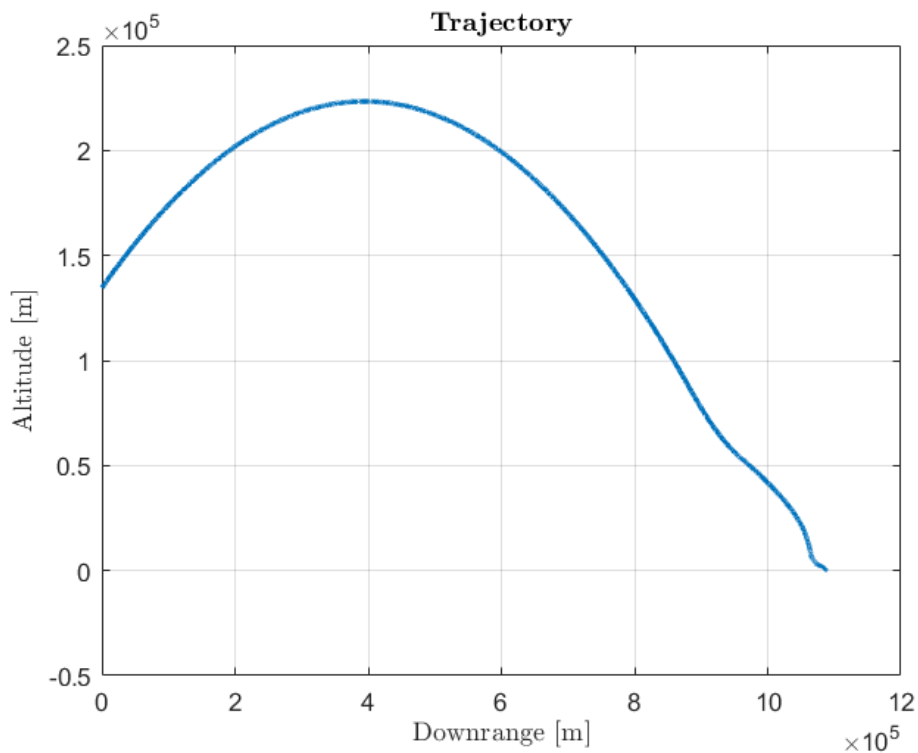


Figure A.32: First stage trajectory with main engine

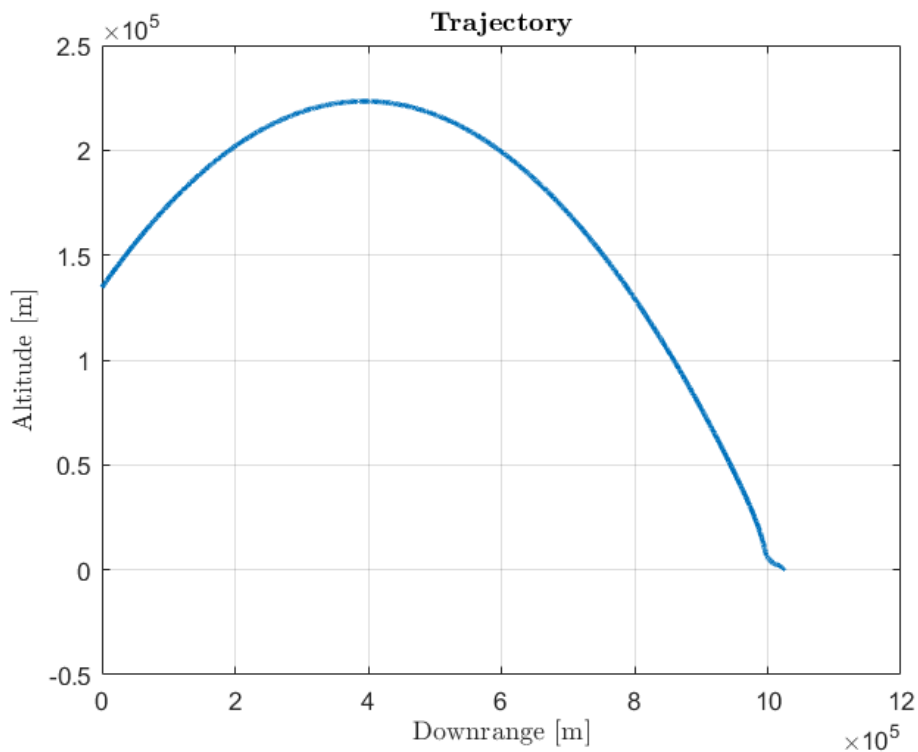


Figure A.33: First stage trajectory without main engine

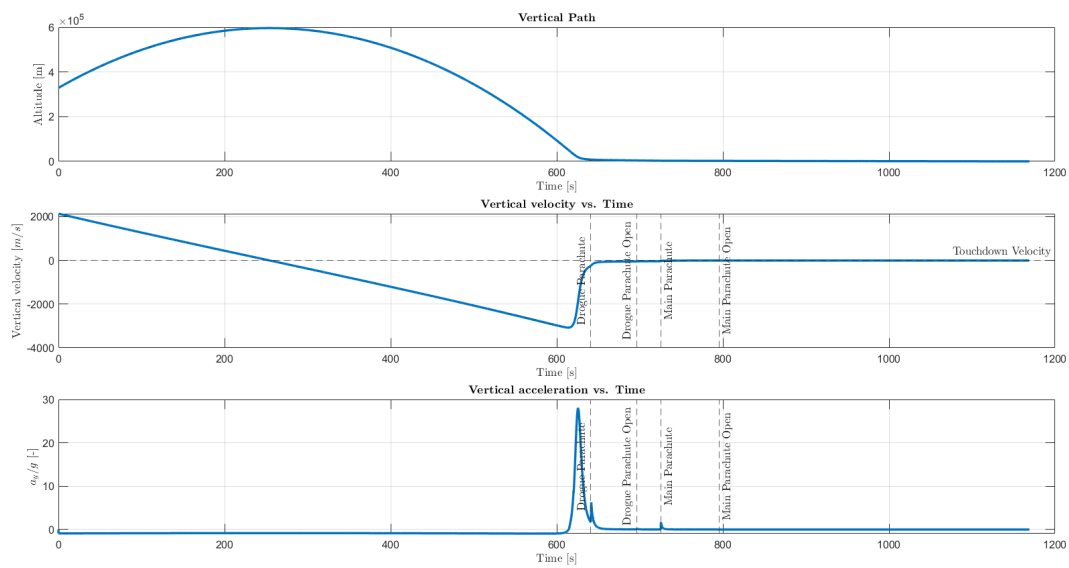


Figure A.34: Second stage re-entry condition with main engine

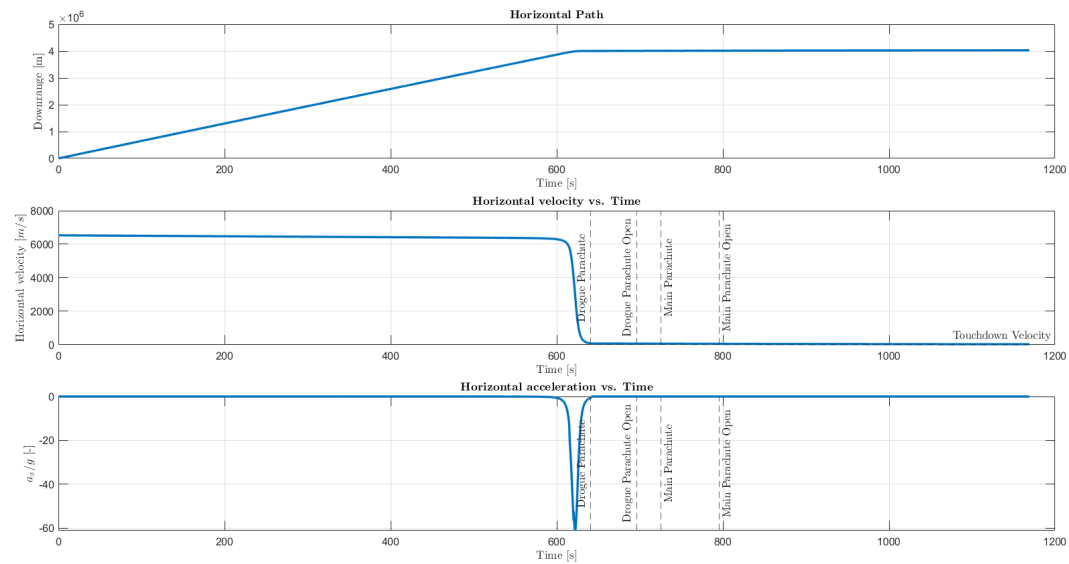


Figure A.35: Second stage horizontal re-entry condition

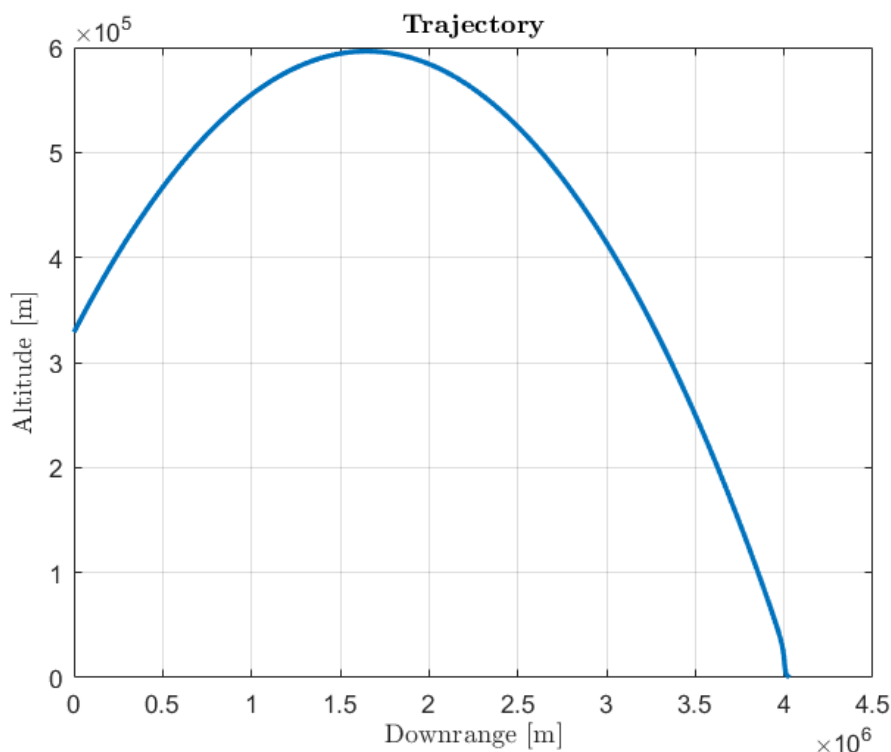


Figure A.36: Second stage trajectory



### A.14.1 Deorbiting

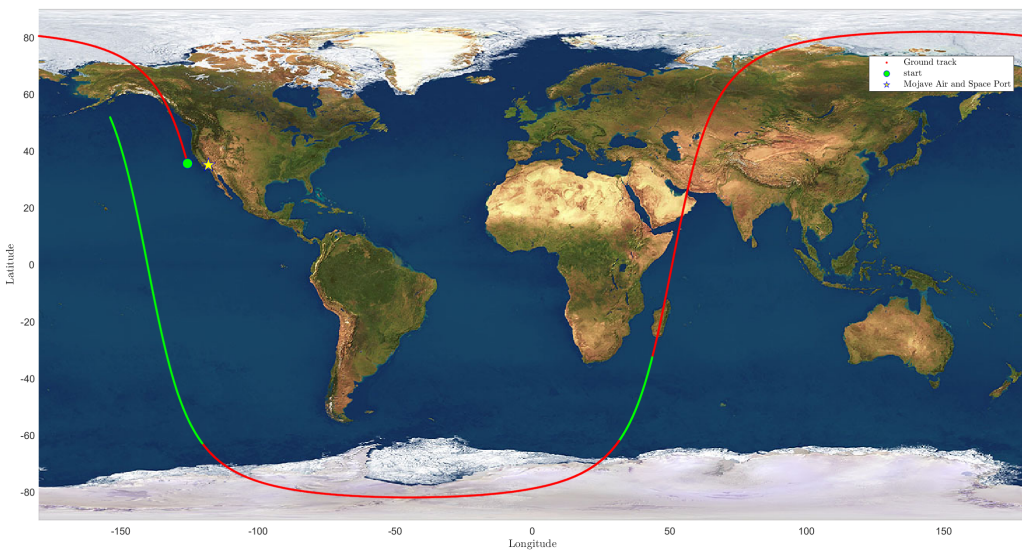


Figure A.37: Deorbiting II Stage

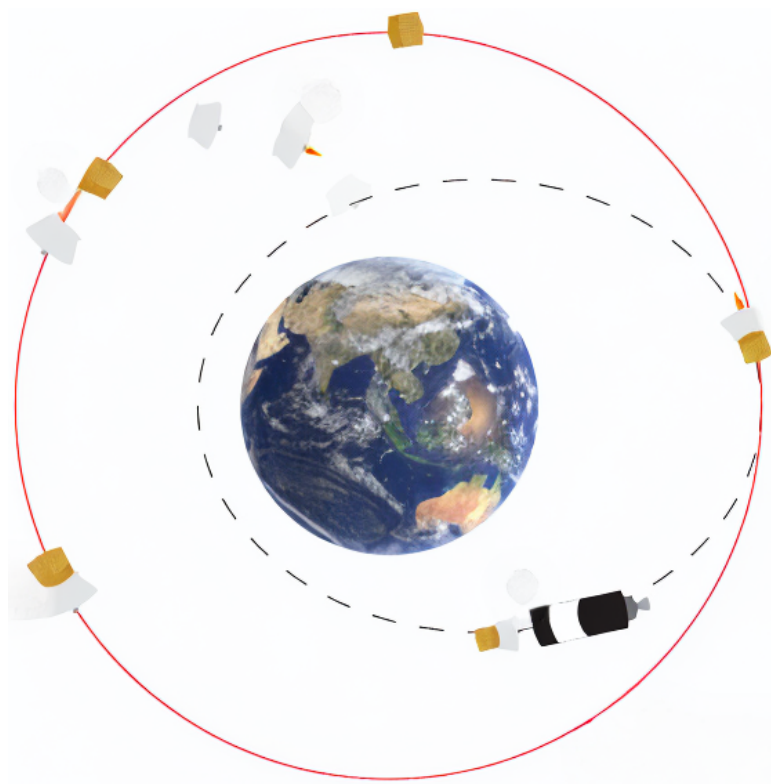


Figure A.38: Deorbiting Kick Stage



## A.15 Structure

### A.15.1 Pictures



Figure A.39: LauncherOne attachment to carrier

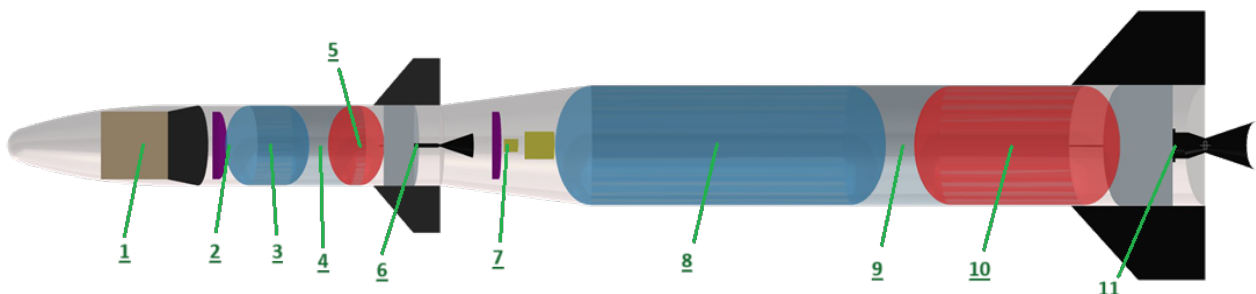


Figure A.40: Placement of nodes in the launcher

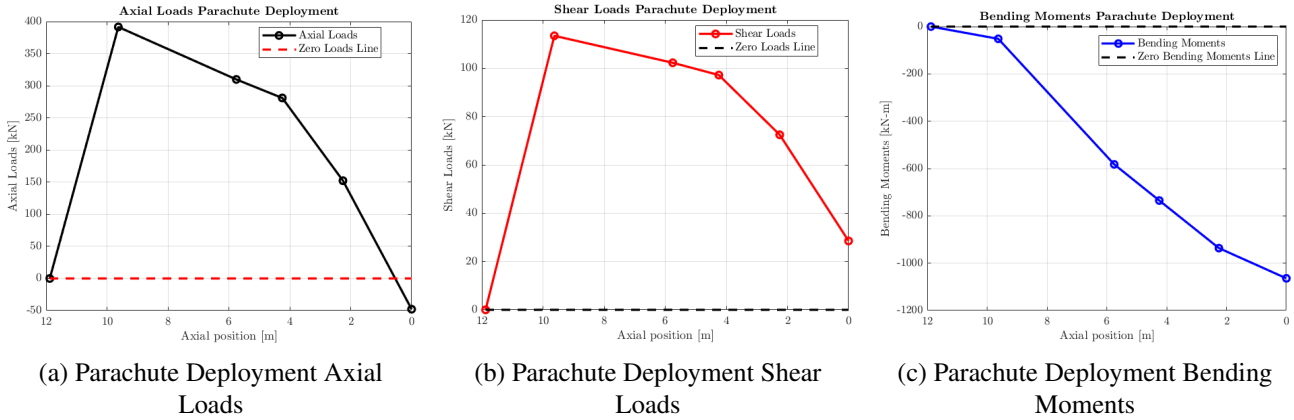


Figure A.41: Loads and Bending Moments analysis of Drouge Parachute Deployment

In the parachute deployment case it is worth noticing that the curves do not close due to the inertia of the masses present in the descending first stage.

### A.15.2 Equations

The estimation of the unknown masses of the components has been done following the equations, described in [40].

- **Metal unpressurized structures:** Interstage, Payload Fairing, Intertanks, After Skirt and Forward Skirt

$$m = 13.3 \frac{\text{kg}}{\text{m}^2} S_{ref}$$

- **Thrust structure mass:**

$$m = 2.55 \cdot 10^{-4} T$$

Where T is the Thrust expressed in N.

- **Avionics:** for a payload mass  $\leq 1000$  kg:

$$m = 75\text{kg}$$

To allocate for the 80% in the upper stage, and the remaining in the lower.

- **Wiring mass:**

$$m = 1.43L_0$$

Where  $L_0$  is the total length of the stage in analysis.

- **Tanks masses:**

$$m_{tank_{RP-1}} = 0.0148m_{RP-1}$$

$$m_{tank_{LOX}} = 0.0148m_{LOX}$$

$$m_{tank} = 12.16V_{prop}$$

The first two equations were compared to the latter one and at the same time evaluated with respect to a third MER [41]:

$$M_{LOX.tank} = (2.44 - 0.007702\rho_{LOX}) \cdot V_{LOX}^{(0.8548+0.0003189\rho_{LOX})} \quad (\text{A.58})$$

$$M_{RP-1.tank} = (2.44 - 0.007702\rho_{RP-1}) \cdot V_{RP-1}^{(0.8548+0.0003189\rho_{RP-1})} \quad (\text{A.59})$$

Where the propellant density  $\rho$  is expressed in  $\frac{\text{lb}}{\text{in}^3}$  and the propellant volume  $V$  is expressed in  $\text{in}^3$ . Therefore the mass will be evaluated in lb. An iterative process comparing different MERs refined the propellant tank thickness by applying these two estimation methods, validating initial calculations based on geometric and technical analyses.

- **Gimbals:**

$$m = 237.8 \left( \frac{T}{P_c} \right)^{0.9375} \quad (\text{A.60})$$

$T$  is the thrust of the engine expressed in  $N$  and  $P_c$  is the combustion chamber pressure in Pascal.

The stress evaluation has been carried out by considering the procedures and workflow depicted in [42]. Here are reported the equations considered during the computations:

- **Unpressurized case:**

$$\sigma_{axial} = \frac{P}{\pi r_i t_i} \quad (\text{A.61})$$

$$\sigma_{bending} = \frac{Mr_i}{\pi r_i^3 t_i} \quad (\text{A.62})$$

$$\tau_{shear} = \frac{V}{2\pi r_i t_i} \quad (\text{A.63})$$

$$\left( \frac{P}{2\pi r t_c} + \frac{M}{\pi r^2 t_c} \right) - \left( 9 \left( \frac{t_c}{r} \right)^{0.6} + 0.16 \left( \frac{t_c}{r} \right)^{0.3} \left( \frac{r}{h} \right)^{1.3} \right) \cdot \frac{Et_c}{r} = 0 \quad (\text{A.64})$$

$P$  is the axial loads applied on the considered section of the component  $i$ ,  $r$  and  $t$  are respectively the mean radius and the thickness of the component in the considered section,  $M$  is the bending moment applied on the considered section. All the section have been approximated to thin circular wall. By solving Equation A.64 it is possible to find the minimum thickness  $t_c$  below which the elastic stability or Buckling is not satisfied.  $h$  is the length of the element considered,  $E$  is the Young's modulus of the material taken into account in the analysis, for alluminum 68.9 GPa [42].

- **Pressurized case:** In the pressurized case addition contribution due to the pressure present in the tanks, have to be considered:

$$\sigma_{axial} = \frac{P}{\pi r_i t_i} \quad (\text{A.65})$$

$$\sigma_{bending} = \frac{Mr_i}{\pi r_i^3 t_i} \quad (\text{A.66})$$

$$\tau_{shear} = \frac{V}{2\pi r_i t_i} \quad (\text{A.67})$$

$$\sigma_{ax\_press} = \frac{pr_i}{2t_i} + \rho_{press} g_0 n_x h_l \frac{r_i}{2t_i} \quad (\text{A.68})$$

$$\sigma_{hoop} = \frac{pr_i}{t_i} + \rho_{press} g_0 n_x h_l \frac{r_i}{t_i} \quad (\text{A.69})$$

$$\left( \frac{P}{2\pi r t_c} + \frac{M}{\pi r^2 t_c} \right) - \left( 9 \left( \frac{t_c}{r} \right)^{0.6} + 0.16 \left( \frac{t_c}{r} \right)^{0.3} \left( \frac{r}{h} \right)^{1.3} + \min \left[ 0.191 \frac{P}{E} \left( \frac{r}{t_c} \right)^2, 0.229 \right] \right) \cdot \frac{Et_c}{r} = 0 \quad (\text{A.70})$$

The main difference is the presence of the pressure contribution, in particular in the lateral direction with the Hoop stresses.



## A.16 MECO

Here is reported the procedure followed for the estimation of the relative velocity between the first and second stage after separation. Given the following mechanical characteristics of the springs: energy stored  $E = 2.45J$  per spring and a spring constant of  $k = 1024.49N/m$  it was possible to determine the contraction of each spring by the formula:

$$\Delta L = \sqrt{\frac{2E}{k}}$$

Then by evaluating a number of springs  $N = 70$ , the mass of the second stage with the nose and payload  $m_1$  and the empty first stage  $m_2$ , replacing these data in the formula:

$$\Delta V = \frac{\Delta L}{1 - \frac{m_2}{m_1}} \sqrt{\frac{Nk}{m_2(1 - \frac{m_2}{m_1})}}$$

## A.17 Thicknesses tuning process

This tuning process focused on the most demanding stress conditions, which corresponded to the highest required thickness. These conditions were identified by calculating the minimum Margin of Safety (MS) for each structural component, defined as:

$$MS = \frac{\sigma_{Al}}{\max[\sigma_{ax_p}, \sigma_{hoop}]} - 1$$

Where  $\sigma_{Al} = 448MPa$  [42] is the maximum allowable compressive yield stress of aluminum,  $\sigma_{ax_p}$  is the axial stress (to consider with pressure contribution if pressurizing case considered),  $\sigma_{hoop}$  is the hoop stress applied on the walls of the tanks by the internal pressure, if present. For each component, the case with the lowest Margin of Safety was isolated. If the difference between the thickness associated with this margin and the currently selected thickness was sufficient to permit a reduction of at least 0.5 mm, the selected thickness was adjusted accordingly. The 0.5 mm threshold corresponds to the minimum machinable aluminum sheet thickness.

## A.18 TRANSCOST Model

Considering expendable stage cost  $H_{ve}$ , reusable stage cost  $H_{vr}$  and engines costs  $H_e$  from [30]

$$VehicleCost = H_{ve} + H_{vr} + H_{e1} + H_{e2}$$

$$DOC = Ground\ Operations + Propellant + Flight\ & Mission\ Operation + Transport\ & Recovery + Fees$$

Considering Launch Mass  $M_o$  in  $Mg$ , launch per year  $L = 3$ , number of stages  $N$ ,  $f_v = 0.8$  for storable propellant,  $f_c = 0.5$  for horizontal assembly,  $f_4 = 0.8$  for serial production

$$C_{Ground} = 8M_o^{0.67}L^{-0.9}N^{0.7}f_vf_cf_4 [MY]$$

Propellant cost:  $RP - 1 = 4.76\$/kg$   $LOX = 0.31\$/kg$

$$C_{fm} = 20(0.4 + 1)L^{-0.65}f_4 [MY]$$

$$C_{tr} = \frac{1.5}{L}(7L^{0.7} + M^{0.83}) [MY]$$

The Feeds depend on launch site: for the US Department of Transportation(DOT) are \$2.50 per  $lb$  of LEO payload



*IOC = Administration + Management & Marketing + Technology Support + Launch Site Maintenance*

Given the VIPER-1 first stage dimension, a 20% of the refurbishment cost (RSC) of the falcon 9 booster has been considered. For the engine it was estimated a 11% of the production cost ( $H_e$ )

$$C_{ref} = 0.2 \cdot 250 \cdot 10^3 + 0.11 \cdot H_{e1} \cdot 296000$$

$$\text{Cost per Flight} = \text{Vehicle Cost} + \text{DOC} + \text{IOC} + \text{RSC} [\text{MY}]$$

The price for one MY has been converted to 296000\$ (work-year to dollar 2010[30])

$$\text{Price per Flight} = \text{Price per Payload Mass} * \text{Payload Mass} [\text{kg}]$$

The price for launch per kg of payload is estimated adding 20% to the Pegasus one (88.888\$ [31])

## A.19 Structural Mass Index

### A.19.1 Required thicknesses variation

In this section are reported the required increment of thicknesses for the components of the first stage, in order to allow the structural feasibility of the un-powered re-entry. The most demanding condition between the atmospheric re-entry and the parachute deployment was the latter one, due to the marked deceleration required to apply to the stage with the formation of relevant shear and bending moments.

	Tank LOX	Intertank	Tank RP-1	Aft Skirt
$\Delta t [\text{mm}]$	1.0616	0.8048	1.0763	1.0917

Table A.2: Thicknesses Increment

Dry Mass 1 [kg]	Dry Mass 2 [kg]	$\varepsilon_{s1}$	$\varepsilon_{s2}$	$E_{rr1} [\%]$	$E_{rr2} [\%]$
2283.20	397.04	0.1116	0.1823	22.13	7.02

Table A.3: Dry Masses and Structural Mass Indexes Increment

The variation of thicknesses would affect a substantial increment in the dry masses of the first stage, causing, as a result, an unacceptable increment in the relative error for the structural mass index.



## A.20 Simulink Model

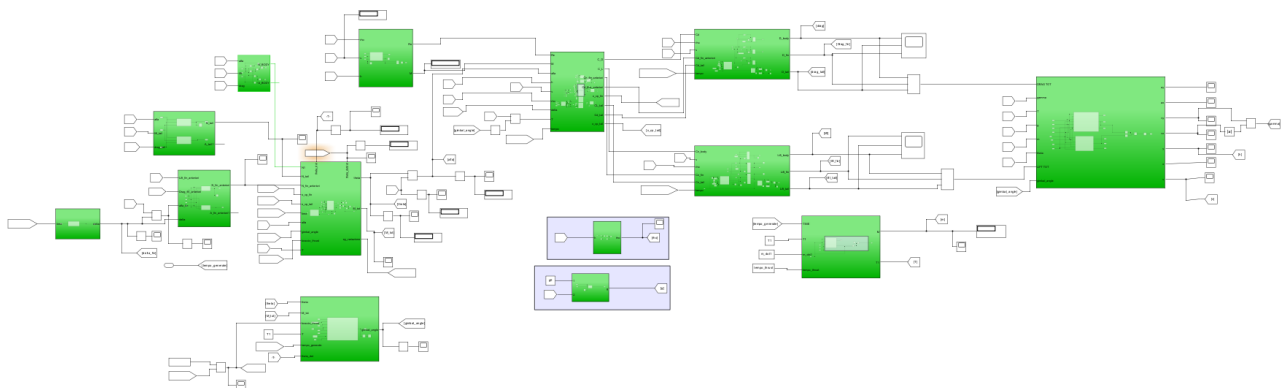


Figure A.42: Overview of the *Simulink®* model developed for the transient phase

# Autorship Declaration

*The team wants to emphasize that everyone gave his own contribution to the project and even though there was a initial distribution of tasks, everyone helped on everything.*

*Overall, everybody took part in the brainstorming and in the first Chapter realization.*

- Carretta Vincenzo 10652780: main trajectory and stages reentry path, launch cost analysis, Thrust Vectoring control devices validation;
- Castoldi Paolo 10668572: Mass Estimation and Structural Analysis;
- De Amicis Vincenzo 11011619: Aerodynamic analysis,Aerodynamic design, drop-phase maneuver design, transient design;
- Di Carlo Pierpaolo 10767871: Mission Analysis and mass budget, main trajectory, Monte Carlo Analysis;
- Di Rago Domenico 10725102: Aerodynamic analysis,Aerodynamic design, drop-phase maneuver design, transient design;
- Manucci Paolo 11010337: Mission Analysis and mass budget, main trajectory, Monte Carlo Analysis, launch cost analysis;
- Rizzi Mirko 10713012: Propulsion (RPA, tank sizing, engine comparison and choice), Openrocket, RASAero, Stability analysis, Thermal analysis, CAD (inertia and CG estimations), Nose cone design;
- Santalucia Andrea 10691238: propulsion subsystem (RPA, engine comparison and choice), stability analysis (OpenRocket, RASAero, fin and tail design), contribution to aerodynamic analysis, drop-phase maneuver simulation and control tuning;
- Taeggi Federico 10739778: Re-entry strategy analysis for first and second stage, parachute design.